RESEARCH ACTIVITIES IN OPTOELECTRONICS AND ELECTRONICS MANUFACTURING 2002

PUBLISHER

VTT Electronics, Kaitoväylä 1, P.O.Box 1100, FIN-90571 OULU, FINLAND
Tel. +358 8 551 2111, Fax +358 8 551 2320
Electronic mail: ele.info@vtt.fi

VTT ELECTRONICS, OULU 2003

PREFACE

VTT Electronics is one of the six operative units of VTT, the Technical Research Centre of Finland, an independent, multi-field contract research organisation. The main task of VTT Electronics is to work as a strategic R&D partner of the electronics industry, thus for its part, ensuring the prospected growth in this sector. At VTT Electronics, 72 of its 300 staff members are involved in optics and optoelectronics.

The main goal of Optoelectronics research is to assist companies in utilizing advanced optical, photonic and optoelectronic technologies in their products. Our core competence is in the integration of optoelectronic modules and instruments. This focus includes challenging research and development aims in modelling, simulation and design, new advanced materials, cost-effective fabrication, manufacturing and packaging applied for multi-technological solutions in optics, optical communication, optical measurements and also sensors and instrumentation. A big thing in 2002 was the inauguration of our Micromodule Centre, offering new and better services to our customers in photonic fabrication and packaging, high precision machining, and a unique pilot environment for printable optics and electronics. Also the 'Microfabrication incubator' activity has been launched to promote new start-ups and manufacturing businesses.

In this report you will find extended abstracts concerning some of the published research and development work carried out in 2002. The abstracts of the examination theses completed by our personnel and a list of publications are also included.

Oulu, May 8, 2003

Further information: www.vtt.fi/ele

Jouni Tornberg
Head of Optoelectronics research
Jouni.Tornberg@vtt.fi

Harri Kopola
Research professor
Harri.Kopola@vtt.fi

TABLE OF CONTENTS

VTT Micromodule Centre Inauguration

The VTT Electronics Micromodule Centre facilities form an unique entity - the largest optoelectronics research facility in the Nordic Countries - allowing versatile manufacturing of optics, electronics and optoelectronics, combined with design, simulation and characterisation services. They include clean room facilities for component and module assembly and packaging, a glass and optics workshop, 5-axis mechanical manufacturing and versatile design, simulation and characterisation tools. These enable services to be provided in innovative electronic and optoelectronic integrated module and instrument R&D using modern optics, electronics and manufacturing technologies (http://www.vtt.fi/ele/services/).

The environment especially supports the development of new manufacturing technologies and businesses by offering not only product development and research co-operation to industry, but also laboratory rooms and the right to use VTT's other facilities, as well as prototype and small-scale manufacturing services in ourmicromachining incubator. Services to industry decrease the need for investments, especially in the testing and development phase. One of the goals of activities is therefore to support new spin-off -companies.

THE MAIN FACILITIES:

In November 2002 VTT Electronics' new clean rooms were taken into use. This doubled the total clean room area to about 1000 m^2 (classes ISO5 and ISO7). They form part of an environment designated for the development of micromodule and optoelectronic component technologies and product applications. The environment includes various pieces of equipment and tools which allow state-of-the-art research work and services.

With *thin and thick film processing* equipment, new thin film, polymer and hybrid materials are manufactured using evaporation, sputtering, spinning or sol-gel processing. They have many application fields, such as communication, chemical and biosensing, microfluidistics and optics, and electronics packaging. The applications manufactured include protective materials for electrical and optical components (including scratch-resistant, EMI and EDS coatings, and hydrophobic coatings) and components for micro-optics (waveguides, OLEDs, diffractive and integrated optics devices). As a new research item, technologies for *printable optics and electronics* have been introduced, which allow these materials and structures to be produced fast and cost effectively on flexible substrates (plastics and paper) using PICO pilot machine.

Interconnection and packaging technologies are used, for example for *micromodule encapsulation*. There is work being carried out with photonic modules, MEMS packaging and RF and microwave modules for telecommunication electronics. Services include the design and implementation of electronic and optoelectronic modules as well as reliability testing.

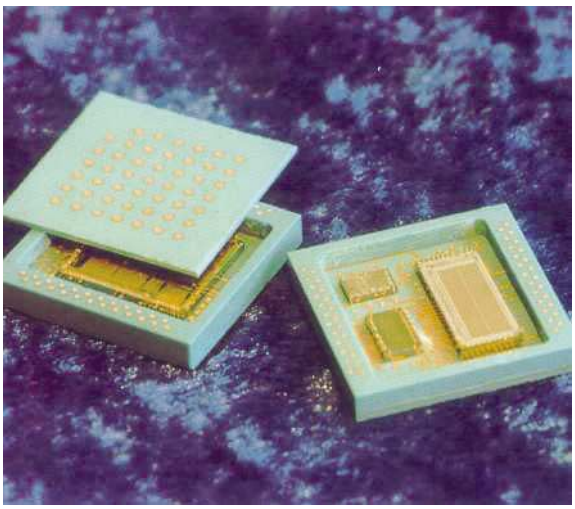

The *Low Temperature Co-fired Ceramics* (LTCC) manufacturing line allows electronic and optoelectronic modules to be designed and implemented using multilayer ceramic

technology. Services include - in addition to the R&D co-operation – the prototype and small-scale manufacture of LTCC substrates and modules for electronics and opto-electronics as well as sensor packaging. The off-the-self LTCC materials used currently include DuPont951, DuPont943, Heraeus CT2000 and Ferro A6-S tapes.

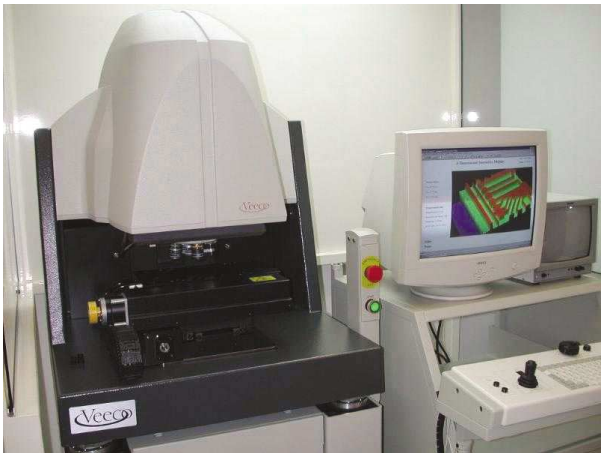

For *characterisation and testing* there are versatile facilities, for environmental and electrical testing, characterisation of optical devices. There are also high quality laboratories for optical spectroscopy and machine vision.

Within the area of *precision machining* VTT Electronics has versatile environment for various processes. There is a glass and optics workshop (with cutting, polishing, rounding and drilling equipment) and an optical clean room with a pneumatically suspended optical bench, a high precision alignment station, optical design, modelling and simulation tools, and mechanical design tools. There is also a workshop containing, for example, a state-of-the-art 5-axis CNC milling machine.

The purpose of the ongoing development activities is to increase R&D in the fields of micromodule and photonic technologies (especially for wireless and optical communication), optical instruments and sensors (for the process industry), biomolecular recognition and polymer optoelectronics (for product packages, printed matter and electronic products). The new clean rooms, combined with the new equipment and VTT's own research and development work, together with skilled personnel ensure that we can stay at the forefront of the R&D community and supply high level services to our customers long into the future.

Tero Majamaa
Tero.Majamaa@vtt.fi

Harri Kopola
Harri.Kopola@vtt.fi

Jyrki Ollila
Jyrki.Ollila@vtt.fi

Timo Salo
Timo.Salo@vtt.fi

Near Field Beam Properties of the Very Small Aperture Laser

The near field beam properties of the very small aperture laser were studied using a finite difference time domain method.

1 INTRODUCTION

Near field optical data storage (ODS) has been studied extensively as a potential choice for the future generation ODS. Solid immersion lens[1] (SIL), direct semiconductor laser readout[2,3] (DSLR) with the very small aperture laser[4] (VSAL) source, and super resolution[5] (SR) technique are among the technologies which take advantage of the evanescent coupling of the electromagnetic field to the disk's data layer. The DSLR system, using a conventional Fabry-Perot (FP) laser diode, can be used as a source, but the smaller spot size obtained using the VSAL is tempting.

In our work a two-dimensional finite-difference time domain (2D FDTD) (see, for example, Taflove[6]) model was used to study the beam properties in a DSLR system using the VSAL as a source. The simulation results obtained from the VSAL structures were compared to ones from a conventional Fabry-Perot (FP) laser diode. We studied the decrease in spot size and the power density in the disk's data layer achieved by the use of the small aperture. From the simulations it was noticed that the resonance effects within the laser front facet and the optical disk significantly affect the system.

In the next section the simulation model is briefly described. The results from the simulations are presented in section 3 and in the last section there are some discussion and conclusions.

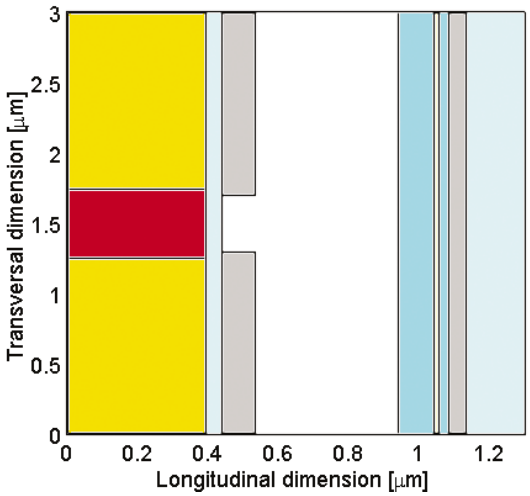

Figure 1. Schematic picture of the modelled VSAL laser and the first surface recording optical disk.

2 SIMULATION MODEL

Figure 1 shows the schematics of the simulation model. The laser waveguide is shown in the central part on the left side of the figure. Around the 0.4 μm tick mark are located the material boundaries between the cladding, the insulating layer and the metal layer with the aperture. The air gap is the white region between the laser end and the optical disk. The disk is assumed to be a first-surface-recorded phase change disk. In Figure 1, the disk surface is located around the 1.0 μm tick mark. The thin film structure of the disk consists of a cover layer, a phase change data layer, a spacer, a metal reflector and a substrate. In this work we did not intend to optimise the optical disk structure in any way. The disk parameters for the FP laser source have been studied in more detail, for example in Kataja et al.[7], and the flying height (airgap) for the simplified system in Kim et al.[8].

The absorption density as a function of the airgap, shown in Figure 2, is calculated with a system where aperture diameter and metal layer thickness are 400 nm and 100 nm respectively. In the figure, the FWHM diameter is shown with a thicker red line. The oscillations in the absorption density and the spot size are clearly seen in this plot. If the plot is studied in more detail it is observed that the minimum spot size occurs just before the maximum absorption density.

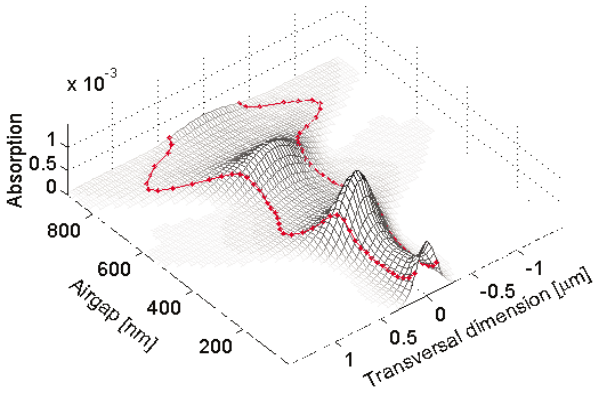

Figure 2. Absorption density in a system where aperture diameter and layer metal thickness are 400 nm and 100 nm respectively.

3 SIMULATION RESULTS

A comparison of the FWHM spot size of the isolated laser and the ESEC configurations is shown in Figure 3 for both the VSAL system and the conventional FP laser system. In this figure we see how the ESEC affects the beam shape and spot size via the resonance effects in the ESEC. The

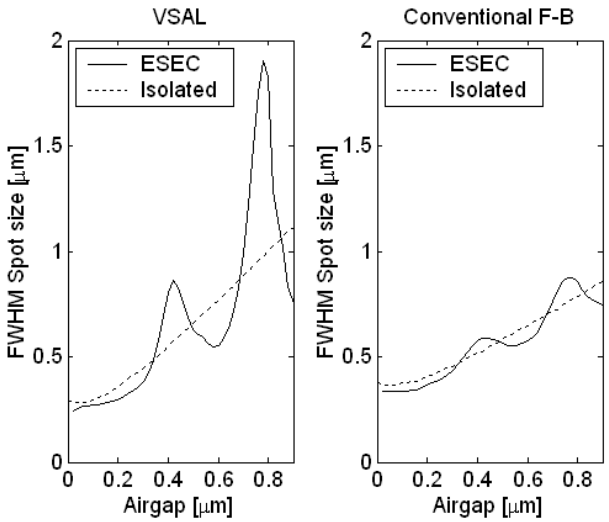

Figure 3. VSAL and conventional laser spot size in the isolated and ESEC system.

oscillations in spot size and absorption density are with a half wavelength period as the function of the air gap thickness and it seems that the free space spot size gives only an average value for the spot size of both the VSAL and the conventional system. Therefore it is obvious that the spot size cannot be studied independently by looking at the beam propagating in the free space, but rather the whole optical system has to be taken into account.

Figure 4 shows the FWHM spot size in three VSAL cases, comparing them to the conventional FP laser. Using these parameters the VSAL spot size is smaller than with the conventional FP laser until an airgap of about 300 nm is reached. After that the VSAL spot size starts to increase rapidly. In an airgap of around 600 nm, the VSAL spot size is again smaller than the spot size of the conventional laser. An interesting feature is that the spot size with a 150 nm aperture is slightly (~30 nm) bigger in the airgap range 70 - 200 nm than the spot size with a 400 nm aperture. The same phenomena occur in the range 400-600 nm but the difference is significantly larger. These could be explained with a larger divergence angle from the smaller aperture. But this explanation does not hold between these regions where spot sizes, as a function of aperture size, are about the same between the VSAL systems. With these geometries the spot size with the 150 nm aperture is smaller than with the 400 nm aperture only in a very close region (airgap < 70 nm).

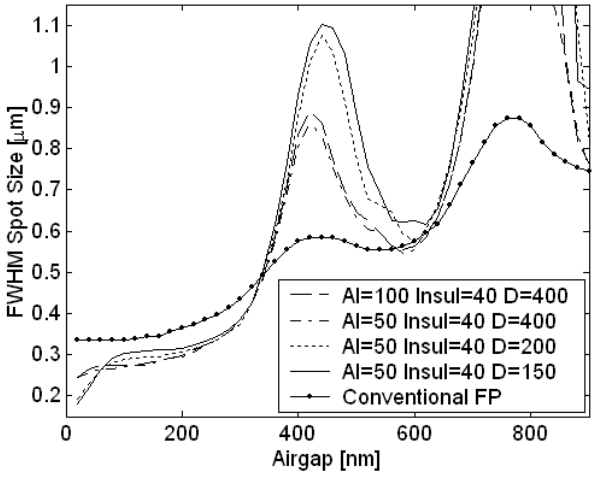

Figure 4. VSAL spot size compared with conventional laser in ESEC system. In VSAL first number is metal thickness and second aperture diameter.

The metal layer thickness of the VSAL aperture does not seem to have an effect on the spot size. However, when the metal layer thickness is increased, the reflectivity of the front facet of the VSAL is also increased and the total absorption in the PC layer decreased. An increased reflectivity from the aperture itself means a weaker signal from the disk and therefore reduced readout signal levels. Absorption density, on the other hand, is important when writing to the disk is considered.

4 DISCUSSION AND CONCLUSION

The spot size of the VSAL system was studied and compared with the conventional FP laser source. The differences between spot sizes for an isolated laser and a laser with the ESEC system were considered. It was noticed that spot size is affected by the ESEC system and therefore when the VSAL system is characterised one has to remember that the measurement setup affects the beam properties. The difference in VSAL spot size compared with the conventional FP laser is constant over a short range (airgap < 300 nm), which could be useful in ODS because the spot size is not sensitive to airgap in this region. After this range the VSAL spot size begins to oscillate along with reflectivity and absorption. On the other hand if an extremely small spot size is desired the airgap should be as small as possible.

REFERENCES

1. E. Betzig, J.K Trautman, R. Wolfe, E.M. Gyorgy, P.L Finn, M.H. Kryder and C.H. Chang, Appl. Phys. Lett. 61, 142-144 (1992).
2. Ukita H., Katagiri Y. and Fujimoro S., Applied Optics 28, pp. 4360-4365, 1989.
3. J. Aikio, K. Kataja and D. Howe, Proc. SPIE 4595, 163-173 (2001).

4. Partovi A., Peale D., Wuttig M., Murray C.A., Zydzik G., Hopkins L., Baldwin K., Hobson W.S., Wynn J., Lopata G., Dhar L., Chichester R. and Yeh J.H-J, Appl. Phys. Lett. 75, 1515-1517 (1999).
5. Tominaga J., Nakano T. and Atoda N., Appl. Phys. Lett. 73 (1998) 2078.
6. Taflove A. and Hagness S.C., Artech House, Boston, 2000.
7. K. Kataja, J. Aikio and D. Howe, "Numerical study of near-field writing on a phase-change optical disk," Appl. Opt. IP 41, 4181-4187 (2002).
8. Kim J-Y., Hsieh H.C., *'An Open-Resonator Model for the Analysis of a Short External-Cavity Laser Diode and its Application to the Optical Disk Head*', J. Lightwave Technol., Vol. 10, pp. 439 – 447, 1992.

Kari Kataja
Kari.J.Kataja@vtt.fi

Janne Aikio
Janne.Aikio@vtt.fi

Dennis G. Howe
University of Arizona, Optical Sciences Center, Tucson, Arizona, USA

UV-photoreactive Organo-tin Compounds for Photolithographic Patterned Transparent Electrodes

ABSTRACT

Fabrication of directly UV-photopatternable pure and antimony doped organo tin films is presented. Direct UV-photopatternability has been achieved by modifying tin and antimony alkoxide precursors with UV-photoreactive methacrylic acid or benzoylacetone ligands. Spin-on deposited films were lithographically patterned using a UV-light source (I-line) with a contact mask. After developing, structures were thermally converted to crystalline, conductive pure and Sb-doped tin oxides. The effects of UV-irradiation, increasing antimony doping level and the used photoreactive ligand on the electrical properties of the single layer films are analyzed.

INTRODUCTION

Directly photopatternable antimony doped tin dioxide (ATO) thin films are of great interest in applications where transparent conductive materials are required. These include transparent electrodes in display devices [1] and solar cells [2]. For these applications ATO material is a potential alternative due to its lower costs compared to widely used tin doped indium oxide coatings (ITO). Tin dioxide and its derivatives also have a sensitivity for gas detection [3]. However, due to the high chemical durability of tin dioxide, the fine patterning of tin dioxide thin films by wet etching has been reported to be rather complicated. Although dry etching patterning methods have been successfully demonstrated, they are usually time-consuming, expensive, substrate size limited and special equipment is needed. Therefore new material approaches for the fast and cost-effective fine patterning of tin dioxide and its derivative thin films are required.

We have successfully demonstrated a new approach for the fine patterning of pure and doped tin dioxide thin films [4]-[6]. This new approach employs a combination of direct photolithographic processing of liquid phase deposited organo-tin films, followed by thermal annealing. In order to fabricate UV-photoreactive organo-tin films, organic ligands such as methacrylic acid (MAA) and benzoylacetone (BzAc) have been used to form bidental chetale type complexes with tin and antimony alkoxides. Materials modified using MAA and BzAc behave as negative tone photoresist under UV-irradiation. Hence, the solubility of the UV-irradiated areas decreases and structures can be developed by dissolving the unexposed areas with alcohols and ketones. In order to obtain conductive transparent conductors, UV-photopatterned organo-tin structures are transformed to crystalline and conductive form by thermal annealing.

EXPERIMENTAL

The directly UV-photopatternable, pure and antimony doped tin dioxide materials were synthesized by reacting methacrylic acid or benzoylacetone with tin and antimony alkoxides [4]-[6]. ^{1}H & ^{13}C NMR, IR- and mass spectroscopic techniques were used for the identification of the bidental chelate type reaction products.

In order to obtain the UV-photoresponse, a radical UV-photoinitiator was added to the solutions of methacrylic acid modified tin and antimony alkoxides. The UV-photoinitiator forms free radicals under UV-irradiation. These radicals assist the photopolymerization of the methacrylic ligands which furthermore leads to the diminished solubility of the UV-irradiated parts of the material. In the case of benzoylacetone modified alkoxides, β-diketonate type of ligands forms chelate rings which show absorption bands at UV wavelengths. These absorption bands are characteristics of the π-π^* transitions in chelate rings [7]. The UV-irradiation at the absorption band wavelengths dissociates the chelate bonds and simultaneously changes the solubility of the material in solvents such as alcohols, ketones or acids.

Thin films of both types of material were formed in a two stage spinning process: first the solution was spread on the substrate for 5 seconds at 500 rpm and then spun-on for 30 seconds at 1250 rpm. Formed single layer thin films were patterned using a binary photomask with UV-irradiation from a mercury UV-lamp source. After UV-irradiation the unexposed areas were removed using isopropanol (methacrylic acid modified materials) and acetone (benzoylacetone modified materials). After this the patterned pure and antimony doped organo tin structures were decomposed onto the crystalline, pure or antimony doped tin dioxide in an ambient atmosphere at an elevated temperature (560°C).

RESULTS

In Figure 1, conductor line images (Wyko NT 2000) with 25 µm line widths are presented. Figures 1a and 1b show air annealed conductor lines fabricated using MAA and BzAc modified precursors, respectively.

Air annealed films are highly transparent at visible wavelengths with transmission values of over 85 %. In Table 1 the electrical resistivities of the fabricated slab films are shown. For comparison, the electrical resistivities of the unexposed (unpatterned) samples are also shown.

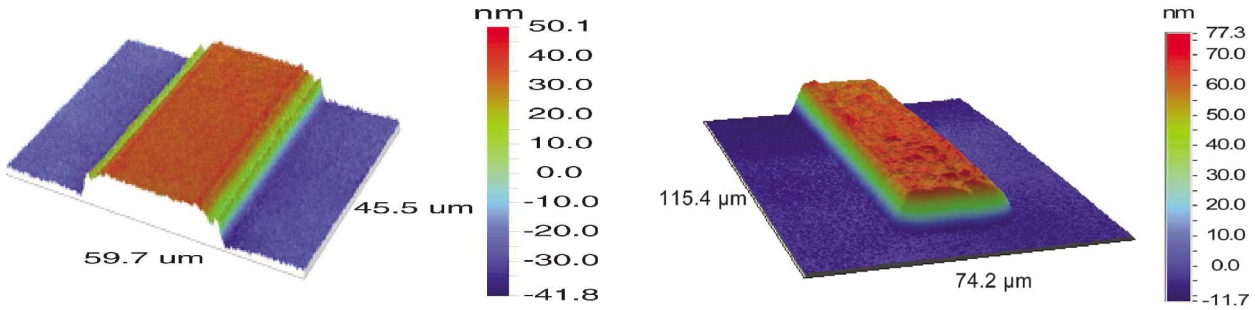

(a) (b)

Figure 1. Figure 1a shows a conductor line fabricated using MAA modified precursors. Figure 1b shows a corresponding line fabricated using BzAc modified precursors. Film thicknesses are 55 and 68 nm, respectively.

Table 1. Electrical resistivities of the unexposed (unpatterned) and UV-irradiated (patterned), pure and antimony doped tin dioxide thin films.

Sb-doping level (%)	Electrical resistivities (Ω·cm)			
	Unpatterned BzAc	Patterned BzAc	Unpatterned MAA	Patterned MAA
0	213	149	132	67
1	0.21	0.17	0.85	0.21
5	0.05	0.05	0.20	0.08
10	0.11	0.13	0.49	0.28

From the values shown in Table 1 it can be concluded that in all cases the lowest electrical resistivities were obtained when antimony doping concentrations were 5 mol.-%. The lowest resistivity was obtained with benzoylacetone modified samples. In this case UV-irradiation has only a negligible effect on the resistivities of the fabricated samples. In the case of methacrylic acid modified samples, electrical resistivities were lower for UV-irradiated samples. This phenomenon was investigated using atomic force microscopy, X-ray photoelectron spectroscopy (XPS) and X-ray powder diffraction (XRD) techniques. According to the obtained results, the UV-irradiation induced an increase in the thin film conductivity, mainly resulting from the increased crystal size of the fabricated materials but also from differences in the antimony distribution between unexposed and UV-irradiated samples [6].

CONCLUSIONS

We have prepared directly photopatternable pure and antimony doped organo tin thin films using coating solutions of benzoylacetone and methacrylic acid modified alkoxide precursors. All investigated materials can be directly photopatterned using UV-irradiation from a normal pressure mercury lamp. The highest obtained conductivity, 20 S/cm (lowest resistivity 0.05 Ω·cm), for the single layer thin film was achieved using benzoylacetone modified precursors with antimony doping concentration of 5 mol.-%.

REFERENCES

[1] S.-S. Park, J.D. Mackenzie, Thin Solid Films 258 (1995) 268, and references therein.
[2] C.M. Lambert, Sol. Energy Mater. 6 (1981) 1.
[3] D. Kohl, Sensors and Actuators 18 (1989) 71.
[4] T. Kololuoma, A. H.O. Kärkkäinen and J. T. Rantala, Thin Solid Films 408 (2002) 128.
[5] T. Kololuoma, L.-S. Johansson, J. M. Campbell, A. Tolonen, M. Halttunen, T. Haatainen and J. T. Rantala, Chemistry of Materials 14 (2002) 4443.
[6] T. Kololuoma, A. H. O. Kärkkäinen, A. Tolonen and J.T. Rantala, Thin Solid Films, *Submitted for publica- tion.*
[7] D. W. Barnum, J. Inorg. Nucl. Chem. 21 (1961) 221.

Terho Kololuoma
Terho Kololuoma@vtt.fi

Ari H. O. Kärkkäinen

J. T. Rantala
GuideOptics Oy, P.O.Box 114, FIN-90571 Oulu, Finland

Sol-Gel Waveguides as Platform for Lab-on-a-Chip Applications

1. INTRODUCTION

There are many applications where multi-parameter sensing capability is hugely attractive. [1, 2] The device can be expanded to measure a wide range of analytes for applications in the biomedical (i.e. blood gas monitoring), automotive (in-car comfort and condition control) and 'household' (Indoor Air Quality monitoring) sector.

Novel miniaturised systems capable of measuring a number of parameters simultaneously are of great interest and are based on a "concept" patent developed by Professor MacCraith at DCU. [3]

The new generic platform is based on photopatternable, organically modified silane materials and sol-gel technology, used for fabrication of the multi-mode waveguide structures, and for immobilisation for analyte-sensitive complexes.

As opposed to conventional techniques used to obtain waveguide structures, the low-temperature sol-gel technology based on photopatternable, organically modified silanes, avoids high processing temperatures (>1000°C) or multi-step etching. Key advantages are simplicity, low cost and adjustable chemical composition of hybrid materials.[4]

2. EXPERIMENTAL

2.1 Multi-parameter sensing system on a sol-gel platform (lab-on-a-chip)

The Efficient Capture System has been based on a US Patent by Professor MacCraith et al.[3] Sensor spots, immobilised in a sol-gel matrix, are applied on waveguides and excited by a blue LED. Sensor fluorescence is guided along the waveguide and optical signals are detected at the end face of the waveguide (Figures1 and 2).

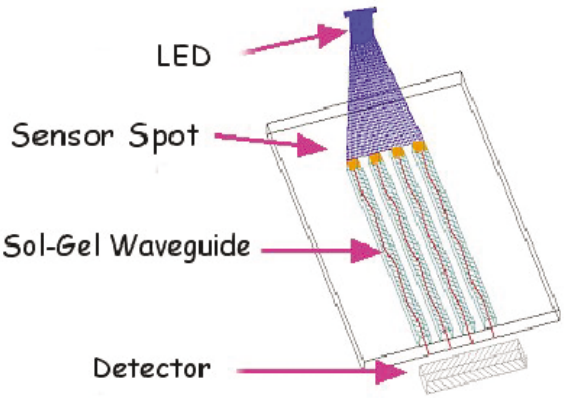

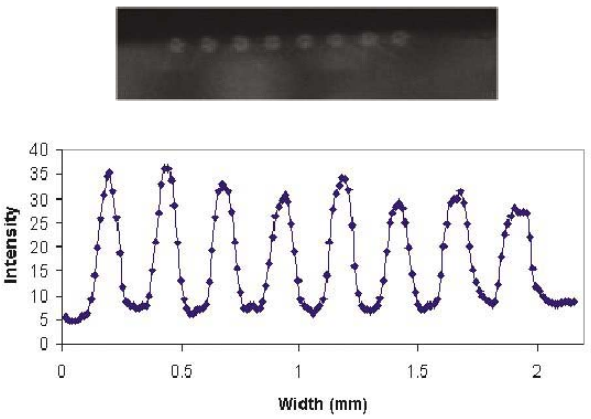

Figure 1.Scheme of a lab-on-a-chip concept
Figure 2. CCD image of fluorescence from waveguides and corresponding intensity profile

2.1 Fabrication and analysis of waveguide structures for miniaturised sensor systems

Photopatternable, organically modified material has been synthesised by the hydrolysis and condensation of silane precursors. The product of condensation was stirred with the crosslinking agent (trimethylolpropane triacrylate) to increase material UV-sensitivity. Figure 3 shows the organically modified material with a sufficient amount of double bonds to react via radical polymerisation triggered by UV-irradiation.

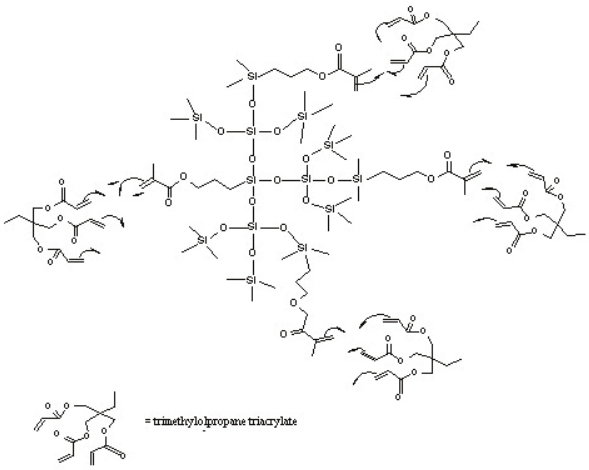

Figure 3. Radical polymerisation through double bonds

The fabrication of sol-gel waveguides is achieved through the photolithography process. The sol-gel material is spin coated onto the silicon substrate. Residues of the solvents used during synthesis are removed in the pre-bake stage. Waveguides are "written" by UV-exposure using a UV-mask aligner (Figure 4). Unexposed areas on the substrate are rinsed off using isopropanol as the developer solvent.

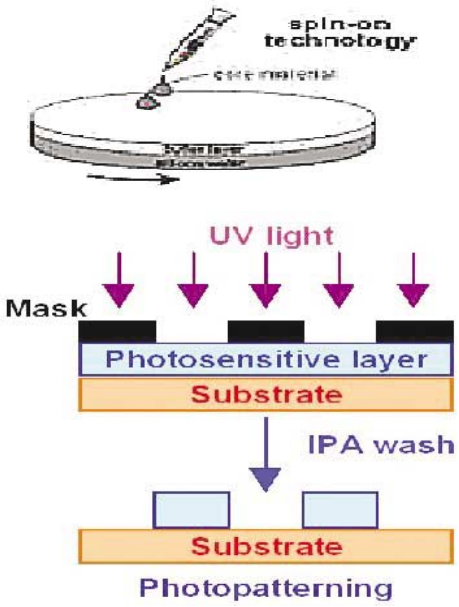

Figure 4. Principles of spin coating, mask UV-irradiation and developing steps within waveguide fabrication

Waveguide microstructures were investigated using a White Light Interferometer (Figure 5). Surface roughness values (rms) of the developed films, analysed using the same technique, are in the range 0.7 to 1.1 nm for a 1 x1 µm area. This meets the requirements of most optical applications (Figure 6).

Multiple analyte-sensing complexes, like oxygen sensitive ruthenium complex [Ru^{II}-tris (4,7-diphenyl-1,10-phenanthroline)]$^{2+}$, can be deposited on the top of the waveguide using stamp, ink-jet or pin printing.[5] This allows for the capture of multiple data parameters on one sensor chip.

3. CONCLUSIONS

The simultaneous detection of several analytes is a major requirement for fields such as food and environmental control and medical diagnostic. The main objective of future research will be the positioning of oxygen, carbon dioxide, humidity and temperature sensors on the same miniature system.

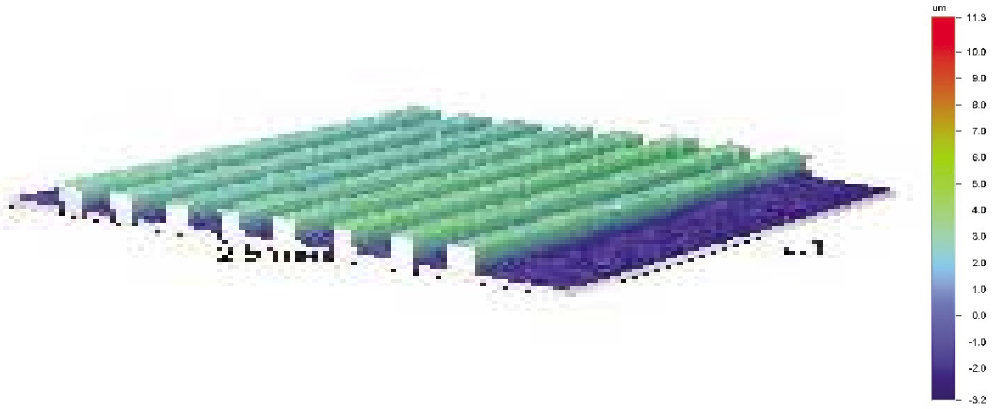

Figure 5. Image of waveguides generated using a White Light Interferometer

Figure 6. Generated image of the surface on top of the waveguide with a rms value of 1.05 nm

Sol-gel waveguides are a promising platform for the capture of fluorescence signals. They are also low cost and relatively easy to produce to the required standards.

The photopatternable, organically modified hybrid material for the multi-channel waveguide fabrication has good optical properties, and its refractive index is tuneable. Several other properties of the material such as adhesion, porosity and sensitivity are also adjustable.

The focus of future research is to find an optimised and repeatable deposition technique for a multi-channel waveguide and improve the performance of the sensing complexes currently under experimentation.

4. REFERENCES

1. "Tailoring of sol-gel films for optical sensing of oxygen in gas and aqueous phase"; McDonagh, C., MacCraith, B.D., McEvoy, A.K.; *Anal. Chem.*, 1998, 70 (1), 45-50
2. "Optical chemical sensors based on sol-gel materials: Recent advances and critical issues"; MacCraith, B.D., McDonagh, C., McEvoy, A.K., Butler, T., O'Keeffe, G., Murphy, V.; *J. Sol-Gel Sci. Tech.*, 1997, 8, 1053-1061
3. US Patent US6137117; MacCraith B.D., Feldstein M.J., Ligleer F.S., 2000-10-24
4. "Development of Polymeric Materials for Waveguide Components", M.Kusevic, M. Hiltunen, SPIE´s International Symposium Photonics West 2002, San Jose, USA
5. 'Phase fluorometric dissolved oxygen sensor'; McDonagh, C., Kolle, C., McEvoy, A.K., Dowling, D.L., Cafolla, A.A., Cullen, S.J., MacCraith, B.D.; Sensors and Actuators B, 2001, 74, 124-130

Maja Kusevic
Maja Kusevic@vtt.fi

O. MacOughey, A. McAvoy, B. MacCraith, J.M. Sabatie
Optical Sensors Laboratory, Dublin City University, Ireland

Photolithographically Miniaturised Organic Light-emitting Devices with Red, Green, Blue and White Electroluminescence

ABSTRACT

We report on BAlq, Alq_3 and DCM-based miniaturised organic light emitting devices (OLEDs). The electroluminescence spectrum consists of blue, green and red bands at 493 nm, 528 nm and 629 nm, respectively. The organic white-light emitting device was demonstrated with the direct mixing of two colours from two different emissive layers separated by a carrier blocking layer. The diameters for emissive areas varied from 100 µm to 800 µm.

INTRODUCTION

Organic light-emitting devices (OLED) meet many of the targets necessary for display and instrumentation applications. For example in devices that use small screens, such as cell phones, personal digital assistants, wristwatches and cameras. The important advantage of OLEDs is their wide range of emission spectra made possible by tailoring organic materials. Other advantages are their potential for low-cost processing, the possibility of fabricating large-size displays and their mechanical flexibility. The fabrication of lithographically miniaturised OLED light sources has been demonstrated and these techniques can be used to produce emissive areas of various sizes [1].

The basic OLED structure consists of a transparent conductive anode layer, organic layer(s) and a metal cathode layer. An externally applied voltage drives electrons and holes from cathode and anode, respectively, into the recombination region where they form an excited state, called exciton. The recombination of the electron-hole pair in the organic layer leads to a photon emission.

EXPERIMENT

The fabrication of the OLED is carried out in two steps: 1) Photolithographically patterned indium-tin-oxide (ITO), 2) deposition of organic and metal layers. Shipley's Microposit S1805 photoresist was used to define the active area in the OLEDs. This photolithography process includes spin coating of resist, soft baking at 115^{0}C, UV-exposure using photomask, development, and hard baking at 130^{0}C. The diameters for emissive areas varied from 100 µm to 800 µm.

The devices consisted of multilayer structures. The organic materials were sublimated using resistive evaporation. N,N´-di(naphthalene-1-yl)-N,N´-diphenylbenzidine (α-NBD), tris(8-hydroxyquinolate) aluminium (Alq_3), 5,6,11,12-tetraphenylnapthacene (Rubrene), 4-(dicyanomethylene)-2-methyl-6-(julolidin-4-yl-vinyl)-4H-pyran (DCM) and aluminum(III)-bis(2-methyl-8-quinolinato)-4-phenylphenolate (BAlq) were used as hole transport layer, green-emitting/electron transport layer, a yellow dye material, a red dye material and a blue emitting material, respectively. Finally, the metal films (Mg, Ag) were deposited using e-beam evaporation. Immediately after deposition the devices were encapsulated using UV-cured epoxy material.

The light output and voltage measurement was done with a ANDO AQ2140 multimeter and a Keithley 2400 SourceMeter, respectively. During measurement the sample was located at a distance of 2 cm away from the photodetector.

RESULTS

Three different light-emitting devices were fabricated, including blue (B), green (G) and red (R) colours. Using these colours (materials) it is possible to fabricate an efficient full colour (RGB) display. Figure 1 represents the electroluminescence (EL) spectra for three emitting materials. Maximum EL peaks for BAlq, Alq_3, and Alq_3:DCM (10 wt-%) were achieved at 493 nm (full width at half maximum (FWHM) = 97 nm), 528 nm (FWHM=110 nm), and 629 nm (FWHM=107 nm), respectively.

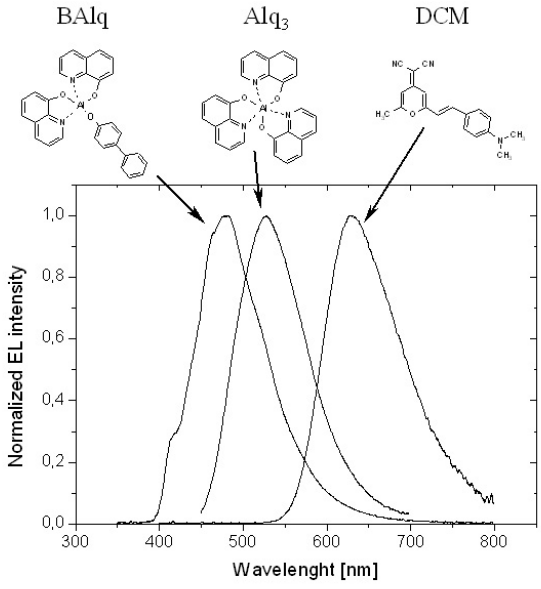

Figure 1. EL spectra and chemical structures for BAlq, Alq_3, and DCM materials.

The luminance-power output-voltage characteristics for three light emitting devices are shown in Figure 2. The lower efficiency of red light compared to green light was due to concentration quenching. Aggregate formation at high dopant concentration provides sites for non-radia

tive recombination, which reduces the possibility of radiative emission [2]. For the blue-light emitting device (BAlq) brightness was reduced due to weak adhesion between blue emitting layer and cathode.

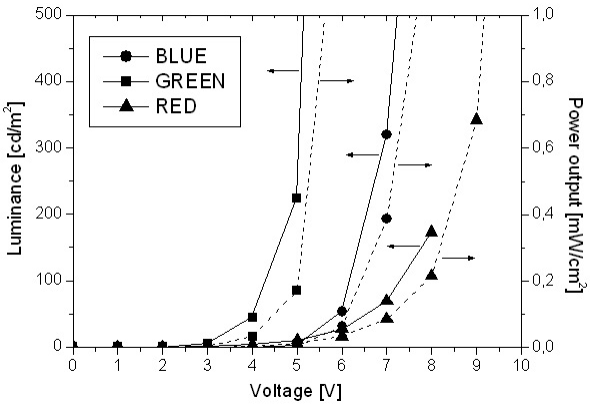

Figure 2. Luminance (solid lines)-power output (dashed lines)-voltage characteristics for blue, green and red light emitting devices with a diameter of 400 µm of emissive area.

In this work, the method used to achieve white emission is to control the spatial location of the exciton-recombination-zone by introducing a carrier blocking layer between the hole transport layer and electron transport layer [3]. White emission is achieved using two different colour-emitting layers (Figure 3). These layers were BAlq for blue emission and Alq:Rubrene for yellow emission.

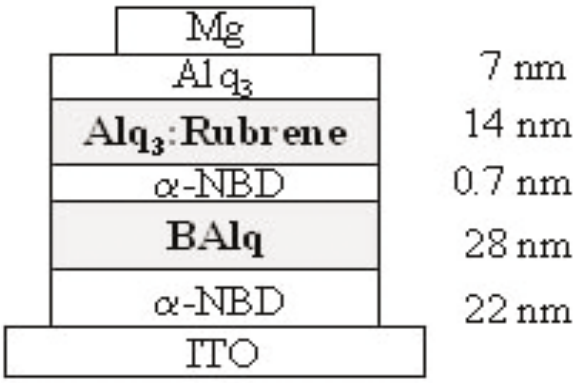

Figure 3. The schematic cross sections of fabricated white-light OLED device.

Figure 4 shows EL spectra for device at various applied voltages. At the low voltage range the recombination of excitons occurs at both emitting layers, and increasing the applied voltage from 10V to 16V shifts the recombination in the BAlq layer. Thereby, the emission colour tends to shift from greenish white to bluish white.

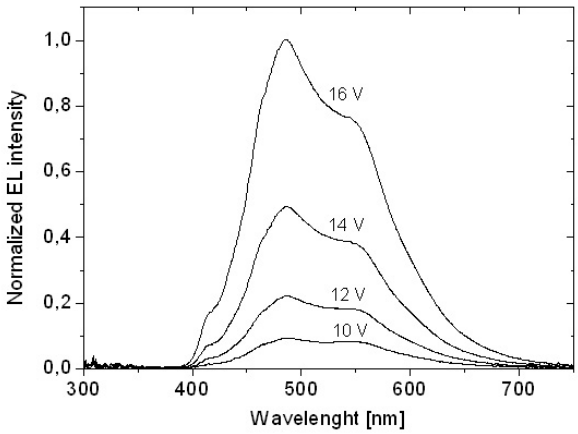

Figure 4. EL emission spectra at various applied voltages for micro OLED.

CONCLUSIONS

In summary, we fabricated four different light emitting devices, including blue (B), green (G), red (R), and white colours. Using these colours (materials) it is possible to fabricate an efficient full colour (RGB) display. Furthermore, miniaturised light sources were studied, which can be used, for example, in micro-optical systems.

REFERENCES

1. A. H. O. Kärkkäinen, J. T. Rantala, M. Jabbour, C. Liang, R. Bedford, N. Peyghambarian, M. R. Descour, G. E. Jabbour, Proc. SPIE - Functional Integration of Opto-Electro-Mechanical Devices and Systems, 2001, vol. 4282, 101.
2. V. Bulovi , A. Shoustikov, M. A. Balbo, E. Bose, V. G. Kozlov, M. E. Thompson, S. R. Forrest, Chem. Phys. Lett., 1998, 287, 455.
3. S. Lee, C.-H. Chung, S. M. Cho, Synth. Met., 2000, 126, 269-273.

Markus Tuomikoski
Markus Tuomikoski@vtt.fi

Ari Kärkkäinen
Chemtone Oy, Kaitoväylä 1, FIN-90571 Oulu, Finland

Kaisa-Leena Mäkelä

Sol-gel Processed Lanthanium Doped Lead Zirconium Titanate Electro-optical Thin Films

ABSTRACT

In this study, the sol-gel process to deposit electro-optical lanthanium modified lead zirconium titanate thin films was investigated. These films had very small surface roughness (<1 nm), strong second order electro-optic effect, and a high index of refraction.

INTRODUCTION

Perovskite ferroelectric materials have been subjected to intensive study over the past few years due to their excellent functional properties, such as electro-optic effect, piezoelectricity, pyroelectricity and acousto-optic effect. Their electrical, optical and electromechanical properties offer a wide variety of applications in microelectronics, -mechanics and -optics.

Thin film materials which are transparent and show good optically nonlinear properties have potential for use in novel integrated optical devices. One material of interest is lanthanium doped lead zirconium titanate (PZT). Because pure PZT is opaque, it is unsuitable for optical applications. However, modifying it by using lanthanium causes the material to become transparent and show measurable electro-optic behaviour [1]. Several deposition methods have been applied for manufacturing doped PZT thin films: multitarget sputtering [2], laser-assisted deposition [3], and sol-gel processing [1]. The advantage of sol-gel processing is the potential for high-volume production because the material is deposited in liquid phase.

SOL-GEL PROCESS

The chemical composition of La/Zr/Ti, 9/65/35, was used to achieve thin films with a strong electro-optic effect [2]. The precursor materials were lead acetate trihydrate $Pb(CH_3COO)_2\ 3H_2O$, lanthanum acetate hydrate $La(CH_3COO)_2\ xH_2O$, zirconium propoxide $Zr[(CH_3)_2CHO]_4$, and titanium isopropoxide $Ti[(CH_3)_2CHO]_4$. 2-Methoxyethanol was used as the solvent to change metal acetate into metal alkoxide and to facilitate dehydration [4].

A mismatch of thermal expansion between PLZT film and substrate can result in cracking.[1] For thicker films (> 100 nm), the interfacial layer (e.g. TiO_2) must be deposited. The PLZT solution was layered on BK7 and TiO_2/BK7 by spin coating using a spinner rotated at a rate of 5000 rpm for 40 seconds. After coating the substrate, films were dried and crystalized at 250°C and 550°C respectively. Finally, the silver top electrodes were e-beam evaporated using a shadow mask. Thickness and morphology of the PLZT films were determined using a Veeco interferometric profiler.

Figure 1 shows plotted X-ray diffraction (XRD) patterns measured from the lanthanum doped PZT film. The

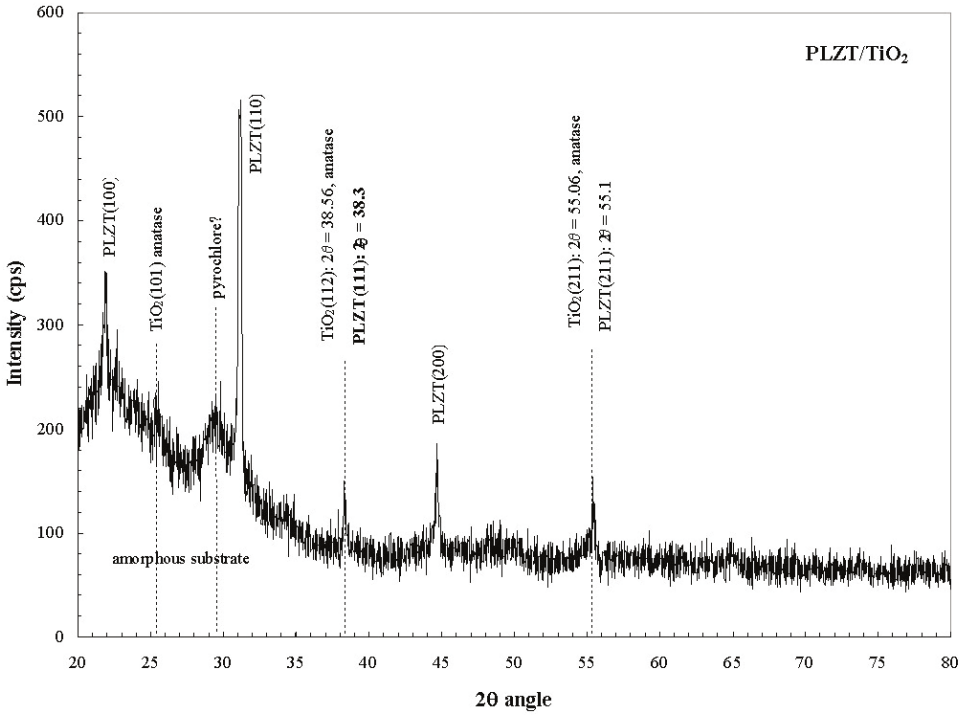

Figure 1. XRD measurement plot for PLZT 9/65/35.

prominent peaks of PLZT corresponding to (100), (110), (111), (200) and (211) have been identified in the figure. The diffractogram contains a broad peak near 2 =29° that can be identified as lead deficient (vaporisation of PbO) pyrochlore phase [5]. Figure 2 shows the surface profile measured by the Veeco interferometric profiler. The film surface is very flat (roughness <1 nm) and crack-free.

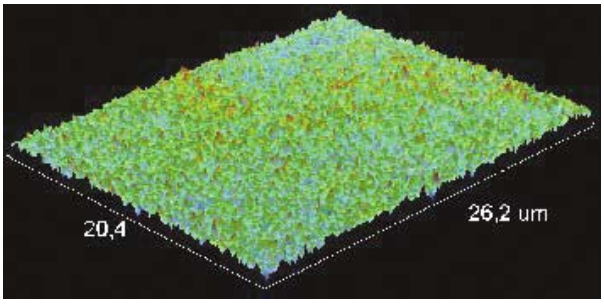

Figure 2. Surface (20.4 µm x 26.2 µm) image of 100 nm PLZT film (RMS <1 nm).

OPTICAL CHARACTERISATION

Characterisation of optical properties consists of the determination of refractive index and its shift under applied electric field. A prism coupling method was used in index measurements. The refractive index is 2.4 at 633nm and 2.2 at 1.55µm wavelength. This can be utilised in high index-contrast structures allowing the design of waveguide components within a small area [6]. The Kerr effect is the most attractive property of these films. It means quadratic dependence of refractive index on the applied electric field, and it was measured by an ellipsometric method similar to the one proposed by Adachi et al [2]. At first laser light emitted from the HeNe-tube (633nm) is modulated with chopper. Then light goes through the polarizer, which is at an angle of 45° relative to the sample having a narrow slit between electrodes. When 45° polarized light propagates through birefringent film, its polarization state turns elliptic. A /4 retarder plate turns the polarization state back to linear, but the angle is now different from 45°. The phase difference occurring in a sample induced by the applied electric field is two times the angle shift of the linear polarization. When this small shift is known, induced birefringence shift can be calculated. The result is shown in Figure 3.

The strength of the second order electro-optic coefficient is defined as

$$\Delta n = \frac{1}{2} n^3 R E^2$$

where n is the refractive index, R electro-optic coefficient, and E electric field. For plotting in Figure 3 $R=0.3*10^{-16}$ m^2/V^2. When this value is compared to the coefficients of sputtered samples ($0.6\text{-}1.0*10^{-16}$ m^2/V^2), it is smaller [2]. However, when it is compared to conventional $LiNbO_3$ materials, which possess first-order electro-optic effect, the birefringence shift is at 2kV/m electric field larger [7].

CONCLUSIONS

Sol-gel process is a potential method for manufacturing PLZT thin films with small surface roughness. These films have strong second order electro-optic effect and a high index of refraction. The results find that PZT films are promising materials as a candidate for nonlinear optical applications.

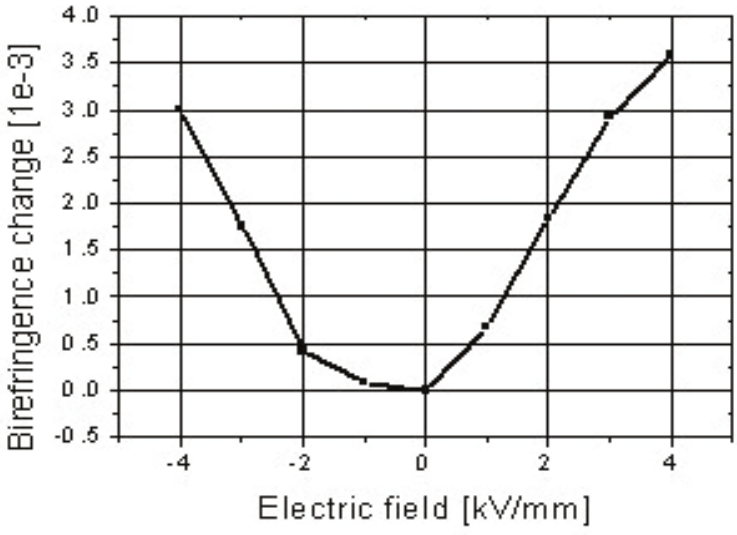

Figure 3. Birefringence shift of sol-gel processed PLZT film.

REFERENCES

1. Y. Guanghua, W. Zheng and M. Sayer, “Preparation of $Pb(Zr,Ti)O_3$ thin films by sol gel processing; Electrical optical, and electro-optical properties”, J. Appl Phys, Vol 64, pp. 2717-2724, 1988
2. H. Adachi and K. Wasa, “Sputtering Preparation of Ferroelectric PLZT Thin Films and Their Optical Applications”, IEEE Transactions on Ultrasonics, Ferroelectrics and Frequency Control, Vol 38, pp. 645-655, 1991
3. J. Lappalainen, V. Lantto, J. Frantti and S. A. Ivanov, “Optical Properties and Surface Morphology of Pulsed-Laser-Deposited Poly-crystalline PNZT Thin Films”, Journal of the European Ceramic Society, Vol 21, pp. 1585-1588, 2001
4. L. C. Klein, “Sol-gel Optics: Processing and applications”, Chapter 12, Kluwer academic publisher, Massachusetts, 1994
5. S. Iakovlev, C.-H. Solterbeck, A. Piorra and M. Es-Souni, “Processing and Characterization of solution deposited $Pb_{1.1}(Zr_{0.58}Fe_{0.2}Nb_{0.2}Ti_{0.02})O_3$ Thin Films”; Thin Solid Films, Vol 414, pp. 216-223, 2002
6. C. Manolatou and H. A. Haus, “Passive Components for Dense Optical Integration”, Kluwer Academic Publisher, 2002
7. H. Nishihara, M. Haruna and T. Suhara, “Optical integrated circuits”, McGraw-Hill Publishing Company, 1989

Jyrki Lappalainen
Microelectronics and Materials Physics Laboratory, University of Oulu, Finland

Jussi Hiltunen
Jussi.Hiltunen@vtt.fi

Markus Tuomikoski
Markus.Tuomikoski@vtt.fi

Zero-alignment Offner-Relay Housing by 5-axis CNC Machining

INTRODUCTION

The Optoelectronics Department of VTT Electronics has developed expertise in CNC machining of complicated, three-dimensional, mechanical bodies used in optical assemblies. A principal advantage of mounting lenses and mirrors into a CNC machined, rigid housing is the potential elimination of manual alignment steps. Other advantages include the ease and low cost of producing copies; and the complete, digital documentation of both shape and manufacturing processes in the form of the CNC program.

A challenging application is the machining of a zero-alignment housing for Offner-type imaging spectrographs. In order to investigate the feasibility of this application, VTT designed, built, and tested a solid housing for an Offner-type 1:1 relay optics with similar mechanical proportions. The optical performance of the relay was measured and used to estimate the worst-case mechanical deviations of the housing. The annular contact rims machined for the mirrors were accurately located within better than approx. ±10 µm of their nominal positions. This performance is sufficient for most, if not all, practical applications of Offner-type optics.

OFFNER RELAY MADE FOR TESTING

The optical design of the Offner 1:1 relay is shown in Figure 1. The simple design consists of three spherical mirrors; one small convex mirror (R=71.8mm, ∅42mm) and two identical, concave mirrors (R=140.13mm, ∅82mm). The nominal optical performance, i.e., best case with zero tolerances, is documented in the spot diagram.

ZEMAX reports a spot radius of 5.6 µm rms at best focus, with the spot being elongated in the horizontal (input↔output) direction. It is important to realise, however, that this simulated value is just that, a software simulation, and that values as high as 6.9 µm and as low as 4.8 µm can be produced by just decreasing and increasing, respectively, the so-called 'ray density' of the diagram.

The optical design was exported from ZEMAX into IDEAS using the STEP format. The mechanical design of the housing was performed using the optical surfaces as 'cutting tools'. Using STEP again, the mechanical design was exported from IDEAS into MASTERCAM. The actual parts were made on a 5-axis CNC machine (Bridgeport VMC800 L22 Digital) equipped with a 200mm Tilting Rotary Table (NST 5AX-200, Nikken Kosakusho, Osaka). The least accurate of the machine movements was the tilting of the rotary table, which was specified with an indexing accuracy of 1 minute (0.016,7°) and a repeatability of ±0.1 minute. The housing was machined as a single piece, in a single chucking, out of a block of so-called tool aluminum. The size of the finished housing was approx. 220 x 110 x 145(height) mm^3. High-quality mirrors (custom-made by Melles-Griot; BK7 substrates, gold coated) were dropped into the housing and spring-loaded against the contact rims with zero manual alignment. The unit is shown in Figures 2a, 2b and 2c. To simplify the testing, a baseplate and holders for input and output optics were also machined.

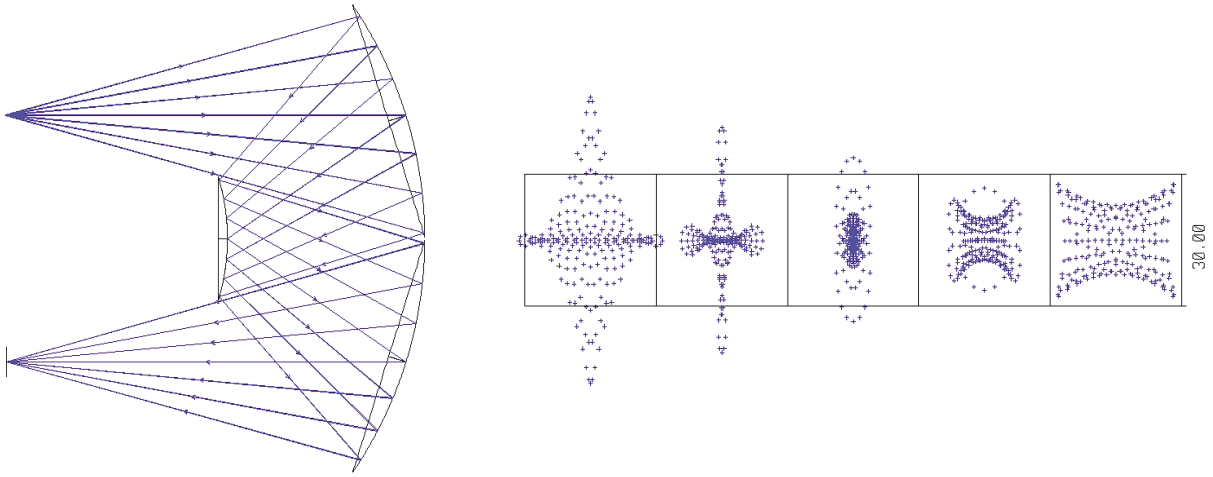

Figure 1 The Offner Relay Optics. The raytrace diagram on the left illustrates the layout. The distance between input and output is 83.2 mm. NA is 0.27. The size of the boxes in the through-focus spot diagram is 30 µm square and the defocus of the boxes is −50, −25, 0, 25, and 50 µm.

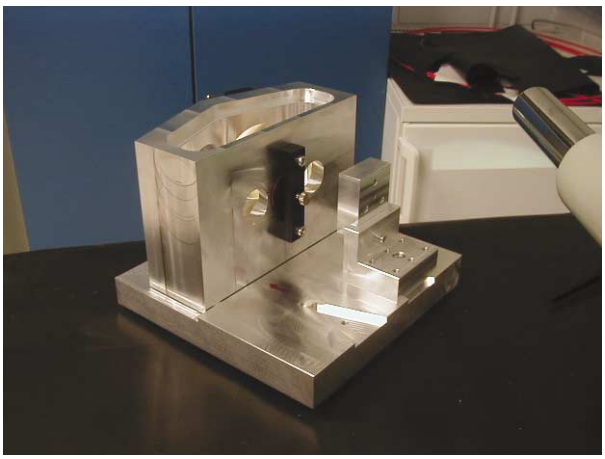

Figure 2a The Offner Relay with mirrors mounted, on its baseplate. The baseplate is 24 x 24 cm². One of the holders used in the testing can also be seen. All parts were CNC-machined at VTT Electronics.

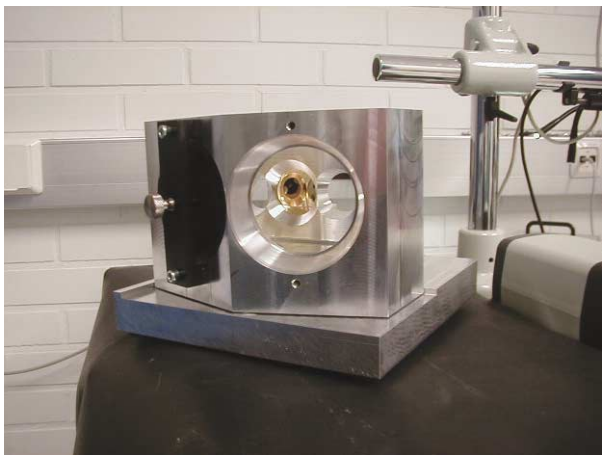

Figure 2b Backview with two mirrors mounted. Gold coating of small mirror visible. Mirrors are spring-loaded against precision-machined, circular contacts.

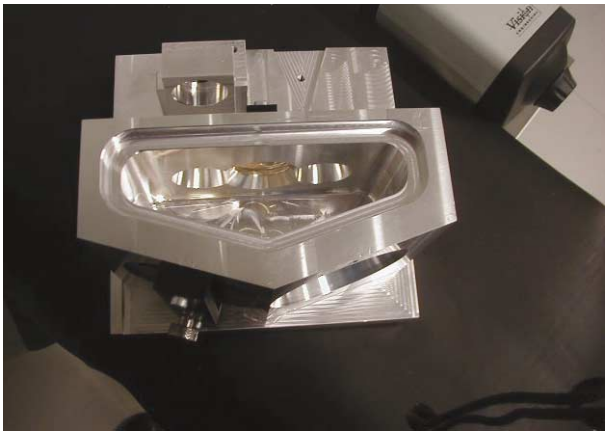

Figure 2c Top view with lid removed.

EXPERIMENTS AND RESULTS

In a first attempt to measure the achieved mechanical accuracy of the housing, the angle between the two annular contact rims machined for the two large spherical mirrors was measured. For this test, plane mirrors were contacted and the angle between them was measured on a Goniometer III (Möller-Wedel, Hamburg). The measured value was 34.513° with precision ±0.002°, which is approx. 0.022° larger than the nominal value of 34.491,1°. (In the ZEMAX design, the angle between the spherical mirrors is 34.576,2° but because of the shape of the contacting rims, this nominal value decreases slightly when contacting *plane* mirrors.) The accuracy of this goniometer test was compromised, however, by stress-induced bending of the plane mirrors, which were cut from 4 mm thin glass plate and loaded against the contact rims by using the same springs that had been designed for the much thicker spherical mirrors. Rourk-formula estimation of the bending induced by the approx. 2 to 3 kg of spring force applied via ∅70mm O-rings to the back of the mirrors, showed that the springs had caused an increase in the measured angle on the order of 0.01°, or roughly half the measured difference of 0.022°.

Mechanical testing proved difficult because features had been machined into opposite sides of the housing (and using the same CNC machine for coordinate measurements was obviously not an option in this case). Therefore, it was decided to measure the *optical* performance of the unit instead and then use a process of 'inverse sensitivity analysis' to estimate backwards, and determine how closely the mechanical dimensions were met.

Optical performance of the relay optics was measured by mounting a pinhole or slit at the input and observing the quality of the image at the output. The pinhole or slit was mounted close to its nominal position by using a mechanical holder of the type shown in Figure 2a, and the optics observing the output image was manually focussed for minimum spot size.

In a first test, the image of a pinhole was recorded on a CCD camera (PCO, 12 bit, 6.7 µm pixels) equipped with a homebuilt 40x microscope objective, see Figure 3. Images were taken at a short exposure time of 2 ms to minimise vibration effects.

The pinhole was nominally ∅10µm which, because of diffraction, appears as 13.5 ±0.5µm when viewed with visible light. [Radius of Airy disk to 1st dark ring is $z \cong 0.61 \cdot (0.55\mu m)/NA$.] The measured width of the spot image was

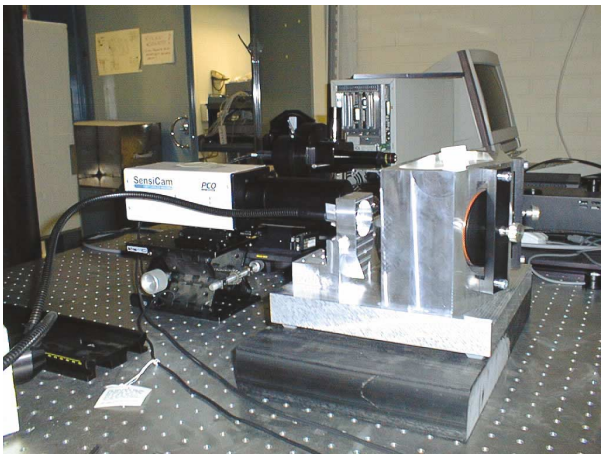

Figure 3 The Relay Optics mounted for the pinhole imaging test.

FWHM ≅ *78 pixels* · (6.7 µ*m*/*pixel*) ÷ 40 ≅ 13.07 µ*m*. Assuming the image is approximately Gaussian, this corresponds to an RMS radius of about 13.07 ÷ 2.35 = 5.56µ*m*, which is *smaller* than the nominal spot value of 5.6µm rms reported by ZEMAX (compare discussion of Figure 1). According to the laws of physics, opto-mechanical tolerances, diffraction, and the finite width of the pinhole itself (10/√ 12 ≅ 2.89µ*m rms*) should all add to the nominal and produce a value *larger* than 5.6µm rms. The conclusion was that the optical performance was so good that the small deviation from the nominal could not be detected by using the simple process of root-sum-of-squares subtraction of measured and simulated spot widths.

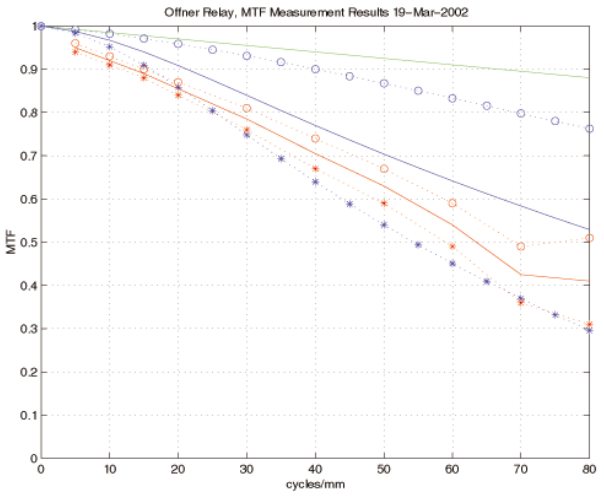

Figure 4 Summary of the MTF results. Diffraction limit for NA=0.27 (green); nominal design assuming zero mechanical and optical tolerances (blue); and measured performance (red). Dots (o) indicate horizontal slit (pointing input↔exit); stars (*) indicate vertical slit; and solid lines are averages of the two.

The modulation transfer function is a much more sensitive indicator of small deviations from the ideal, diffraction-limited, imaging performance. In a setup similar to the one shown in Figure 3, the MTF of the relay was measured on an MTF Test Station (Image Science Ltd., Chalgrove, Oxford, England). Microscope objective was 4x and slit width was 8 µm, giving a useful frequency range up to 80 cycles/mm. Results are summarised in Figure 4 and show that the relay performed very close to its nominal design.

For the inverse sensitivity analysis, ZEMAX iteratively increased *individual* mechanical tolerances until the simulated MTF at 50 cyles/mm had dropped to the measured value of 0.62, see Figure 4, allowing focus adjustments. The results are summarised in Table I.

The values listed in the ”minmax” column of Table I are minimum-maximum values in the following sense. First, the values are *minimal* in the sense that each value summarises the sensitivity results of several degrees-of-freedom of mechanical movement. For example, the first row, *X-,Y-position of the vertices of the two large mirrors*, has four DoF's because two mirrors can shift into two directions. Since shifts can be to the (+) or (−) side, the inverse sensitivity analysis produces a total of eight ΔX-, ΔY-values, each individually sufficient to degrade the MTF to 0.62. The value, 12 µm reported in Table I, is the *minimum* of the eight absolut values, i.e., it represents the most critical tolerance. (Many of the other seven tolerances, which are not listed in Table I, are more than 2x less critical.) Second, the reported values are *maximal* because each number is computed assuming that the individual mechanical tolerance is responsible for *all* of the observed degradation in MTF, whereas all other mechanical tolerances and all optical tolerances (radii and surface figures) are assumed to be zero. Clearly, by putting all the blame onto the single tolerance under study, the reported value is increased and the numbers in Table I are worst-case estimates in this sense. Now, if we assume that the mechanical features addressed in each row of Table I can be CNC machined with equal difficulty or ease, then the minmax values can be used to make conclusions such as: ”The housing was machined accurately enough to position the vertices of the two large mirrors to within better than ±12 µm of their nominal X- and Y-positions;” and so on for the other rows of Table I.

Table I Mechanical Tolerances Estimated by Inverse Sensitivity Analysis
Note: X-axis is perpenticular to the plane of the paper in Figure 1; Y- and Z-axes are local to the mirrors and attached to their vertices, with the Z-axis pointing in the direction of the optical axis. DoF = degrees of freedom.

	DoF	"minmax"	"likely"
X-,Y-position of the vertices of the two large mirrors	4	12 µm	± 7 µm
X-,Y-position of vertex of the one small mirror	2	125 µm	(")
Z-distances, small-to-large mirrors	2	26 µm	± 15 µm
X-,Y-tilts of the two large mirror	4	0.005°	± 0.003°
X-,Y-tilt of the one small mirror	2	0.10°	(")

The values listed in the 'likely' column of Table I are an attempt to estimate the achieved accuracy more realistically, as $minmax/\sqrt{3}$, i.e., by arbitrarily assuming that three tolerances are equally responsible for the MTF degradation. Since the tolerances of the small mirror have only a relatively small effect on optical performance, their limits cannot be effectively estimated by the inverse sensitivity process. However, it is reasonable to assume that accuracies are similar to the ones achieved for the larger mirrors, and this is indicated with the (") signs in Table I. The tilt tolerance of ± 0.003° of the larger mirrors is equivalent to an 'edge-to-edge' tolerance of $82mm \cdot \tan(=0.003) \cong \pm 4\ \mu m$.

SUMMARY AND CONCLUSIONS

A zero-alignment, rigid housing for an Offner-type 1:1 relay optics was machined using a 5-axis CNC machine. The part was machined in a single chucking out of a block of tool aluminum and contained three annular contact rims against which the spherical mirrors were mounted using spring-loading, thereby eliminating any manual alignment of the mirrors. The optical performance of the relay was measured on an MTF test station and was close to the nominal design which, in turn, was close to the diffraction limit. An inverse sensitivity analysis showed that the mechanical features of the housing had been accurately machined to within better than approx. ± 10 µm from their nominal positions.

For imaging-spectrograph type applications, in which the small mirror is replaced with a grating, the result of this report means that manual alignment can be reduced to (i) rotational alignment of the grating grooves and (ii) focussing of the focal plane array, depending on the tolerances of the FPA chip relative to its outside package.

Some final remarks concern the opto-mechanical design process. Close cooperation between the designer of the part and the CNC operator is necessary in order to insure that the housing is within the operating limits of a particular CNC machine. The range of tilt of the rotary table, which is typically around 120°, limits the complexity of the features that can be machined in a single chucking, into opposite faces of a part. It is likely that the aluminum block needs to be mounted in an angled jig in order to better utilise the available range of tilt. Tools with a larger than 90° point angle are helpful in this regard.

Ralf Marbach
Ralf.Marbach@vtt.fi

Tomi Seppänen
Tomi.Seppanen@vtt.fi

Pekka Suopajärvi
Pekka.Suopajarvi@vtt.fi

Optical Interconnects on Printed Wiring Board

ABSTRACT

Future wiring boards may include optical transfer lines in addition to conventional copper striplines. This development is driven by the ever-increasing performance and integration density requirements that probably cannot be fulfilled feasible with electrical interconnects but are seen achievable with optical interconnects. In the OHIDA project, electronics design and manufacturing technologies for the integration of optical transfer lines into printed wiring boards (PWB), as well as for the packaging and assembly of optical transmitters and receivers onto the boards, are studied and developed.

INTRODUCTION

With ever-increasing processor clock frequencies and telecom data rates, the performance of electrical interconnects inside equipment creates a bottleneck. The performance of electrical interconnects has many physical limitations, for instance, due to dispersion, electromagnetic emission, and susceptibility against electromagnetic radiation. However, optical interconnects have a very high bandwidth and are also insensitive to EMI/EMC problems. Fibre (ribbon)-based optical interconnects are already used in rack-to-rack and board-to-board applications, but they do not meet the low-cost and high-integrability requirements for board level and shorter distances. Free-space optical interconnects have been widely studied but so far have only shown potential for very short-range intra-chip and intra-MCM (multi-chip module) applications. However, optical interconnects based on integrated waveguides are a promising solution to overcome the interconnection bottlenecks at board and module level.

Most likely, novel technology with high-bit-rate optical interconnects has to be developed based on existing PWB technology instead of developing a completely new one. The stripline-like optical waveguide approach fulfils the integrability and compatibility requirements of PWB technology and enables design techniques analogous to the ones used for wiring electrical signals. This leads to hybrid optical–electrical boards (OE-PWB) with optical waveguides embedded in the board as additional optical layers, see e.g. ref. [1]. In this paper, some key technological challenges and potential solutions are reviewed.

The objective of the OHIDA (Optics on future printed circuit board in high speed data transmission applications) project (2002–2004) is to develop technologies to integrate high-speed (~10 Gb/s/channel) optical interconnects into conventional (FR-4) PWBs with dimensions of up to 50 cm. This includes studies of the potential technologies, including high-speed electronics and optoelectronics, packaging and optical coupling concepts for the transmitters and receivers, as well as materials and processing for optical waveguides. In the second phase, the design and manufacturing processes of OE-PWBs and the attaching techniques for optical components will be developed to be more suitable for board production and assembly processes. Suitable technologies and processes will also be demonstrated and tested.

DEVICES

The electronic and optoelectronic component technologies suitable for short-distance optical interconnects up to 3 Gb/s/channel are commonly available, and 10 Gb/s devices are emerging. Although almost all components are designed for fibre-optic links (being the only volume application so far), most of them are also suitable for OE-PWBs – directly or after a small modification. In addition, the customised packaging of transmitters and receivers for the chosen optical coupling scheme need to be developed to enable compatibility and feasibility for the assembly process and to ensure that the reliability criteria are met.

Probably the most suitable emitter devices for OE-PWBs are vertical-cavity surface-emitting lasers (VCSELs), emitting at around an 850-nm (or 970-nm) wavelength. Monolithic VCSEL arrays allow high interconnection density and have shown the required reliability and the potential to become a low-cost technology. Currently, 3 Gb/s VCSELs are available as arrays and 10 Gb/s/channel arrays are emerging. The optical receivers will be based on photodiodes or metal-semiconductor-metal (MSM) diodes with integrated pre-amplifiers. Suitable detector technologies exist, but optimisation in terms of bandwidth and active area would be required to maximise the performance in OE-PWB applications. To allow better alignment tolerance in optical coupling between waveguide and detector, as large a detector area as possible is preferred; but increasing the area of the detector increases its capacitance, which results in decreased receiver bandwidth and increased pre-amplifier noise. MSMs are probably better than PINs, since a larger photosensitive area-receiver sensitivity product is possible at the same bandwidth. Nevertheless, there is a much better selection of PINs available than MSMs, because in fibre applications the smaller area of PINs is often sufficient.

OPTICAL WAVEGUIDES

In addition to excellent optical properties, the important requirements of hybrid optical–electrical board technol-

ogy, from the materials and manufacturing point of view, are structural integrity and multi-material compatibility. The use of polymer based materials for optical waveguides offers several advantages over inorganic materials, like low-cost, high endurance and the possibility for mass production with relatively low processing temperature, giving a higher degree of freedom in design and applications. Polymer-based waveguides can be implemented using process techniques compatible with PWBs, for instance, for patterning photolithography and etching, embossing or moulding techniques are possible. Unfortunately, only a few of the PWB-compatible polymer materials have potentially feasible optical properties. However, new materials have recently been released that exhibit very low waveguide attenuation, even less than 0.05 dB/cm. Embedded waveguide concepts compared to overlaid schemes are seen as more favourable because otherwise optics will lower the packaging density by occupying surface space. An additional waveguide layer offers transparency to the system integrator if it is compatible with the standard multilayer lamination process.

PWB may include multiple optical layers, but this feature probably cannot be exploited in routing optical transfer lines, since low loss optical 'vias' are very difficult to implement. However, routing is possible on a single optical layer as crossovers with low loss and crosstalk can be made with optical waveguides (on the contrary to electrical stiplines). Waveguide technology also allows the integration of passive optical structures, like splitters and combiners, to provide multipoint connections.

The dimensions of the waveguides need to be sufficiently large, in the order of 50 microns or bigger, to ease alignment tolerances for optical coupling. Such waveguides will be highly multi-modal. There are several simulation and design tools for optical waveguides, but they are based on the analysis of individual optical modes, which is only practicable for small waveguides, not highly multi-modal ones. However, the conventional optical analysis approach, ray tracing, is applicable. For such analysis, Monte-Carlo ray tracing is the most powerful general tool and can be interpreted using commercially available software, like ASAP (by Breault Research Organization Inc). The waveguide structure, even with surface roughness, can be modelled. In addition, ray tracing allows analysis of the impulse response of the optical channel and is an excellent tool for the analysis of optical coupling.

OPTICAL COUPLING – PACKAGING

Another key challenge is to provide efficient and robust optical coupling between the waveguides and the optoelectronic devices, i.e. transmitters and receivers – suf

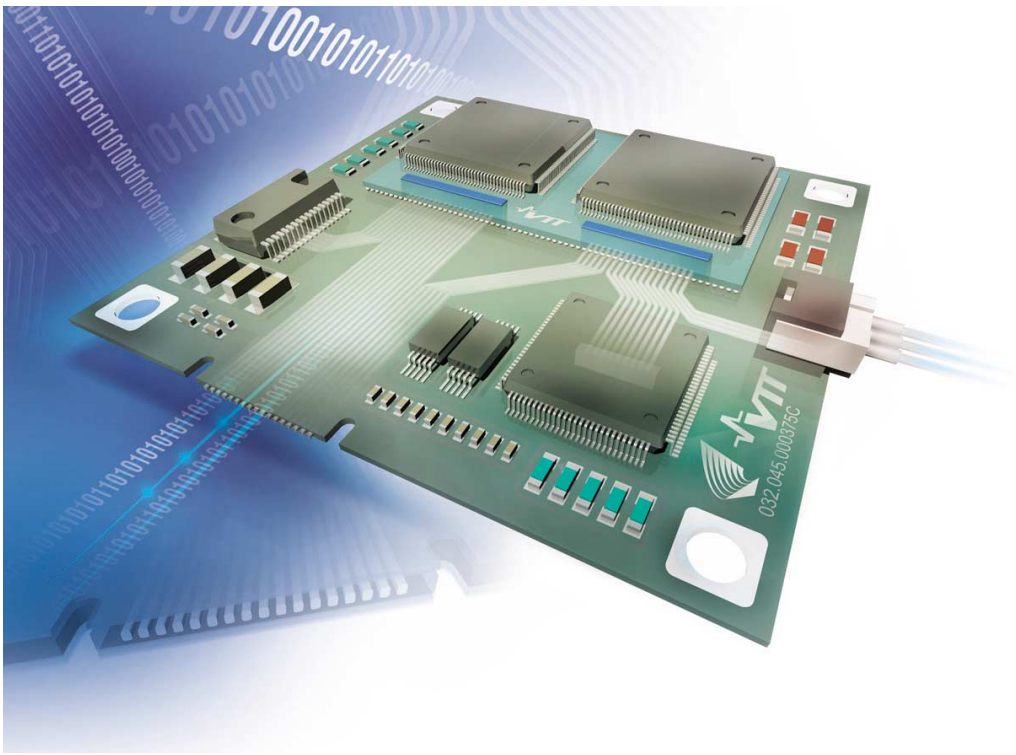

Figure 1. A vision of future optical–electrical printed wiring board.

ficient optical alignment should be achieved by the pick-and-place assembly of the components. This is in order to be compatible with automated electronics manufacturing processes. A simple approach is butt coupling, in which the optoelectronic devices, i.e. emitters and detectors, are placed facing directly towards the waveguide ends (Figure 2a). This scheme requires a special package with optical sub-assembly entering a via or cavity on the board, and the necessary alignment accuracy is defined by the dimension of the VCSEL, detector and the waveguide. The optical alignment requirements may be relaxed and the coupling efficiency improved by the use of optics based on micro-optical elements, such as, lenses, prisms, mirrors and diffractive optical elements. They also allow the use of packages suitable for standard surface assembly methods (Figure 2b). The expanded beam method enables loosening the tolerance requirements, e.g. between the package-to-alignment in Figure 2b, but the use of the method is limited by the channel pitch of the parallel interconnects, which is typically 250 µm in VCSEL arrays.

The cross-sectional dimensions of optical waveguides should be optimised based on the chosen coupling scheme and the properties of the emitter and detector, as well as achievable alignment tolerances. To simplify, the bigger the waveguide, the easier it is to couple from VCSEL to waveguide, and on the contrary, the more difficult it is to couple from waveguide to the detector. In practise, a reasonable waveguide cross-section is approximately the same as for those of microstrip lines, i.e., 50... 100 µm, which also allows high interconnection density. Typically, the resulting alignment accuracy requires that the components are in the order of 20...50 µm or smaller, which is very challenging but probably achievable with today's high-end assembly techniques. In addition, tilts of devices (i.e. angular misalignments) have to be rather small with optics – an aspect with not much importance in traditional electronics assembly.

Considering the assembly of the devices, there are also practical issues not covered by previous studies. The underfill materials are an example; if, for device reliability reasons, underfills have to be used below an optically interconnected component, the material should be optically transparent and also taken into account in the optical design. Actually, the use of underfills may also be necessary for the optical channel, as they would prevent dust or moisture from disturbing the channel.

PERFORMANCE

At 10 Gb/s, the allowed optical loss between emitter and detector is in the order of 10 dB, or a bit more with state-of-the-art devices, to maintain a very low bit-error rate. Such optical power budget probably enables transfer lines at board level distances with state-of-the-art polymer waveguides and minimised coupling losses. Nevertheless, only a small splitting ratio (1-to-2...4) multipoint interconnects are possible, and even this will require very low waveguide attenuation or short links (a few centimetres or less). The data rate maximum of 10 Gb/s is defined by the bandwidth of suitable optoelectronic devices – not by the transmission media, as bandwidth of multi-mode waveguides can be much higher. Since the limits of device technologies are not yet reached, even higher speeds may be possible in the future, though with the cost of a smaller power budget.

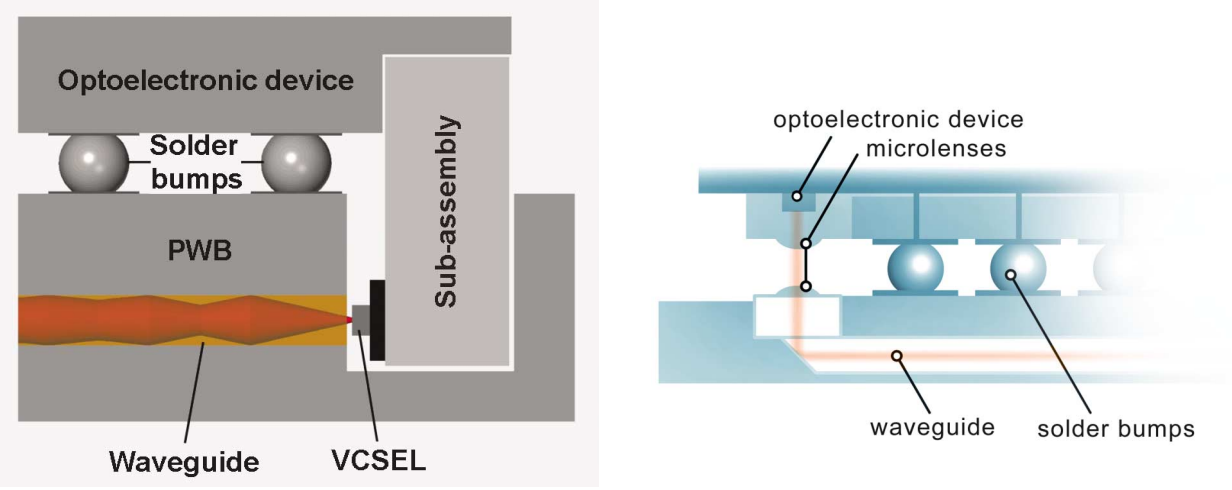

Figure 2. Examples of optical coupling schemes between an optical transmitter/receiver in a BGA-package and a waveguide integrated into PWB: a) butt coupling; b) expanded beam coupling via mirror.

The state-of-the-art level for the electric interconnects is 10...12 Gb/s with four serial lines each operating up to 3.125 Gb/s. With suitable equalisation techniques, the transmission distance of 0.5 m seems to be within reach, even with FR-4 as a substrate material. Even 10 Gb/s has been demonstrated based on adaptive equalisation and minimisation of impedance discontinuities. At very high data rates, optics allows better performance and higher density (less board area needed for transmission lines). If the system is power critical, the electrical option usually needs less power, especially at smaller speeds and transmission distances. As the optical waveguides can be placed close to each other without crosstalk and the interfaces can be made small, substantial space savings can be achieved even in small transmission distances. If the application is EMI/EMC critical, the optical option is more favourable.

CONCLUSIONS

Embedding optical waveguides into electric wiring boards leads to optical–electrical hybrid boards. The optical layers with waveguides can be made of polymer materials with extra processing steps using standard patterning methods, such as photolithography, to ensure compatibility with the electrical board manufacturing processes. The high-bandwidth optical waveguides transmit signals from surface-emitting laser chips to photodiodes, which can be heterogeneously integrated into micromodule or silicon chip packages. The optical coupling between the transmitter/receiver and the waveguide can be enhanced with micro-optical components, but nevertheless, stringent mechanical accuracy requirements are probably set for packaging and assembly. Although suitable components and waveguide materials are available and some functional concepts have been demonstrated, research is still needed to develop packaging, processing and design practices to achieve feasibility for mass-production as well as to confirm reliability issues. In addition, new design rules and algorithms are needed that can fully exploit the advantages of hybrid board technology.

ACKNOWLEDGEMENTS

The partners of the OHIDA project are Aplac Solutions, Asperation, Aspocomp, Elcoteq Network, Perlos, as well as Helsinki university of Technology (Laboratory of electronics production technology) and VTT Electronics. OHIDA is funded by Tekes (National Technology Agency) under the ELMO research program.

REFERENCES

1. E. Griese, “A High-Performance Hybrid Electrical–Optical Interconnection Technology for High-Speed Electronic Systems,” IEEE Transactions on Advanced Packaging, Vol. 24, No. 3, pp. 375–383 (Aug 2001).

Mikko Karppinen
Mikko.Karppinen@vtt.fi

Antti Tanskanen
Antti.Tanskanen@vtt.fi

Kari Kataja
Kari.Kataja@vtt.fi

Jussi Hiltunen
Jussi.Hiltunen@vtt.fi

Jukka-Tapani Mäkinen
Jukka-Tapani.Makinen@vtt.fi

Marika Immonen, Riia Lankinen, Jorma Kivilahti
Helsinki University of Technology

Printable Electronics, Optics and Optoelectronics

ABSTRACT

The integration of electrical, optical and optoelectrical components into products such as disposable packages and printed matter requires new, cost-effective and volume scale capable manufacturing techniques. VTT Electronics has, together with VTT Information Technology and Finnish universities, launched the Printo-project in Tekes' (the National Technology Agency) ELMO-program, the main goal of which is to develop roll-to-roll and related volume-scale manufacturing technologies for the fabrication of electrical and optical components. Manufacturing technology and functional material development will be carried out in close relationship with Finnish industry.

1. INTRODUCTION

In the future, food packages will be smart enough to communicate actively or passively with kitchen appliances, helping them to understand how food must be stored, whether the contents of the package is all right, and what additional foodstuff will be needed to prepare a delicious dinner. Furthermore, shipping boxes will never get lost because they will always know where they are and where they are heading. They will also recognize right or wrong handling, so the shopkeeper or consumer will have the right address for the delivery of a credit note. These are just two of the more modest visions helping to drive the development of inexpensive printable electronics, optics and optoelectronics.

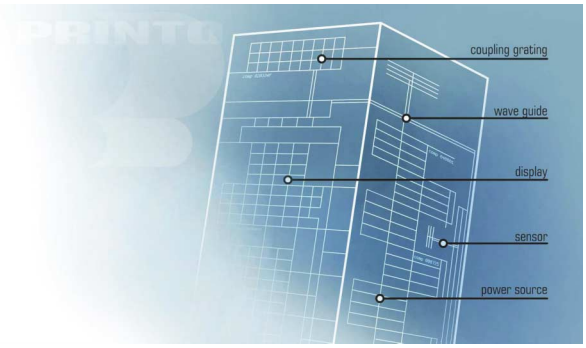

Figure 1. An active package containing a simple display element, power source, the required electrical components for energy transfer and switching, optical impressive elements and a sensor.

What is needed to fulfil these visions is a volume-scale manufacturing technology capable of producing electrical, optical and optoelectrical components at a unit price of only a few euro cents or even fractions of a cent. Optical and optoelectrical components, such as the various displays of organic LEDs, photodetectors like solar cells, lighting elements like optical waveguides, diffractive elements, and electrical components (conductors, resistors, coils and even switching elements, such as transistors) are needed to realize even simple entertaining, impressive or guiding effects. However, in most cases the technologies for manufacturing these components currently require inflexible substrates, not suitable for use in packaging or printed matter.

The Printo project is seeking to evaluate roll-to-roll related mass production techniques such as gravure printing, embossing, digital printing and offset for the fabrication of optical, electrical and optoelectrical components. These components will be the building blocks for tomorrow's active packages. The recent development of electrical and optical polymeric, inorganic and hybrid materials, as well as "inks" suitable for the above techniques, has made it possible to fabricate electrical, optical and optoelectrical components using roll-to-roll and related techniques. Therefore, electrical or optical inks for roll-to-roll manufacturing processes are also being tested, modified and developed. Moreover, during the project, consumers' interests in intelligent Printo-packages are defined using functional demonstrator concepts, realized at the University of Lapland, in the faculty of arts and design.

2. TECHNOLOGIES

In order to investigate the volume-scale manufacturing technologies for electronics and optics, printing methods such as gravure, hot-embossing, flexo, offset and ink-jet are investigated and evaluated, firstly by using simple table scale units. By using these table scale machines, simple electrical equipment (conductors, resistors) and parts of the active optical elements (cathodes for display elements, light guiding structures) are already demonstrated. In April 2003, a pilot production facility has been installed in clean room at VTT Electronics. This facility includes gravure (UV-, thermal- or IR-curing possibilities), hot-embossing and laminating units. The facility is capable of printing a 25 cm max. web width at a speed of 100 m/min max.

2.1. Electrical components

For the fabrication of electrical components, conductive polymer inks are realized and tested using gravure, flexo and off-set techniques during the project at VTT TTE/microelectronics. Inks suitable for gravure, off-set and ink-jet techniques (VTT TTE/media) are fabricated and test structures, including conductors for example, are realized. However, there is limit to the conductivity of the polymeric materials and, for example, coils are impos-

sible to realize using polymeric material. Therefore particulate silver-containing inks are used in applications where high electrical conductivity is needed. Silver-containing inks and their printability properties are investigated at the University of Oulu, in the microelectronics laboratory.

2.2. Optics

The easiest way to fabricate an impressive effect is to use diffractive optics. Diffractive optical elements will be fabricated using the roll-to-roll hot-embossing method. The hot embossing technique is already realized for the fabrication of light guiding structures and diffractive elements (including optical ROM). Hot embossing tests are carried out at the University of Joensuu, in the department of physics in close co-operation with VTT Electronics.

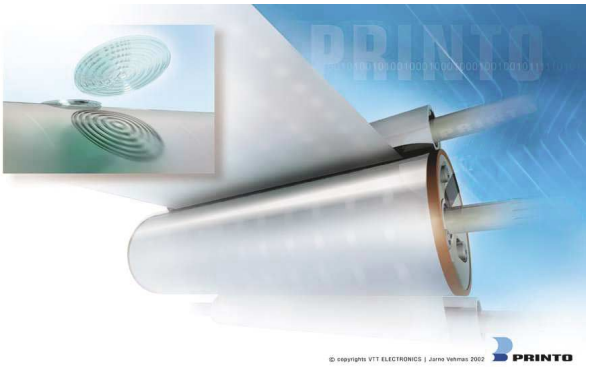

Figure 2. Hot-embossing roll-to-roll manufacturing method for optical elements.

2.3. Optoelectrical components

From the active package point of view, the most critical component is the display element. During the Printo project roll-to-roll manufacturing technologies for organic light emitting diodes (OLED) are investigated at VTT Electronics and VTT TTE/microelectronics. So far, functional one color OLEDs have been realized, partly using the roll-to-roll technique. Emitting devices also require energy. This energy will be created using dye-sensitized or organic solar cells (DSSC and OSC, respectively). Roll-to-roll fabrication of DSSC and OSC elements were also investigated during the Printo project. DSSC elements will be fabricated at the University of Jyväskylä, in the department of chemistry. During this project DSSC elements using conventional techniques have been fabricated. Material and manufacturing techniques realizing the roll-to-roll DSSC are under intensive investigation. The fabrication of OSC elements is directly related to the fabrication of OLED structures. Therefore, achievements with OLEDs have a direct contribution to the manufacturing possibilities of OSC elements.

3. CONCLUSIONS

During the Printo project, techniques and materials for the realization of intelligent and active packages have been investigated. Results, achieved to date, indicate clearly that roll-to-roll manufactured active and passive electrical, optical and optoelectrical components will be integrated into packages and printed matter in the future.

Terho Kololuoma
Terho.Kololuoma@vtt.fi

Harri Kopola
Harri.Kopola@vtt.fi
Tapio Mäkelä
VTT Information Technology, microelectronics
Jali Heilmann
VTT Information Technology, media
Tomi Haring
University of Joensuu, Department of Physics
Jani Kallioinen
University of Jyväskylä, Department of Chemistry
Juha Hagberg
University of Oulu, Microelectronics Laboratory
Ilkka Kettunen
University of Lapland, Faculty of Art and Design

2.4 GHz LTCC-Radio Module

LTCC-technology helps the progress of electronics integration and also offers improvement in high frequency performance. The benefit of LTCC-technology is in the high number of available dielectric and conductor metallisation layers in the substrate. Additionally, accurate conductor patterning is very good for the miniaturisation of electronic devices. The low dielectric and conductor losses of available LTCC-materials improve high frequency performance compared to FR4-boards. It was in VTT's interest to design a pilot application to have a conception of RF-circuit design and manufacturing matters in the LTCC-environment.

1. THE DESIGN OF THE RADIO MODULE

For the realisation of the radio module, an LMX 3162 integrated circuit from National Semiconductor was chosen. LMX 3162 is a 2.4 GHz ISM-band transmitter and receiver integrated circuit including phase locked loop (PLL) blocks. Common radio systems using 2.4 GHz band include Bluetooth, HomeRF and DECT. LMX 3162 has been designed only for non-linear modulation (FSK) use which keeps the design simple. Although LMX 3162 represents today's highly integrated radio chip, the fully functional radio module needs a separate RF-band filter, IF-SAW-filter, voltage-controlled oscillator (VCO), a couple of discrete transistors for RF-amplifiers and some conventional discrete passive components. The total component count is about 60. The block diagram of the radio module is presented in figure 1. The needed supply voltage for LMX 3162 and thus for the whole radio module is 3.3 V.

The radio module circuit design was based on the LMX 3162 application data sheets provided by National Semiconductor. The frequency synthesiser operates on 1.2 GHz and the frequency is multiplied by 2 inside the LMX 3162 to generate the needed 2.4 GHz local injection. This way the synthesiser is easier to realise and the current consumption can be reduced. The drawback is that the leaking 1.2 GHz fundamental frequency must be filtered out of the transmitter output.

The VCO-module used on the National Semiconductor's application data sheet was no longer available so an integrated circuit VCO from Maxim (MAX 2754) was selected instead. The replacement VCO also has an input for the generation of the direct frequency modulation. MAX 2754 is a very interesting VCO because of its small-size 8-pin package (3 mm x 5mm) including internally all but one needed supply voltage filtering capacitor. The minimum supply voltage for this VCO is as low as 2.7 V.

The low noise amplifier (LNA) and transmitter output amplifier both use a BFP 420 bipolar transistor that is very commonly used for this kind of purpose and thus is a cheap component. The RF and IF-band pass filters were available from Murata. The RF-filter is ceramic and the IF-filter is a surface acoustic wave (SAW) type.

Four tape layers of DuPont 951 general purpose LTCC-tape was chosen to form the needed substrate with 0.8 mm of total fired thickness and thus five metallisation layers available for conductor trace routings. It was decided to print conductor metallisation with the co-fireable silver paste and 130 um was used as the design rule for the minimum conductor trace width and space. That is a very conservative rule, and 100 um is nowadays an easily realistic value for printed conductors. The size of vias was chosen to be 200 um in diameter as it is easy to realise this by punching the LTCC tape. The via holes were also filled with silver paste before co-firing. The module was assembled in a standard SMD-reflow process.

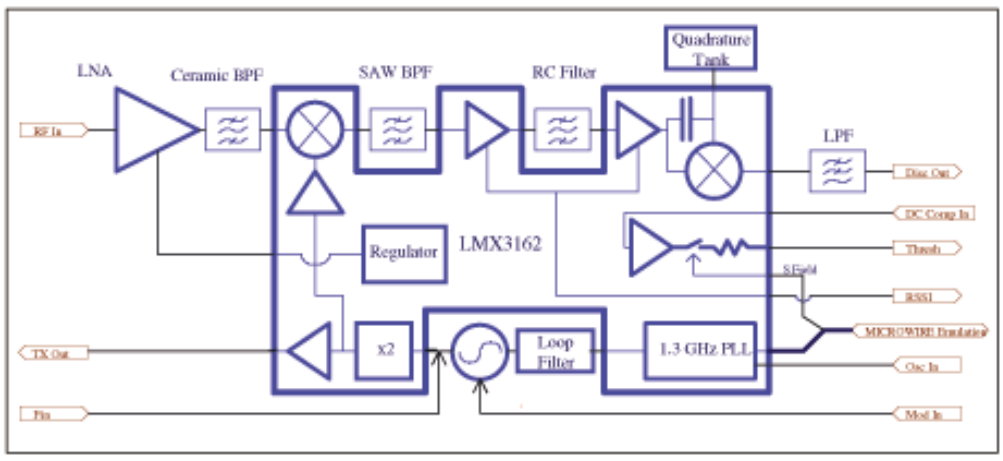

Figure 1. The block diagram of the 2.4 GHz radio module.

A photograph of the assembled module is presented in fig. 2. The needed substrate area of the module with the connectors is 28 mm x 33 mm. There are separate SMA-connectors for the receiver (RX), transmitter (TX) and local oscillator (LO) ports. The connector for the LO-port was included for prototype testing purpose only and could have been left out of the design. Two 8-pin miniature surface mount connectors were used for the supply voltages and all the needed I/O-signals. For prototype testing some extra pins were used although a smaller number of pins would have been sufficient for essential power supply and I/O-signals.

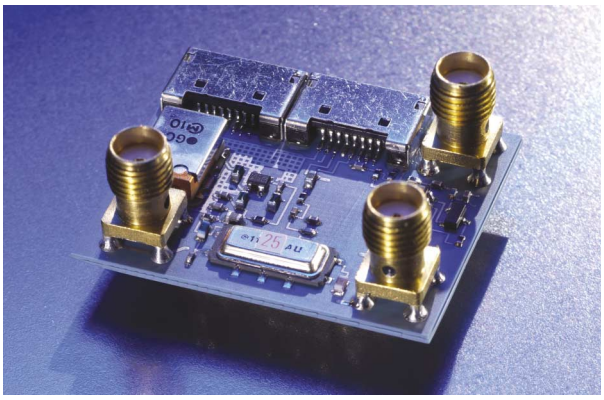

Figure 2. The photograph of the radio module.

2. THE TESTING OF THE RADIO MODULE

It was quite easy to get the radio module operating. PC software called Codeloader is available from National Semiconductor to load the digital control registers of the LMX 3162. A simple cable is needed between the computer and the module. The functionality of the frequency synthesiser was beforehand a little uncertain because of the replacement of the VCO with a previously non-tested type. That would cause a different VCO-factor in the closed-loop transfer function of the PLL and moreover it would have an effect on the performance of the whole frequency synthesiser. Fortunately, the synthesiser was seen to function reasonably well on the whole desired band 1.15 - 1.25 GHz without any loop filter modification. Without the optimisation of the loop filter, the phase margin and the bandwidth of the closed loop are, of course, not the best possible. In practice this means unoptimal phase-noise and setting time characteristics.

Fig. 3. presents the spectrum analyser picture of the transmitter output giving 5 mW RF-output power at 2.4 GHz. As can be seen, the output is fairly clean of noise but there are interference sideband carriers 10 MHz away from the wanted carrier. The interference carriers are caused by the 10 MHz reference oscillator of the PLL mixing with the 2.4 GHz local oscillator signal. This might be due to insufficient protection of the interference-sensitive signal routes. Because the reference oscillator signal was fed from an external source, it can, for example, couple to power supply wires because the perfect shielding of wires is not possible to realise.

The receiver tests showed its functionality. At first, the 110.6 MHz IF-chain had some instability, but that problem was solved by putting the whole radio module inside a metal box. The IF-chain has 85 dB of total gain, so it is no wonder that good shielding is necessary for stable operation. FM-receivers usually have very much gain in an IF-chain to get proper amplitude modulation (AM) rejection in the limiter stage. The receiver is a single-conversion type, and a quadrature detector is used for FM-detection after the IF-amplifier and limiter stages on 110.6 MHz IF-frequency. The sensitivity or intermodulation distortion (IMD) performance of the receiver was neither measured nor optimised.

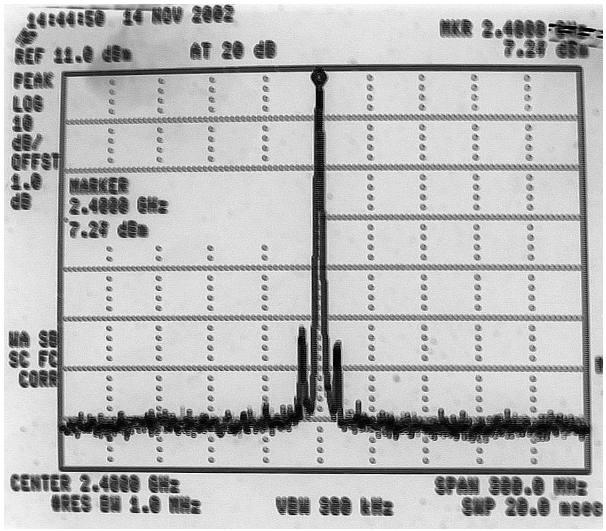

Figure 3. The spectrum analyser picture of transmitter output operating at 2.4 GHz.

Antti Vimpari
Antti.Vimpari@vtt.fi

Fine-Line Screen Printing in LTCC

INTRODUCTION

Conventional screen printing technology, using stainless steel mesh screens and silver based conductors, is the main low-cost manufacturing technique for conductor patterning in LTCC circuit manufacturing and will remain so in the near future. Screen printing has become a critical process in the manufacture of LTCC substrates. Traditionally, the minimum printed line width on ceramic substrates has been 100...125 µm in production. The need for higher packaging density has increased the importance of screen print quality and fine line capability. The increased number of RF/microwave LTCC applications has particularly emphasised the need for a high quality screen printing process, including finer lines and improved repeatability. In these applications the print quality characteristics, such as line width, line edge definition, print thickness and their tolerances, are crucial to the RF performance.

A smaller feature size will be necessary for certain designs at microwave frequencies and also for high density packaging needs in the future. The need for a higher interconnection density and better line definition has led to the increased use of photolithographic patterning methods instead of screen printing. A potential technique to address the requirement of finer lines and improved line definition, especially for microwave applications, is the photoimaging technique, which uses photosensitive thick film paste materials. Lines and spaces of 50 µm and even smaller are possible in a multilayer structure with a superior line definition to screen printed lines. These new materials are not yet widely used and their properties are not very well known. It is, however, clear that photoimaging will be used more in the future, in combination with screen printing, in those layers which are beyond the capability of screen printing alone. However, recent advances in screen technology enable a line and space of below 100 µm. These new possibilities should also raise the interest of material manufacturers in developing fine-line pastes for LTCC.

FINE LINE PRINTING

There are numerous factors that affect screen print quality, such as substrate material and flatness, paste properties, screen type and quality, type of squeezee, printer parameter settings etc. In LTCC technology, the substrate material itself is a flat and smooth tape sheet and as such an ideal base for fine line printing. The firing shrinkage of 10 to 15 % will further reduce printed line dimensions. The two most important factors in fine line printing process development for LTCC are the screen and paste properties.

For fine-line printing of thick film conductors, the quality of the screen is of great importance. Commonly used screens for general purpose conductor printing on ceramics use stainless steel 325 mesh fabric (325 wires/inch) with a wire diameter of 30 µm. The size of one screen opening is in this case about 50 µm. A general rule is that the minimum line width is about three times the screen wire diameter and the mesh opening should be three times the particle size of the paste. This means that for 50 µm lines, the wire diameter should be 18µm or less.

A line width of below 100 µm is possible by using screens with a thinner mesh wire and thus bigger openings, although this causes a shorter screen life and higher cost. Typically, 400 mesh screens with 18 µm wire are used for feature sizes of less than 100 µm, but even 500 mesh screens are available today. It is clear that the finest fabric materials are susceptible to damage and are also expensive. A higher screen tension gives a better image quality, because a smaller screen gap can be used. On the other hand, the screen is easily damaged if it is stretched to its elastic limit. The optimal angle of screen wires for fine-line printing is generally regarded to be 30 degrees. A wire angle of 22^{o} is also commonly used.

In addition to cloth thickness, the photosensitive screen emulsion thickness has an effect on the print thickness. Typically 10...20 µm emulsion thickness is used for fine line printing, depending on the paste properties. The emulsion exposure parameters should be optimised to get a good line definition and small deviation. For 75µm feature size and smaller, a glass mask is normally recommended for screen exposure. The cost of a glass mask is, however, too expensive for most low and medium volume applications. A film mask does not produce quite as accurate feature edges, but high quality films can be used even for 50 µm feature size.

Regarding fine-line printing, one problem with woven mesh screens is the uneven open area for the paste to go through due to the random location of mesh wires and poor emulsion definition on top of the wire. An even bigger problem is conductor smearing or spreading. This means that a small line spacing is normally a bigger problem than a small line width. Sharp corners are especially problematic with small conductor spaces. The squeezee has to seal the emulsion properly to the substrate surface to prevent the paste from spreading. A very important factor is how the screen is separated from the substrate surface behind the moving squeezee.

Paste composition plays a major role in fine-line screen printing. Typically, fine line thick film pastes are fairly high viscosity gold pastes. One reason for this is that very fine Au powder has been available. Nowadays, Ag powders with a small µm particle size can also be manufactured. The right paste rheology is very important to achieve good results. The viscosity is affected by the binder system, solvent and metal particle size and distribution. It is important to know that the paste properties should match the used printing tool. If the paste works fine with a mesh screen, it doesn't necessarily work well with a stencil and the stencil design should be optimised to the paste viscosity. In production it is also essential to keep the paste viscosity constant. The optimum printer settings and operator skills are, of course, very important for fine-line printing. Most Ag based paste materials for LTCC are not formulated to be suitable for a line width of below 100 µm, although some materials perform better than others.

PRINT TOOLING

The state-of-the-art screen printing tool is the so-called "trampoline screen", also called the "combination screen". This uses a high mesh count, thin wire stainless steel fabric, which is glued to a polymer fabric, as shown in Fig.1. Due to the elastic polymer fabric, the screen tension can be increased without damaging the fine wire screen. The trampoline structure also allows for a more optimal screen separation angle behind the squezee. A microscope picture of a fine mesh combination screen is shown in Fig.2. A glass exposure mask is recommended for feature sizes of below 75 µm. The screen cost is about 50% higher than a conventional fine mesh stainless steel screen.

Metal stencils, made with double sided etching or electroforming, have been used instead of conventional screens in the manufacture of some specific high volume applications, such as solar cells or capacitors. Other applications include wafer bumping and via filling of green ceramic sheets. The potential accuracy of stencil printing is based on the custom hole grid design of the conductor layout. Hole size, hole pitch and stencil thickness can be adjusted to optimise the print quality and print thickness of a certain paste material. To manufacture a high quality stencil, a precise glass mask is needed. This is very expensive since the size of the mask is normally quite big. For experimental purposes and prototyping, a less expensive but also less accurate emulsion glass mask can be used.

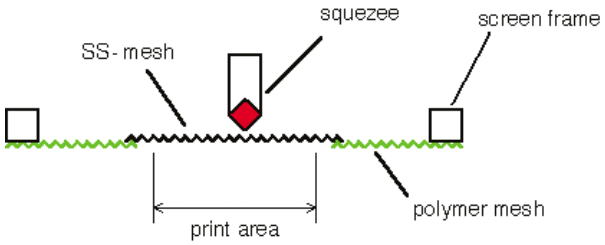

Figure 1. The principle of trampoline screen

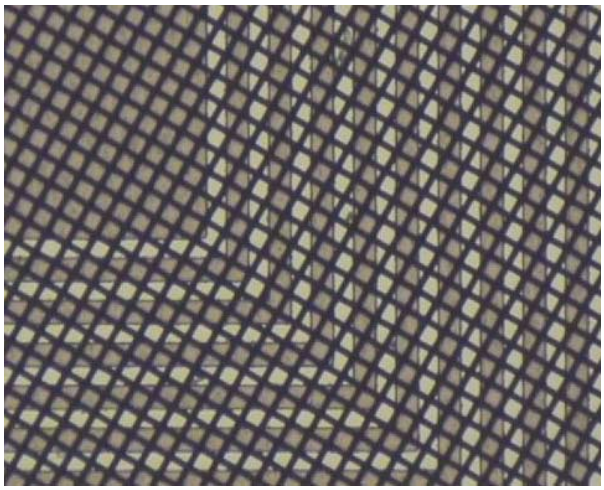

Figure 2. 500 mesh trampoline screen, 18 µm wire, 32 µm opening

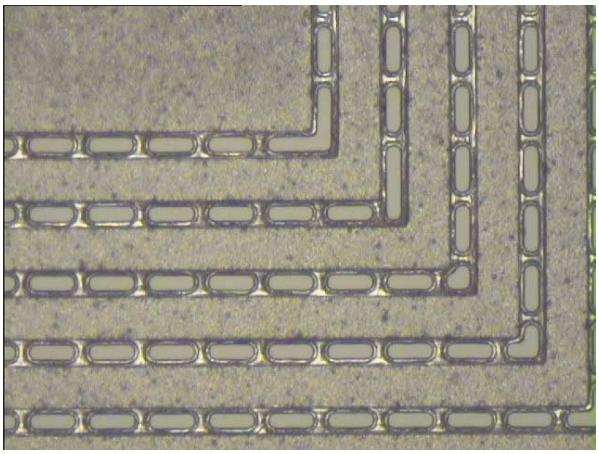

Figure 3. Detail of electroformed stencil, 60µm line/ 90µm spacing

Etched stencils use a metal foil, e.g. stainless steel or brass, etched on both sides to give a symmetric hole. For conductor printing, a polymer emulsion layer is needed on the bottom side of the foil to enable a good line definition. Electroformed metal stencils are usually made of hard nickel with a good mechanical strength and thus a

long screen life. Electroforming gives a better hole quality compared to etching or lasering. The stencil consists of two separate layers. The upper nickel layer with the hole grid pattern is expanded first to a thickness of 20...30 µm. The bottom Ni layer with the conductor image (product layer) has the same function as the polymer emulsion on standard screens. The thickness of the layer can be varied between 10...45 µm to achieve the desired print thickness. The cost of an electroformed stencil is typically 10 to 15 times the cost of a standard mesh screen. On the other hand, the life of the stencil is very long.

EXPERIMENTAL

The experimental fine line printing work was focused on pure Ag pastes, which were printed on tape. These were commercial materials of different LTCC systems. The test layout (4"x4") included typical conductor meander test patterns and spiral inductors with 50 µm minimum line width and space. The fine line printing tests were performed on the Baccini printer. Altogether 31 test lots were made with different Ag pastes. In addition to standard stainless steel screens, a special tool was used, such as trampoline screens, and stencils made by etching or electroforming. The printer parameters like snap off distance, squeezee pressure and squeezee speed were varied and recorded. Also the squeezee hardness and squeezee angle were varied.

Clearly the best results were given by the trampoline type of screens, both 400 mesh and 500 mesh. It seems clear that this concept gives a better print quality compared to conventional stainless steel screens with a similar mesh count and wire diameter. Figure 4 shows the sustainable print quality achievable with the tested combination screens and fine-line pastes. Even 50 µm lines and spaces were possible for straight lines. The spiral test structure with 50 µm line width and space couldn't be printed repeatedly, although in some individual cases the result was good.

The print quality for the etched stencil was similar or slightly better than that of a standard 400 mesh screen. The benefit, compared to the high cost, was not big. The electroformed stencil gave better results than the etched one but conductor smearing was a problem with dense spiral structures. In stencil printing in general, high viscosity pastes cause line discontinuities due to limitations in the hole pitch of the grid layer. The stencil grid design is thus very critical. Electroformed or etched stencils cannot generally be recommended for fine-line printing in circuit and module manufacture. For very high volume

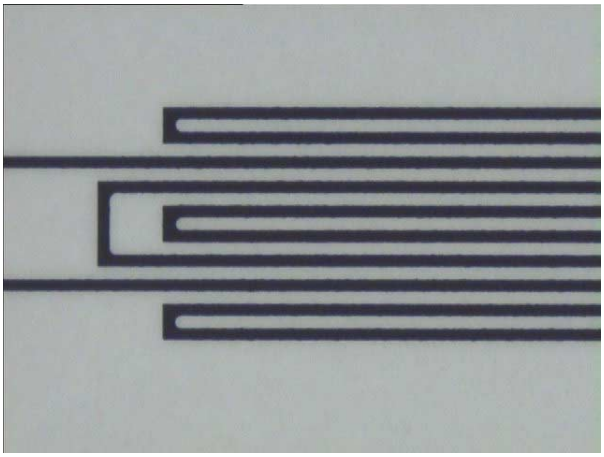

Figure 4. Ag conductor 75 µm line/ 75 µm space, printed with 400 mesh "trampoline screen"

applications, however, the optimisation of stencil design could be justified and stencil tooling may be a good and cost effective solution in component manufacture.

CONCLUSIONS

It was demonstrated that the new trampoline type of screen gives a clear improvement in fine-line print quality compared to conventional stainless steel screens. Electroformed metal stencils also gave promising results and are potentially suitable for the high volume manufacture of special applications and components. A clear problem with fine-line printing on LTCC is that there are only a few silver based thick film pastes capable of producing a line width of below 100 µm.

Kari Kautio
Kari Kautio@vtt.fi

The Characterisation of the Integrated RF Passive Components in LTCC

LTCC-Technology enables the integration of passive components into the substrate of an electronic device. It can be used for cost reduction by replacing discrete components. A great number of spiral inductors and interdigital capacitors of different geometries were manufactured and measured to find the useful frequency span and the optimal dimensions. The tests were repeated using different commercially available LTCC material systems. The measured peak Q-values for the spiral inductors were up to 100. The lowest measured insertion loss for the three finger interdigital capacitor was 0.4 dB at 7.7 GHz, which was the series resonance frequency of the capacitor.

STRUCTURES FOR INTEGRATED INDUCTANCE REALISATION

The spiral inductor is the most used inductive element in the planar world. It has good area efficiency because of the mutual coupling of the turns. That also enhances the inductor quality factor (Q-value). The restrictive property of spirals is that the parallel resonance frequency remains quite low due to the relatively high parasitic capacitances of the spiral turns.

The ground plane underneath the spiral has a very important role for the inductor Q-value. The characteristic impedance of the spiral trace should be made as high as possible to create an inductor rather than a transmission line structure. This means that a spiral trace without the ground plane acts mostly like an inductor. If the dimensions of the spiral are made small (a narrow conductor trace is used) and there is also dielectric material present, the radiation of the spiral is reduced and furthermore the Q-value is increased. The picture of the structure for spiral inductor testing is presented in fig. 1.

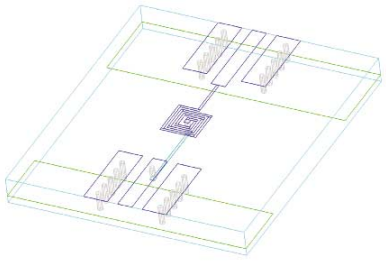

Fig. 1. Test structure for spiral inductor measurement.

To characterise the properties of spiral inductors, sets of test structures with variable dimensions were manufactured on a few commercially available LTCC material systems (DuPont 951, Heraeus CT2000 and Ferro A6S). Round geometries were also designed and tested, because round is known to be the optimal spiral inductor shape. The improvement in Q was even up to 45% compared to rectangular geometries.

At the resonance frequency the parallel resonance of the spiral causes a deep notch on the measured S21 curve. An example of the measured response of the spiral inductor is presented in fig. 2. As can be seen, the notch that indicates a high Q-value is very deep. The Q at resonance can be calculated directly from the 3-dB bandwidth of the notch. Moreover it can be approximated to be the unloaded Q because the notches are in the range of -40 to -50 dB which means very low loading [1]. The parameters of some tested rectangular inductors are presented in table 1.

From table 1 it can be seen that inductors 1 - 4, made by using photopatterned conductor metallization, receive a clear benefit from the narrow available conductor trace

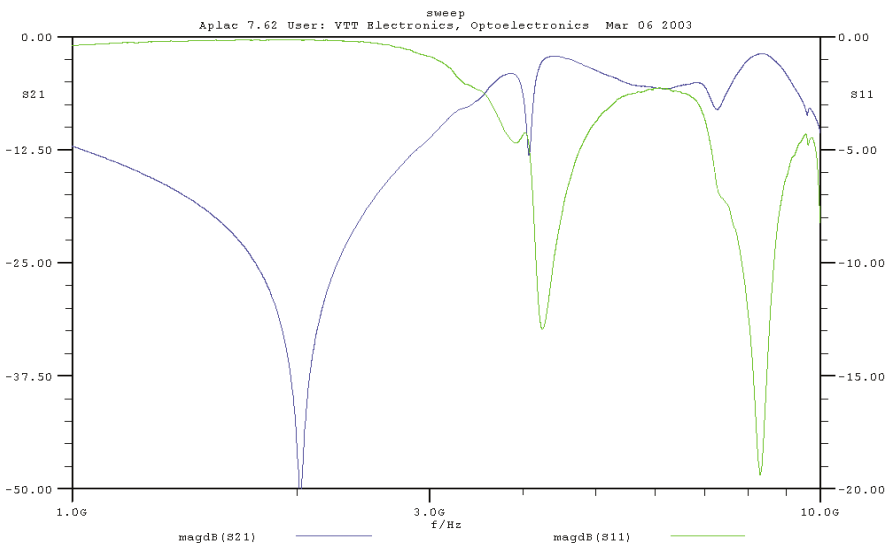

Fig. 2. Measured response of the example spiral inductor (nr. 2 in table 1).

Table 1. The parameters of some measured rectangular spiral inductor structures.

Structure number /LTCC Type	Conductor trace width (W)	Outer side (Do)	Inner side (Di)	Number of turns (N)	Inductance measured at 200 MHz (L)	Quality factor at resonance (Q)	Resonance frequency (f_res)
1. / DP951	50 um	1.2 mm	0.5 mm	4	25 nH	19.8	3.34 GHz
2. / DP951	50 um	1.6 mm	0.5 mm	6	57 nH	74.8	2.02 GHz
3. / DP951	50 um	2.8 mm	1.1 mm	9	481 nH	78.7	795 MHz
4. / DP951	50 um	3.2 mm	1.3 mm	10	1.59 uH	81.9	645 MHz
5. /CT2000	100 um	1.5 mm	0.5 mm	3	17 nH	30.5	4.15 GHz
6. /CT2000	100 um	3.1 mm	0.5 mm	7	115 nH	70.9	1.28 GHz
7. /CT2000	100 um	2.4 mm	1.0 mm	4	48 nH	86.1	1.90 GHz
8. /CT2000	100 um	2.8 mm	1.0 mm	5	77 nH	85.9	1.46 GHz
9. / A6S	100 um	1.5 mm	0.5 mm	3	16 nH	43.2	4.84 GHz
10. / A6S	100 um	3.1 mm	0.5 mm	7	87 nH	94.9	1.52 GHz
11. / A6S	100 um	2.4 mm	1.0 mm	4	42 nH	75.4	2.19 GHz
12. / A6S	100 um	2.8 mm	1.0 mm	5	64 nH	62.4	1.69 GHz

(50 um) to realise higher inductances on the same substrate area. The maximum achieved inductance was as high as 1.6 uH. Inductors 5 - 12 have printed 100 um wide conductor traces, and the achieved inductances are less than 100 nH. The Q-values for all the inductors are between 20 and 95.

STRUCTURES FOR INTEGRATED CAPACITANCE REALISATION

Capacitive circuit elements can be realised, for example, with multilayer plate structures. Unfortunately they have a relatively high parasitic capacitance to the grounded shieldings. Plate capacitors are not useful in microwave applications, where interdigital capacitors are a better choice. A picture of a three finger interdigital capacitor is presented in fig. 3.

The plot of the measured response of the example three-finger interdigital capacitor (number 13 in table 2) is presented in fig. 4. The effect of the series and parallel mode resonances can be noticed occurring while the overlapping section of the fingers are electrically $\lambda/4$ and $\lambda/2$ long respectively. The maximum of the |S21| occurs at series resonance frequency and the minimum or the notch occurs at the parallel mode resonance frequency. Parameters of some tested finger capacitors are presented in table 2.

A plate capacitor topology can be used to realise buried and shielded capacitors. Plate capacitors usually have significant parasitic capacitance to grounded shield metallization. To minimise the parasitic capacitance the substrate can be stacked with tapes having different thicknesses so that the thinnest tapes are in the middle of the

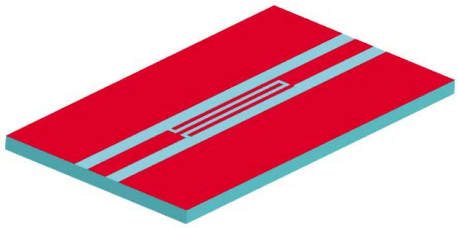

Fig. 3. Three-finger interdigital capacitor.

stack acting as the dielectric between the capacitor plates. Mixed-K laminates would also be very beneficial for the integration of plate capacitors. A picture of an example plate capacitor structure is presented in fig. 5. Parameters of some tested plate capacitors are presented in table 3. The plot of the measured response of the example plate capacitor is presented in fig. 6 (number 5 in table 3).

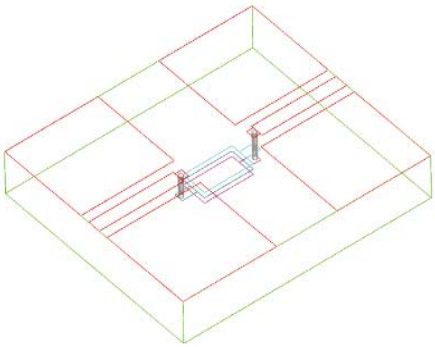

Fig. 5. Plate capacitor structure.

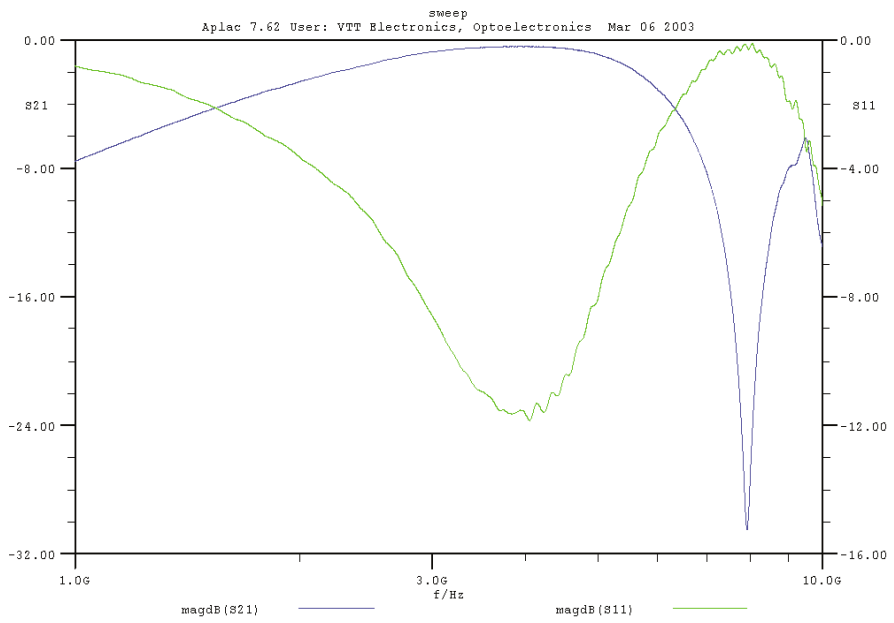

Fig. 4. Measured response of the example three-finger interdigital capacitor (nr.13).

Table 2. Parameters of some measured interdigital capacitors.

Structure number /LTCC Type	Length of the finger section	Number of fingers	Width of finger traces and gaps	Resonance frequency	Insertion loss at the resonance frequency
1. / DP951	4 mm	3	130 um	7.5 GHz	-1.0 dB
2. / DP951	5 mm	3	130 um	7.3 GHz	-0.5 dB
3. / DP951	6 mm	3	130 um	5.7 GHz	-0.6 dB
4. / DP951	7 mm	3	130 um	4.9 GHz	-0.6 dB
5. / DP951	8 mm	3	130 um	4.5 GHz	-0.6 dB
9. / CT2000	4 mm	3	100 um	7.7 GHz	-0.4 dB
10. / CT2000	5 mm	3	100 um	6.1 GHz	-0.4 dB
11. / CT2000	6 mm	3	100 um	5.2 GHz	-0.4 dB
12. / CT2000	7 mm	3	100 um	4.7 GHz	-0.4 dB
13. / CT2000	8 mm	3	100 um	3.9 GHz	-0.4 dB
14. / CT2000	9 mm	3	100 um	3.4 GHz	-0.4 dB
15. / A6S	4 mm	3	100 um	5.1 GHz	-3.0 dB
16. / A6S	5 mm	3	100 um	5.1 GHz	-1.6 dB
17. / A6S	6 mm	3	100 um	5.1 GHz	-1.0 dB
18. / A6S	7 mm	3	100 um	4.5 GHz	-0.9 dB
19. / A6S	8 mm	3	100 um	4.4 GHz	-0.5 dB
20. / A6S	9 mm	3	100 um	3.7 GHz	-0.5 dB
21. / DP943	4 mm	3	100 um	7.8 GHz	-1.1 dB
22. / DP943	5 mm	3	100 um	6.8 GHz	-1.0 dB
23. / DP943	6 mm	3	100 um	5.0 GHz	-0.8 dB
24. / DP943	7 mm	3	100 um	4.5 GHz	-0.7 dB

Table 3. Parameters of some measured plate capacitors.

Structure number /LTCC Type	Dimensions of the plate stack	Series capacitance	Parasitic capacitance	Measured min. insertion loss / frequency	Dielectric thickness between plates / substrate thickness
1. / DP951	1.2 mm x 2.25 mm	1.9 pF	1.4 pF	2.0 dB / 3 GHz	0.2 / 1.6 mm
2. / DP951	1.2 mm x 3.1 mm	2.7 pF	1.6 pF	1.8 dB / 1 GHz	0.2 / 1.6 mm
3. / CT2000	1.2 mm x 2.25 mm	6.5 pF	1.7 pF	1 dB / 1.0 GHz	0.078 / 1.1 mm
4. / CT2000	1.2 mm x 3.1 mm	8.7 pF	2.1 pF	1 dB / 0.7 GHz	0.078 / 1.1 mm
5. / A6S	1.2 mm x 2.25 mm	3.3 pF	1.0 pF	0.35 dB / 2.5GHz	0.1 / 1.6 mm
6. / A6S	1.2 mm x 3.1 mm	4.6 pF	1.3 pF	0.38 dB / 1.9GHz	0.1 / 1.6 mm
7. / DP943	1.2 mm x 3.65 mm	5.8 pF	1.5 pF	0.87dB / 1.2GHz	0.11 / 1.3 mm
8. / DP943	1.2 mm x 4.8 mm	7.6 pF	1.7 pF	0.90 dB / 0.9GHz	0.11 / 1.3 mm

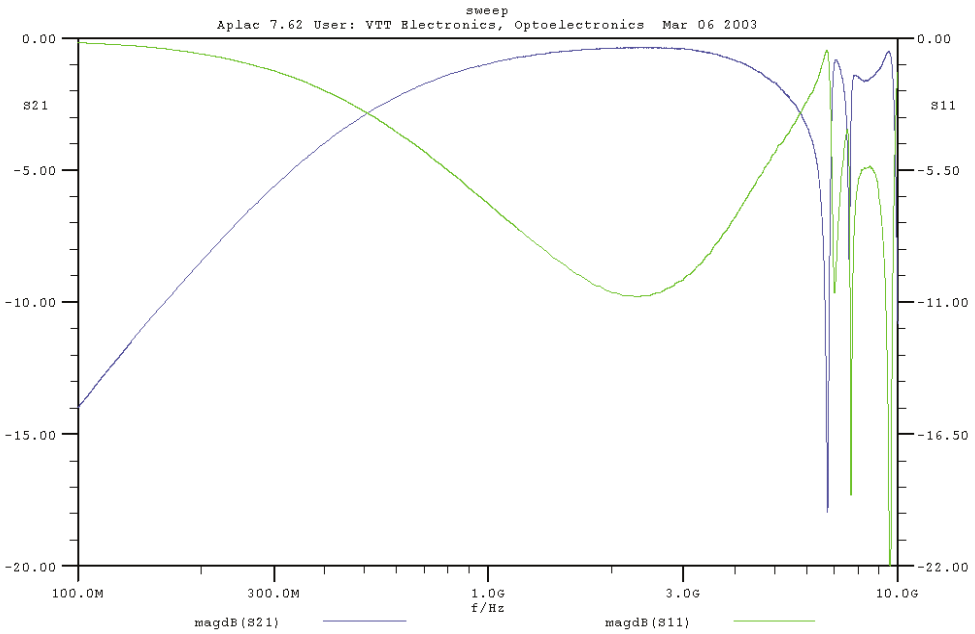

Fig. 6. Measured response of the example plate capacitor (nr.5).

REFERENCES

[1] Carroll J., Li M. & Chang K. (1995) New Technique to Measure Transmission Line Attenuation. IEEE Transactions on Microwave Theory And Techniques, January 1995.

Antti Vimpari
Antti.Vimpari@vtt.fi

LTCC Dual Mode Patch Filter for Millimeter Waves

1. INTRODUCTION

Low temperature co-fired ceramic (LTCC) technology is based on multi-layer thick film processing, which allows the combination of active and passive microwave components into a monolithic module. This enables microwave devices to be fabricated with a high overall reliability while keeping the cost competitively low. The development of local area networks (LAN) and car radar systems caused the intensive investigation of LTCC properties at millimetre-waves. The experiments of different transmission lines (microstrip, stripline, coplanar, etc.) and passive components based on LTCC at frequencies up to 40 GHz have been made. They show the capability of multi-layer LTCC technology to be utilised at millimetre-waves [1,2].

Fabrication tolerances of LTCC technology (currently it is possible to resolve 100/100 µm line/space with 10% accuracy) can affect the repeatability of LTCC filter parameters. In addition, LTCC filters exhibit a rather high insertion loss in bandpass, which is caused by the microwave loss of normal conductors due to the skin effect. Extra attention has to be spent on selecting the correct structure to find a resonator with the highest Q-factor. Also it is necessary to select the right type of filter characteristic to minimise the number of resonators.

The aim of the experimental investigations was to find a low-loss filter layout possessing the least sensitivity to technology uncertainty and to test the parameter repeatability of the bandpass LTCC filter proposed.

2. DESIGN

Fig. 1 shows the conventional dual-mode resonant structure. Such a structure has been developed from a single-mode resonator (commonly used for microstrip patch antennas) by adding a perturbation at a point 45° from the axes of the coupling and the resonator (the patch is cut in one of its corners). It enables two orthogonal modes, generated within the resonator, to be coupled [3]. The filters based on such a structure are supposed to possess the least sensitivity to LTCC technology uncertainty. Each square patch replaces two commonly used half-wavelength resonators, the side of the square patch being about half-wavelength. There are therefore no narrow lines with widths close to technology limitations. Also these resonators are known to have advantageous features such as size compactness, low radiation loss, and an easy-to-design layout.

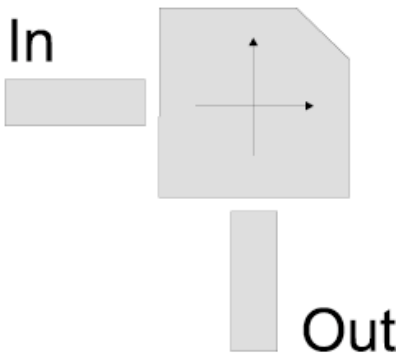

Figure 1. The principle of dual-mode resonant patch structure.

The aim of the design procedure was to build the filter with a 3.5% bandwidth and 12 dB return coefficient. To obtain the required strength of coupling coefficient the resonant structure and feed lines were inserted into different layers. So, the external coupling is realised by an overlap between the resonator and the feed line. By changing the deepness of the cut the coupling coefficient between the generated modes can be modified. It makes it possible to design a second order filter.

A filter operated at millimetre-waves should be inserted into a proper package to prevent radiation losses. The stripline configuration is the most preferable solution. It enables us to design a closed box where vertical walls are realised by vias. The distance between vias was about 200 µm, 12 times less than the wavelength at the central frequency of the bandpass. Hence, the package walls may be considered monolithic.

There are many different types of filter responses available. Every type has its own advantages and disadvantages. The necessary design trade-offs can be evaluated to best meet filter requirements. The use of Chebyshev polynomial response allows a minimal insertion loss with the sharpest cut-off to be obtained. Estimation of the filter parameters shows that a 3-pole filter with Chebyshev characteristics satisfies the specifications involved.

3. REALISATION

To test LTCC properties at millimetre-waves the 2-pole filter with a central frequency of 29.1 GHz and 2.1 % bandpass was designed for an 8-layer CT2000 tape system. The length of the patch side was 1.5 mm and the widths of the input and output lines were 100 µm. The distance between the square patch and the feed lines was 156 µm and the feed lines overlapped the square patch by 500 µm. The ground layers of 6x6 mm^2 were printed on

the top and bottom of the substrate. Their distance to the patch layer was 312 µm. The Ag conductors were screen-printed on an unfired tape. All the layers were then laminated and co-fired.

4. RESULTS

The scattering parameters of the filter have been simulated by Ansoft Ensemble 8.0 and measured by a network analyser from 4 to 45 GHz. The experimental and simulated characteristics of the filter are shown in Fig. 2. The return loss over the bandwidth is better than 12 dB. The structure reveals less than 2.8 dB loss in the bandpass. The measured and predicted results coincide rather well in the bandpass. However, additional resonances were observed in the measured frequency band. We suppose they were caused by the filter package and this influence on filter characteristics can be removed by changing the excitation of the filter. The measurements of the test structures reveal the filter's good parameter repeatability. The Q-factor of the dual mode structure involved was 150. For comparison, a microstrip ring resonator and a stripline half-wavelength resonator were designed. They had Q values of 100 and 115, respectively. Thus the dual mode resonant structure is a very attractive option.

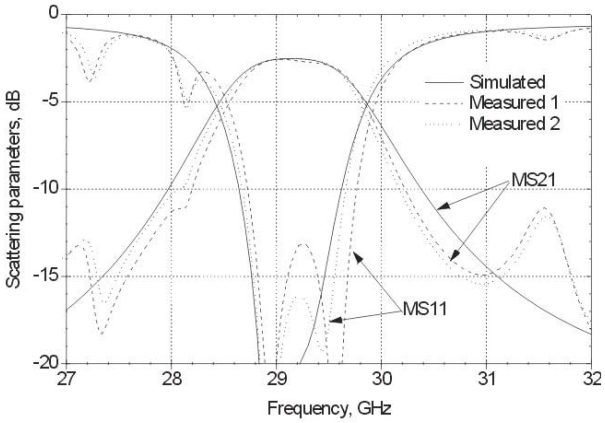

Figure 2. The scattering parameters of the 2-pole LTCC filter.

5. CONCLUSIONS

The LTCC dual mode bandpass filter was designed and measured. Comparison of the predicted results and measured data shows good agreement. Also, the repeatability of the scattering parameters of the LTCC filter was demonstrated. The design of the filter package was found to be critical for the performance of the filter.

REFERENCES

1. C. Free and P. Barnwell, "Microwave properties of an integrated thick film and tape technology to 40 GHz", Proc. Int. Symp. on Microelectronics, Chicago IL, USA, pp. 84-88, October 1999.
2. W. Simon, R. Kulke, A. Wien, M. Rittweger, I. Wolff, A. Girard and J.-P. Bertinet, "Interconnects and transitions in multilayer LTCC multichip modules for 24 GHz ISM-band applications", IEEE MTT-S Dig., Boston, USA, pp. 1047-1050, June 2000.
3. J.A. Curtis and S.J. Fiedziuszko, "Miniature dual mode microstrip filters", IEEE MTT-S Dig., Boston, USA, pp. 443-446, June 1991.

Vasily Kondratyev
Vasily.Kondratyev@vtt.fi

Markku Lahti
Markku.Lahti@vtt.fi

Tuomo Jaakola
Tuomo.Jaakola@vtt.fi

Thermal Management of Power MMIC on LTCC Substrate

INTRODUCTION

Low temperature co-fired ceramics (LTCC) are finding increased usage as an interconnect substrate, especially in high frequency applications due to the high conductivity of the conductors and low loss of the dielectric. Millimeter wave transmitter modules often require the integration of a high power MMIC amplifier on the substrates. The power densities to be dissipated can be as high as 100 W/cm^2, so a very good thermal contact with the thermal sink is required. Due to the relatively low thermal conductivities of 2-4 W/m°C of LTCC materials, high power applications must use thermal vias.

In this work the heat management effectiveness of Si and GaAs components on LTCC substrate has been modeled by a thermal simulation tool, and the results have been compared to experimental measurements. The effects of thermal via area fraction, and of novel die adhesive materials with high thermal conductivities on the thermal management capability of the structures have been studied.

MANUFACTURE OF TEST CIRCUITS

Figure 1 shows a sketch of the test structures selected for studying the thermal transfer efficiency of thermal vias. The largest area fraction of vias was obtained with the via diameter of 180 µm and via pitch of 350 µm. The best thermal conductors are the silver via fills (i.e. DuPont 6141 at 289 W/mK).

A silicon thermal test die (PST1-02, size 2.54 x 2.54 x 0.6 mm^3) with a heating resistor and diodes on its surface for temperature monitoring and a GaAs power amplifier (42 GHz HPA APH403 from Velocium) chip (size 1.3 x 2.76 x 0.1 mm^3) were used in the work. The typical DC power dissipation of the component is 2.4 W.

Novel materials with high thermal conductivity were used for attaching the power components. ME8418-XT and ME8550-UT from AIT, XCP3300 from Emerson&Cuming, Ablebond 84-1LMIT1 and Diemat DM6030 were used in the experiments.

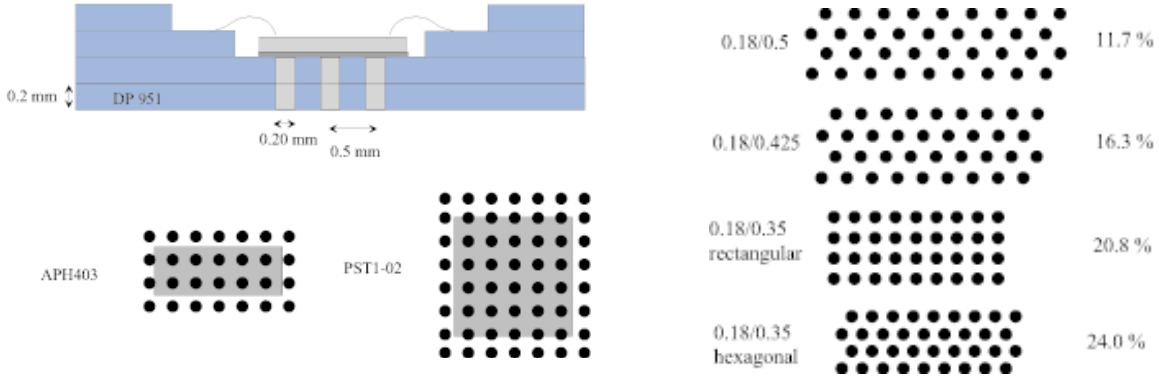

Figure 1. Cross-section of the LTCC thermal test circuit (left). Via patterns selected in making the thermal management LTCC substrates (right).

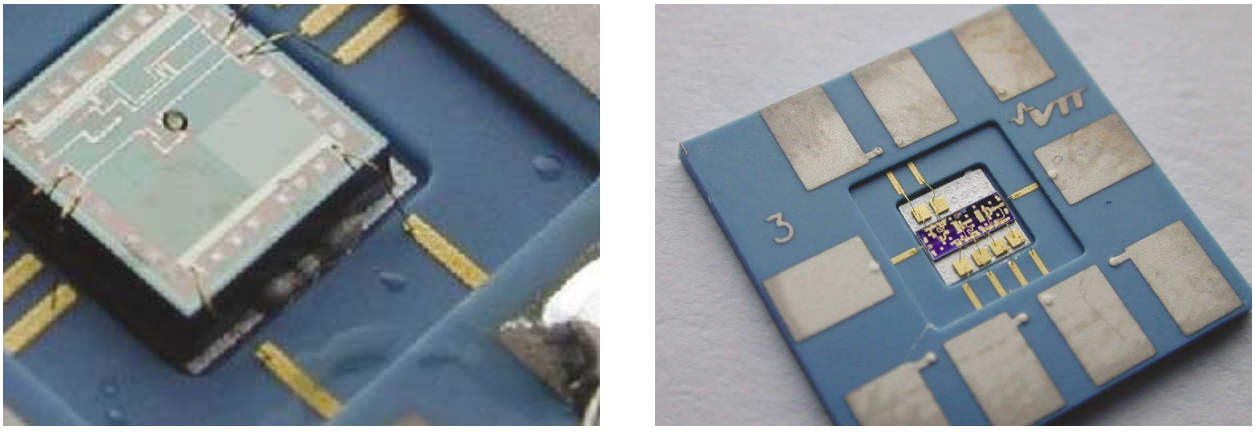

Figure 2. Photo of the PST test component attached on LTCC (left) and a photo of the assembled APH403 MMIC with six capacitors.

Table 1. Maximum temperature increase on an APH403 GaAs power amplifier chip on LTCC calculated by THERMIC simulation tool.

Power distribution on chip surface	Area fraction of vias	ΔT
2.4 W in 70% of chip area	18.4 %	23.0°C
2.4 W in 70% of chip area	32 %	21.1°C
2.4 W in three 0.5 mm wide areas (0.26, 0.86 and 1.34 W)	18.4 %	39.0°C
2.4 W in three 0.5 mm wide areas (0.26, 0.86 and 1.34 W)	32 %	36.4°C

The LTCC substrates were manufactured at VTT Electronics LTCC proto line using DuPont 951-AX tape material. The number of tape layers was four. Figure 2 shows a close-up view of the LTCC test circuits with the components assembled into the cavities.

SIMULATIONS

The power handling capacity of different structures was modeled by a thermal simulation tool THERMIC. In addition, modeling work by a more sophisticated tool, IDEAS, was performed.

The results for APH403 MMIC are shown in Table 1 for two power distributions and two thermal via area fractions. An example of the temperature distribution is shown in Figure 3.

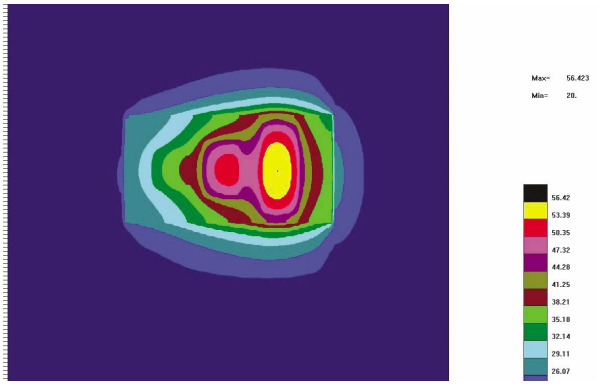

Figure 3. Temperature distribution on the surface layer of APH403 (power shared between three areas).

For the PST chip a power of 5 W was assumed to be evenly distributed over 70% of the area of the chip surface. Figure 4 shows as an example of the simulation result for approximate temperature differences over the layers of the structure.

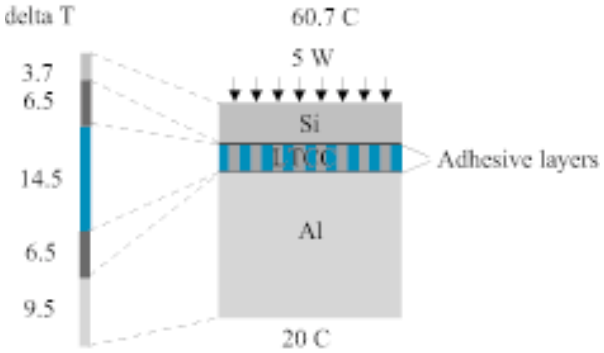

Figure 4. Temperature differences over the layers of the PST structure.

MEASUREMENTS

The temperature rise of the PST chip was measured for samples attached onto a thick aluminium heat sink by using a thin layer of silicone thermal grease. Figure 5 shows the measured temperature for samples made using ME8418-XT adhesive as a function of area fraction of vias, and two simulated curves with different thermal conductivities for adhesive and vias.

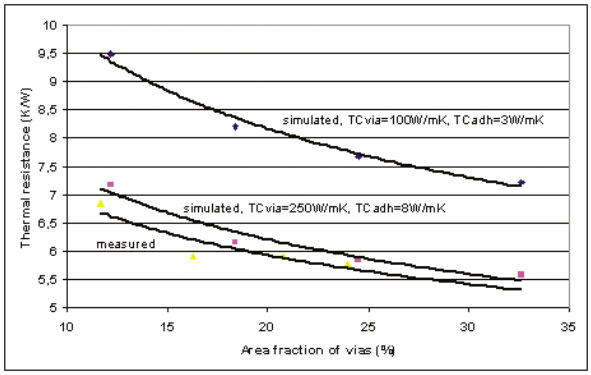

Figure 5. Measured and simulated maximum temperature for different area fractions of thermal vias.

The planarity of the bonding surface of LTCC is important for good thermal contact to the chip and heat sink surfaces. Figure 6 shows the measured roughness of the thermal

via area of LTCC substrate. One can notice that the vias protrude some 6...8 µm from the background silver layer. This could, in fact, be beneficial for good heat transfer, because most of heat is transferred through the vias, and protruding vias could make a closer contact with the chip and sink surfaces.

The structure of the adhesive layers was studied by scanning electron (SEM) and acoustic (SAM) and x-ray transmission microscopes. The thickness of the adhesive layer was 15...20 µm. With SAM thin surface cracks could be detected, while x-ray only showed larger deviations from the homogeneous adhesive layer.

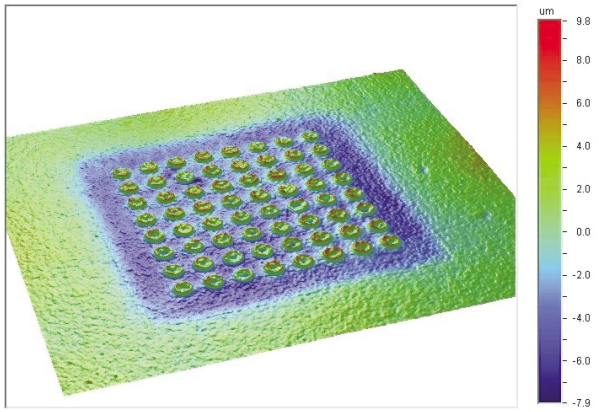

Figure 6. Planarity of thermal via area.

CONCLUSIONS

The maximum simulated temperature rise for the MMIC chip at 2.5 W power dissipation was between 28...39°C depending on the adhesive thickness and thermal conductivity, and thermal via conductivity and area fraction. However, one must remember that this is not the actual transistor channel temperature rise, which is still considerably higher. The corresponding values for the PST chip were 30...40°C at 5 W power dissipation. The measured values conformed quite well to the simulated maximum temperatures. It was observed that the vias protrude some 6...8 µm from the background silver layer. The thickness of the adhesive layer was measured to be 15...20 µm.

REFERENCES

1. T. Jaakola, K. Kautio, J. Petäjä, and J. Lenkkeri, *Thermal Management of Power MMIC on LTCC Substrate*, paper accepted for presentation at 14th European Conference EMPC, June 2003.
2. M. Zampino, R. Kandukuri, W. Kinzy Jones, *High Performance Thermal Vias in LTCC Substrates*, ITherm 2002, the International Conference on Thermal, Mechanics and Thermomechanical Phenomena in Electronic Systems, June 2002 in San Diego, California.

Tuomo Jaakola
Tuomo.Jaakola@vtt.fi

Kari Kautio
Kari.Kautio@vtt.fi

Jarno Petäjä
Jarno.Petaja@vtt.fi

Jaakko Lenkkeri
Jaakko.Lenkkeri@vtt.fi

Lead-free Soldering

INTRODUCTION

The forthcoming RoHS directive (a directive on the limitation of hazardous substances in electrical and electronic equipment) bans lead from new electrical and electronic equipment put on the market by Member States of the EU. The latest expected date for RoHS to come into operation is 1 July 2006 across the whole of the EU with some exceptions. The electronic industry is now preparing for lead elimination by researching and testing new lead-free solders and lead-free components.

AIMS OF THE STUDY

The purpose of this project was to get hands-on experience of lead-free wave and reflow soldering. Reliability tasks for lead-free soldered boards were also investigated with several tests. Results were compared with tin-lead soldered boards.

TEST ARRANGEMENTS

One lead-free solder paste and one lead-free wave solder alloy were used for soldering test boards. The solder alloy selected was Sn3.8Ag0.7Cu. Wave solder fluxes with a higher solids content than comparable fluxes in SnPb soldering were used for lead-free soldering, according to the recommendations of manufacturers. Double-sided FR-4 and single-sided CEM-1 with either Ni/Au or OSP (organic solderable preservative) surface finishes were used as laminates. SMD and through-hole components with lead-free external terminal plating were used for lead-free soldering. To provide a comparison tin-lead component boards were also soldered.

The reflow and wave soldering processes were optimised according to the common recommendations of the manufacturer. The peak temperature during reflow soldering was 240-250°C, and the measured maximum temperature during wave soldering 257-259°C. The time over melting point (217°C) of the lead-free reflow solder was longer than for common SnPb solder for proper wetting of the joints. No additional nitrogen was used during soldering.

SOLDERABILITY AND SHEAR STRENGTH

A solder joint of SnAgCu has a more greyish and matte appearance when compared to a SnPb solder joint. Also the geometry of the solder joint differs somewhat from SnPb due to the lower wetting ability.

Soldering results showed that in some cases the solderability of lead-free terminated components was not as good as that of tin-lead terminated components. The wetting of some reflow soldered tin terminated chip resistors was incomplete as can be seen in Figure 1.

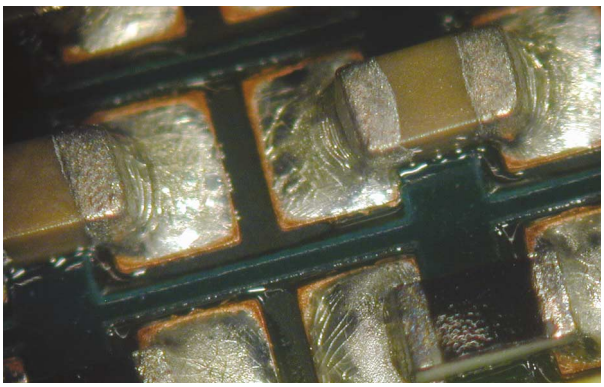

Figure 1. Solder joints after reflow soldering.

Large differences in the wave solderability of chip components, as lead-free or lead containing, could not be detected. Solder bridging between some wave soldered surface mount components was larger with lead-free SMD components than with lead containing components. In general, the adequate wetting of joint areas on the wave side of the board can be achieved with proper process optimisation and flux selection.

Some voids were detected in the reflow soldered and wave soldered through-hole joints.

Shear strength measurements were performed before and after temperature cycling (-40°C to +125°C for 1000 hours). Variations in the shear strengths of chip resistors and capacitors were quite large after soldering and could not be specified as lead-free material characteristics. On the whole, the joint strengths of lead-free chip components were at the same level as tin-lead joints and were thus satisfactory. The variations in joint strengths became equalised in some series after temperature cycling. Different termination plating materials of chip resistors and capacitors (100% tin and Cu/Ag/Ni, respectively) did not clearly affect the shear strengths of the components. An example of shear strengths is shown in Figure 2.

RELIABILITY TESTING

The following reliability tests were performed:

- Temperature cycling (-40°C to +125°C for 1000 hours)
- Fatigue life measurement of BGA components (bending test)
- Accelerated life test (85°C 85%RH for 500 hours, 15 volts bias)

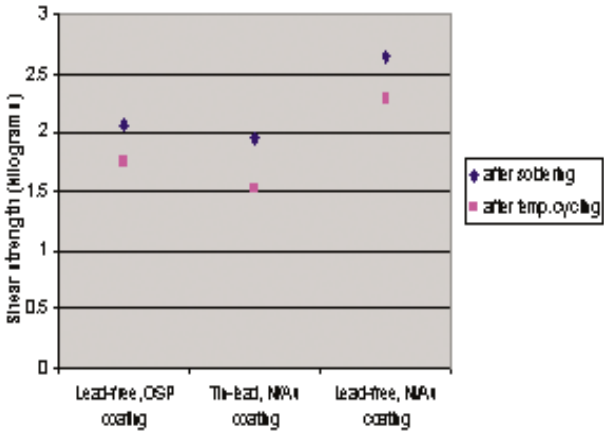

Figure 2. Shear strengths of reflow soldered 0402 capacitors.

In addition, shear test measurements were performed before and after temperature cycling as mentioned in the previous section. The joint integrity of BGA daisy chains during temperature cycling was controlled with resistance measurements. The joint integrity of PIH (pin-in-paste) connectors was controlled from the cross-sections after the temperature cycling test.

As a general conclusion, lead-free and lead-containing component boards behaved similarly during reliability tests. Temperature cycling was found to be the major accelerating factor in joint degradation.

Temperature cycling caused joint unfastening and joint cracking in some lead-free through-hole connector joints as shown in Figure 3.

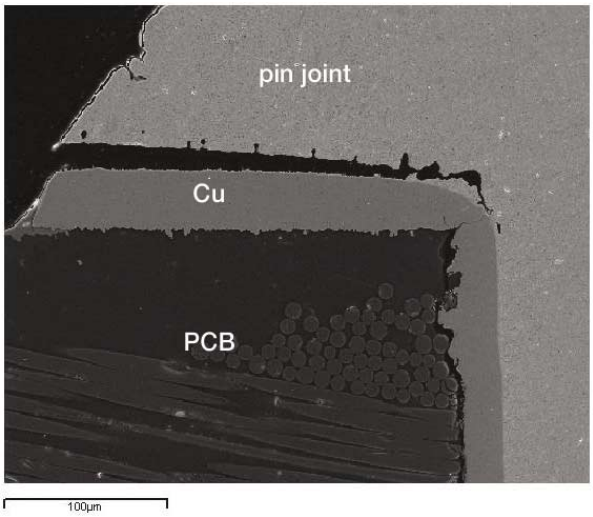

Figure 3. Fillet lifting from the pad after temperature cycling, the sample is a wave soldered through-hole connector.

The results of the bending of BGA components can be considered as preliminary. Any dramatic differences between lead-free and tin-lead BGA components in their resistance to cyclic bending could not be observed. Cross-section samples showed that BGA balls were typically cracked on the component joint as shown in Figure 4.

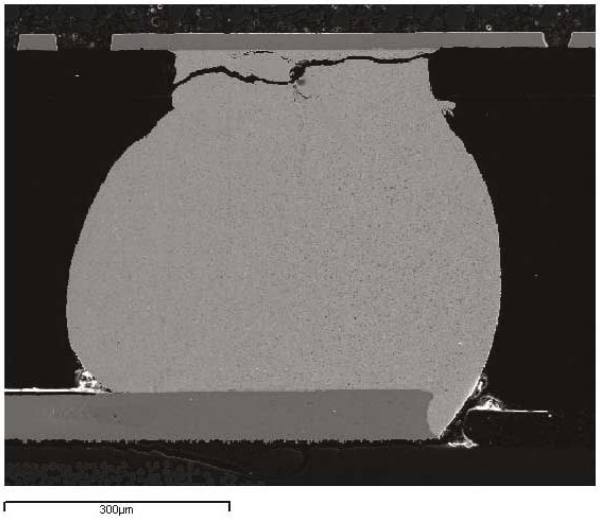

Figure 4. Cracking of the component was seen from the cross-section on the component side.

CONCLUSIONS

Both reflow and wave soldering is possible with lead-free materials without any major obstacles.

The quality of reflow and wave soldering was satisfactory. Fillet formation was acceptable for all components, only reflow soldered chip components wetted incompletely, but they still passed the limit of IPC-A-610C. PTH filling and PIH-connector hole filling was comparable to that of holes in SnPb boards.

The different tested component termination plating materials had no clearly different impact on the soldered joints. It is always advisable to check the temperature durability of component packaging plastics before soldering. In this test the pin header did not stand reflow soldering.

Both OSP and Ni/Au surface finishes performed equally well in lead-free and SnPb soldering.

The performance of lead-free component boards in accelerated reliability testing did not deviate considerable from that of common SnPb soldered boards. The only noticeable thing was fillet lifting after temperature cycling. According to this examination it cannot be sug-

gested that fillet lifting would be a phenomenon of lead-free soldering.

The next important step in lead-free soldering should involve product level implementation, going through reflow and wave soldering process optimisation, observation of equipment demands and the selection of suitable materials. Solder defects will also lessen by, for example, proper flux selection. The best component termination materials for lead-free soldering need to be evaluated. Several lead-free solders and pastes must be set in an order of superiority according to their metallurgy. The production yield and through it the cost effect of moving to lead-free production must be estimated. Common knowledge of the failure rate of lead-free products must also be defined.

REFERENCES

KOTEL004 Lead-free Soldering, Final Report, in press.

NoNE lead-free soldering guideline, in press.

Liisa Kivimäki
Liisa.Kivimaki@vtt.fi

Full-Sheet Paper Moisture Measurement Using Infrared Spectroscopy

Traditional paper moisture measurements are based on scanning measurement units located in the dry end of the paper machine, and attempts to use these scanners in the wet end have failed so far. Scanners also suffer from the inability to separate cross direction (CD) and machine direction (MD) variations from one another. VTT Electronics, Metso Automation and Suomen Optomekaniikka have developed a new moisture measurement system, capable of full-sheet measurement in the wet end, and Metso Automation launched this new powerful quality measurement, IQInsight, in June 2002. The first unit was installed about a year ago on PM8 at UPM-Kymmene's Kymi Paper mill in Kuusankoski, Finland and it has operated uninterrupted ever since.

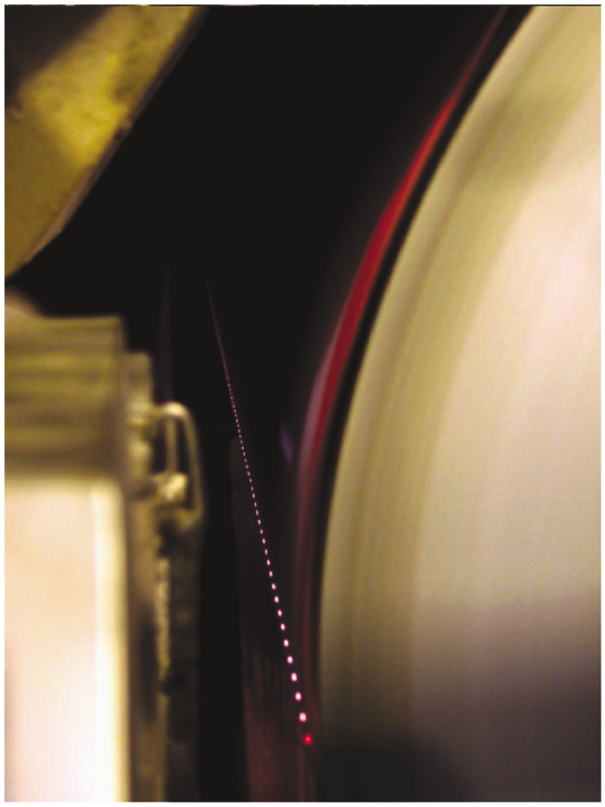

The measurement is based on infrared spectroscopy of the moving paper using multiple measurement modules across the web and data transfer using optical fibres. This technique makes IQInsight capable of capturing high resolution moisture profiles with high frequency. (Figure 1)

TRUE CD AND MD SEPARATION AT A HIGH SPEED

Before IQInsight, online quality measurements scanned across the moving paper web. Therefore several hundred meters of paper passed by during one scan and MD variations were mixed up with CD profile. MD variations, folded into CD profile, made the measurement even slower since a stable CD profile was achieved only with profile filtering. If one scan across the sheet took more than 30 seconds, the filtering reduced the measurement speed to several minutes.

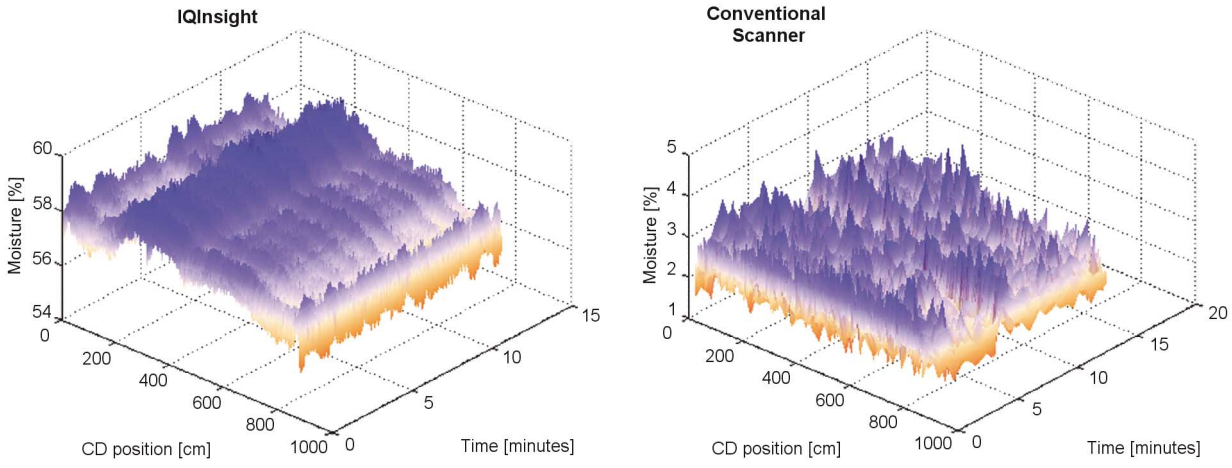

Figure 2. The same MD variation measured with a traditional scanner in the dry end and IQInsight in the wet end. Without IQInsight this MD variation could lead to replacement of the scanner, since the scanning measurement seems to be unstable and the problem itself would not be found.

The ability to separate MD and CD variation makes the IQInsight measurement unique. This feature relies on the high measurement speed and is achieved with multiple detector modules. With this technique the system reaches 1 cm resolution and, if ultimate speed is required, provides profiles in less than 200 ms. Even at this speed one raw moisture profile is so stable that no filtering is required.

Because of the high moisture measurement accuracy, high CD resolution and high measurement speed, it is possible to display series of profiles in three-dimensional displays. These displays reveal true MD and CD variations that cannot be seen in two-dimensional displays or by making similar 3-D displays from scanning measurements (Figure 2).

In the Kymi paper mill IQInsight is located in the wet end of the first dryer section. A lot of attention was therefore needed to ensure operation in a harsh environment by sealing, cleaning and pressuring the system. Despite the hostile location, with 70 ºC temperature, relative humidity of almost 100 %, fibre and dust from the paper and steam everywhere, the mill has not reported any problems with the hardware. On the other hand, there was a clear reason for placing the measurement device in this position. Because the beam is located just after the press section, the moisture profile of the paper entering paper machine dryer section can be analysed. Ealier there has not been any measurement at this location, but now the measurement responds very quickly to sheet quality or process changes and makes it possible to distinguish reasons for disturbances (Figure 3).

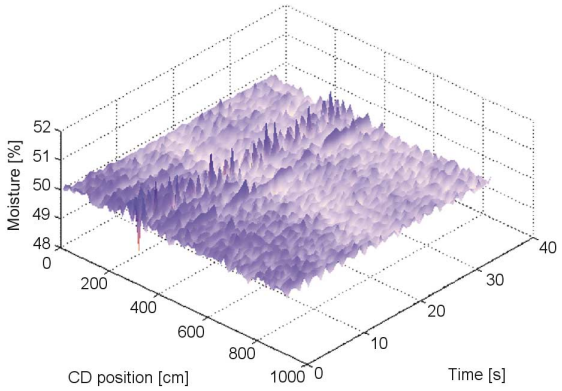

Figure 3. The frequency of cyclic streak detected by IQ-Insight was matched with rotation periods of different components. This pointed to felt that was then seen to be dirty and changed. After replacement the problem disappeared.

The high measurement speed over the whole web – the snapshot analysis – makes it possible to see patterns that will remain hidden to scanners. Although some of these phenomena seem more “nice to know” than of paramount importance, they still prove how transcendent this technique is compared to traditional scanners (Figure 4). This, combined with the operation inside the paper machine where no scanner has been installed before, enables optimisation of the press section and drying section and therefore leads to better runnability and a higher running speed.

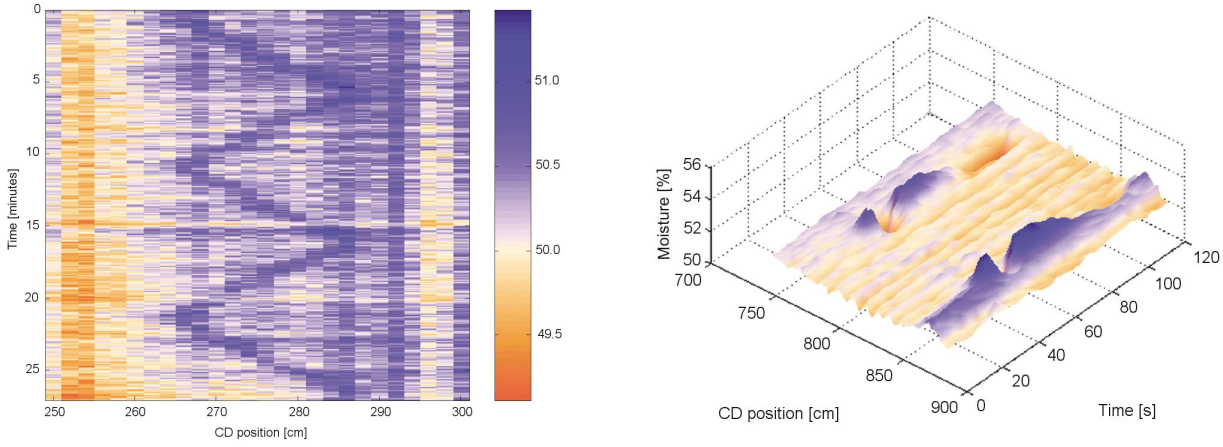

Figure 4. Imprint of fabric cleaning shower on the paper (left) and calibration of two dilution valves where the whole calibration sequence lasts less than 2 minutes (right).

CONCLUSION

The main role of VTT was to take care of the evaluation of the implementation principles of optics, the optical design of the final optical structure, application know-how in spectroscopy, calibrations of moisture measurement and manufacturing high precision optomechanics. IQ-Insight is a sophisticated integrated measurement system for the harsh environment of the press section, and it gives for the first time the possibility to monitor CD and MD moisture variations separately. The benefits to improve the controllability and runnability of the paper process are obvious.

Pekka Suopajärvi
Pekka.Suopajarvi@vtt.fi

Janne Suhonen
Janne.Suhonen@vtt.fi

Jussi Tenhunen
Jussi.Tenhunen@vtt.fi

Markku Mäntylä
Metso Automation

Reijo Peura
Suomen Optomekaniikka

Performance Evaluation of Near Infrared Spectrometers Based on Array Detectors

INTRODUCTION

Array detectors are proving themselves to be increasingly useful in applied spectroscopy. Spectrometers based on array detectors offer many advantages such as the capability to record a full spectrum typically using 128, 256 or 512 pixels, high speed, lack of moving parts, wavelength repeatability and compatibility with fiber optics for flexible process interfacing. Array detectors operating in the near infrared region (NIR, 0.75−2.5 µm) are potential for process measurement applications but there is only limited information available on the performance tradeoffs between the various technology options.

VTT Electronics has studied commercial spectrometer units based on PbS (Lead sulfide), standard InGaAs (Indium Gallium Arsenide) and extended InGaAs array technologies. The work was carried out within the strategic project, "Optical Techniques for Industrial Inspection". Main objectives of the evaluation were to determine linearity, signal to noise ratio, and spectrometer system stability in varying ambient temperature. Commercial spectrometers evaluated were Zeiss MCS 511 NIR [1], TQA Analyser [2,3], J&M Tidas [4] and Hamamatsu PMA-11 series C8147-38 [5]. The main specifications of the studied systems are presented in Table 1.

EXPERIMENTAL

All evaluated spectrometers have an A/D converter with 16 bit resolution. Linearity was determined within this dynamic range by simply measuring different illumination levels for a constant integration time. Different illumination levels were realised by using an adjustable blind together with appropriate beam homogenisation. An Ando optical power meter was used as a reference instrument, with a germanium probe AQ-2711 or AQ-1971. The measurements were made for a complete system composed of spectrometer optics permanently aligned in front of the detector array. As detected light has wavelength distribution, only pixels that experienced close to full A/D converter scale were selected for the linearity study.

Signal to noise tests were performed using stabilised illumination (Gilway, part no. L519-G, 12 V/20 W) and Spectralon 99 % reflectance standard. Signal levels were optimised by adjusting integration time for each spectrometer. Signal to noise ratios were mathematically averaged in the cases of J&M and Hamamatsu spectrometers. This yields to an effective 100 ms integration time value which corresponds to Zeiss spectrometer's direct integration time of 100 ms. Input of the Zeiss spectrometer had to be neutral density filtered (OD = 2, T = 1 %) to avoid detector saturation.

The tests for stability of dark current were arranged for the InGaAs spectrometers only. The spectrometers were placed inside a weather chamber and preprogrammed temperature cycling was run through. All spectrometers were equipped with internal temperature stabilisation or cooling, which was operational during the tests. Operating temperature recommendations notified by the manufacturers were taken into account when temperature cycling was programmed. The spectrometer was operated at a temperature for a two hour period to ensure time for stabilisation, after which a new temperature level was executed. Depending on the spectrometer, the steps were ± 5 ... 10 °C each. Three temperature levels were tested and dark current spectra were recorded during the process.

RESULTS AND DISCUSSION

Figure 1 presents nonlinearity curves as a function of normalised reference power for a typical pixel of each spectrometer. Linearity in Zeiss and TQA spectrometers was very good, typically 0.2 and 0.5 percent, respectively. The extended InGaAs spectrometers were found to have more nonlinear characteristics. Typical results for J&M ranged from 2 to 6 percent, depending on the pixel in question. The non-linearity measured for Hamamatsu was around 3.5 percent peak-to-peak, with a characteristic shape for all pixels. The nonlinearity of the test setup was minimised by design, but is not known. The result measured for Zeiss is likely to be affected by the setup

Table 1. Main specifications.

	Zeiss MCS 511 NIR	J&M Tidas	Hamamatsu PMA-11	TQA Analyser
array technology	InGaAs	ext-InGaAs	ext-InGaAs	PbS
operating range	0.95 - 1.7 µm	1.2 - 2.3 µm	1.6 - 2.35 µm	1.2 - 2.3 µm
array manufacturer	Sensors Unlimited	Hamamatsu	Hamamatsu	Cal Sensors/ Rikola Ltd.
no. of pixels	128	256	256	24
pixel dimensions	50 x 500 µm	50 x 250 µm	50 x 250 µm	1 x 4 mm

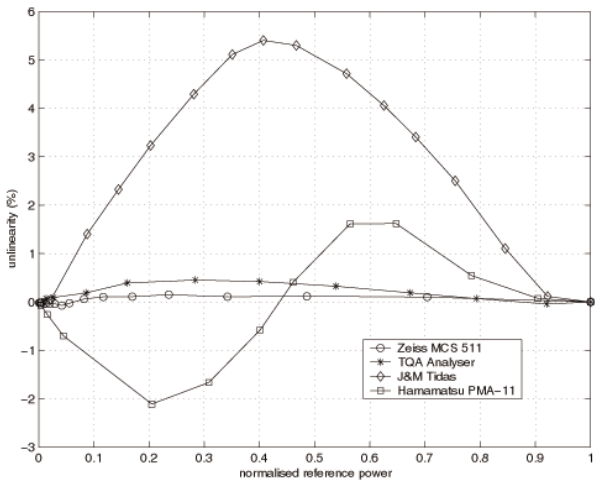

Figure 1. Unlinearity as a function of normalised reference power.

nonlinearity, but the results with higher nonlinearity for the other spectrometers are expected to be reliable.

Figure 2 presents measured noise in digital numbers (DN) based on signal to noise tests for the three spectrometers. The optimum integration times chosen were 100, 3 and 10 ms for Zeiss, J&M and Hamamatsu, respectively. Hamamatsu can be seen to have the lowest noise using these measurement parameters. The same measurement data was used to calculate signal to noise ratios for an equivalent integration time of 100 ms, based on averaging 33 and 10 scans for J&M and Hamamatsu, respectively. Averaging reduced noise according to expectations for J&M, from about 30 DN to 7 DN, whereas the noise of Hamamatsu was only reduced from about 8 DN to 6 DN. This characteristic of Hamamatsu may be due to significant 1/f-type noise content in the measured signals. As shown in Figure 3, all tested InGaAs spectrometers reached a sufficient signal to noise ratio in their operating wavelength scale, when appropriate integration time and sufficient illumination was used. It is worth remembering, however, that the illumination used for J&M and Hamamatsu was 100 times higher than for the Zeiss spectrometer, as discussed earlier.

Figure 4 illustrates dark signal instability of the InGaAs spectrometers based on the measurements in the stability test. The data shown was recorded in the temperature chamber at two temperatures: +25 °C and +15 °C. The results were calculated to dark signal change in digital numbers per 1 °C and repeated for all pixels corresponding to the wavelength scale of the spectrometer. The changes recorded for Zeiss are very small, but the direction of the change was found to be different for even and odd pixels [6]. The tested extended InGaAs spectrometers seem to have significant dark signal drift with temperature, this is especially true for the J&M spectrometer. The dark signal change recorded for Hamamatsu seems to vary across the length of the spectrum, which may be due to spatial differences in cooling and thermal stabilisation across the detector array. The changes recorded for J&M are much higher, but more random from pixel to pixel. The average dark signal drift per 1 °C was calculated for each spectrometer and is summarised in Table 2. As the dark signal drift is given in absolute digital numbers, it is affected by the magnitude of dark current and any further amplifications used within the spectrometer. It is therefore interesting to compare dark sig-

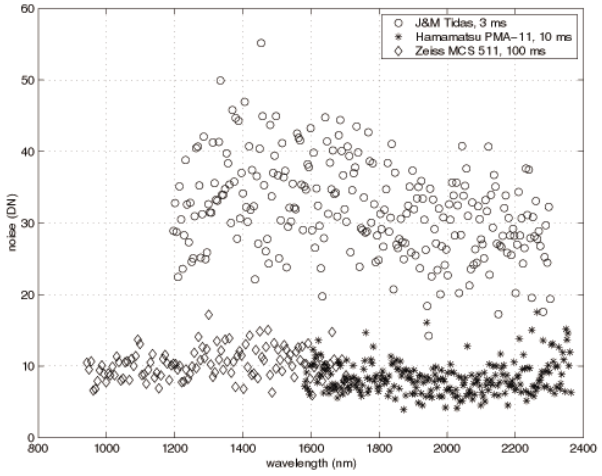

Figure 2. Noise in units of digital number (DN) for spectrometer specific integration time.

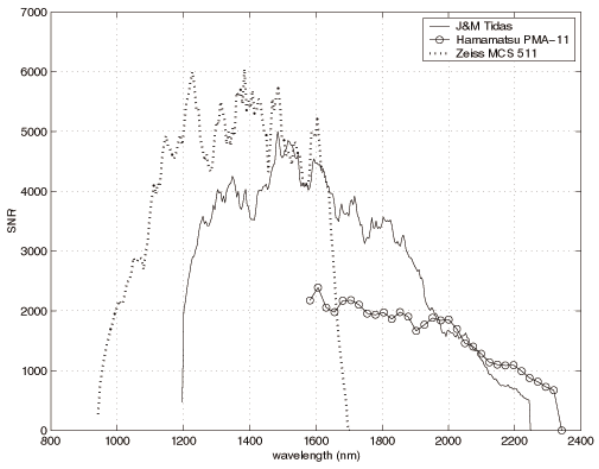

Figure 3. Signal to noise ratios at 100 ms.

nal drift with dark signal noise for each spectrometer. For this purpose dark signal noise was calculated from data recorded during a stable period at +25 °C and included in Table 2. Although the absolute drift of J&M is high, relative to dark signal noise it is only slightly higher than for Hamamatsu.

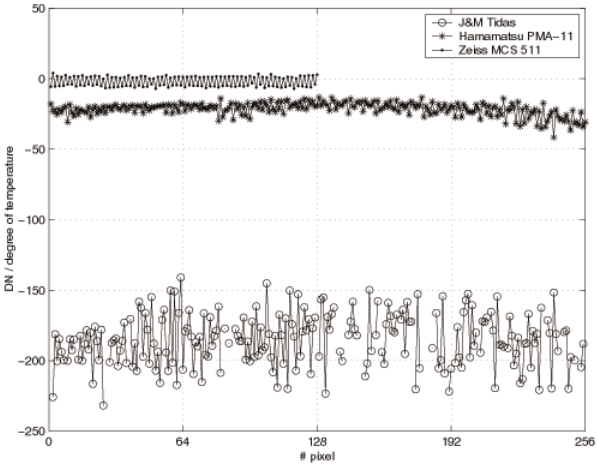

Figure 4. Dark current change calculated per 1 °C across the full spectrum of 128 or 256 pixels.

SUMMARY

Performance testing was arranged for commercial NIR spectrometers based on competing detector array technologies. The tested spectrometers were based on standard InGaAs, extended InGaAs and PbS detector materials. The evaluations made covered linearity of photometric scale, signal to noise ratio and stability of dark current against fluctuations in ambient temperature. The results obtained for a standard InGaAs spectrometer presented very good signal to noise ratio and satisfactory linearity and dark signal stability. The extended InGaAs spectrometers were found to have higher signal nonlinearity ranging from 2 to 6 % and significant dark signal drift due to changes in ambient temperature. Furthermore, extended InGaAs spectrometers require higher level of sample illumination, approximately x100, before they reach ideal signal to noise characteristics. The results of evaluation have produced valuable knowledge and experience, which will be useful in future R&D work for applying these spectrometers in various process monitoring applications.

Table 2. Summary of dark current stability testing.

	Zeiss MCS 511 NIR	J&M Tidas	Hamamatsu PMA-11
integration time	10 ms	3 ms	8 ms
average dark current change (DN/degC)	-5.3 (odd) / 1.5 (even)	-185	-22
rms noise (DN @ 25 degC)	8	29	6

REFERENCES

1. URL: http://www.zeiss.de
2. URL: http://www.abb.com
3. Malinen J., Hagrén E. & Sutinen R.(2000) PbS-Array Based NIR Spectrometer for Analysing Fast Moving Process Streams, Report No. 00-5-1. 4th European Symposium on Near Infrared (NIR) Spectroscopy. Kolding, DK, 10 - 12 May 2000. Biotechnological Institute. Kolding (2000), s. 165 - 169.
4. URL: http://www.j-m.de
5. URL: http://www.hamamatsu.se
6. H. Lindström (2002) Performance evaluation of near infrared spectrometers based on array detectors, diploma thesis.

Hannu Lindström
Hannu.Lindstrom@vtt.fi

Jouko Malinen
Jouko.Malinen@vtt.fi

The Use of Raman Spectroscopy to Assess the Degree of Crystallinity of Lactose

INTRODUCTION

VTT Electronics and the Department of Pharmaceutics at the University of Kuopio have carried out the quantitative analysis of crystallinity using a CCD-Raman spectrometer. This research was part of the 'Laara' project (Raman spectroscopy as an analytical method in drug development and manufacture). Other companies involved are Orion, Leiras, Pharmatory, Specim and the Central Criminal Police. Other fields of interest (in addition to polymorphism) are narcotics, polymer technology, powder and tablet technology.

Polymorphism describes different packing arrangements of the same molecular species. The detection of polymorphs has become essential in the pharmaceutical industry since different modifications can have markedly different biopharmaceutical properties. By investigating the possible polymorphic modifications of a drug, costly repercussions through the untimely appearance of new forms can be avoided.[1,2] A large variation in the properties of some polymorphs may be exhibited, which leads to their exploitation to produce a polymorph more appropriate to the final dosage form. Pharmaceutically desirable properties such as chemical stability may depend heavily on the polymorph selected and the polymorphic form of a drug may change on storage, which necessitates the need for the detection and quantifying of polymorphic mixtures.[3]

Lactose is a polymorphic excipient usually used in pharmaceutical products as α-anhydrous lactose, spray-dried lactose and α -lactose monohydrate. Other polymorphs, such as β -lactose, are used less. The CCD-Raman spectrometer used in this study was developed by VTT Electronics.

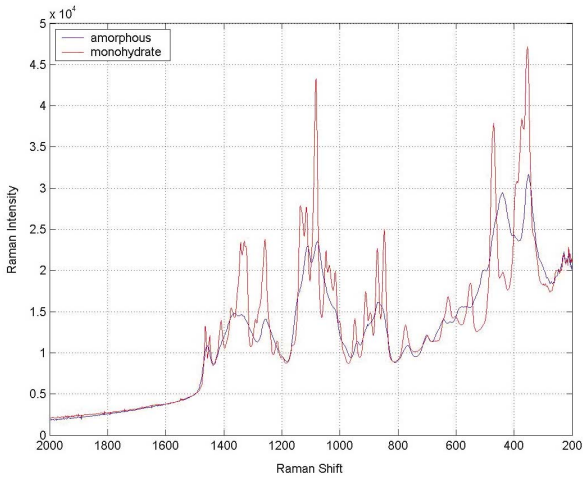

Figure 1: Raman spectrum of amorphous and crystalline lactose.

RESULTS

Amorphous lactose was spray dried from solution. The amorphous nature of the lactose was confirmed with an isothermal microcalorimeter. Known ratios of amorphous and crystalline lactose were prepared by geometrically mixing a total weight of 500 mg in a Wig-L-bug stainless steel mixing capsule without the ball. The capsules were cooled in liquid nitrogen before grinding. Grinding time was 5 minutes. The Raman spectra of crystalline and amorphous lactose are shown in figure 1. It can clearly be seen from figure 1 that the crystalline state typically leads to sharp, narrow peaks whereas material in the amorphous state leads to broader peaks.

CONSTRUCTION OF A CORRELATION CURVE

Crystallinity was determined from the spectral area of 500 to 410 cm^{-1}. In the crystalline state a new peak was growing from the shoulder of the amorphous content. The area of this new peak was employed in calculations. The areas used in quantitative analysis are shown in figure 2. The ratios of these areas were calculated. A correlation curve between (area) ratios and relative amounts of crystalline lactose is shown in figure 3.

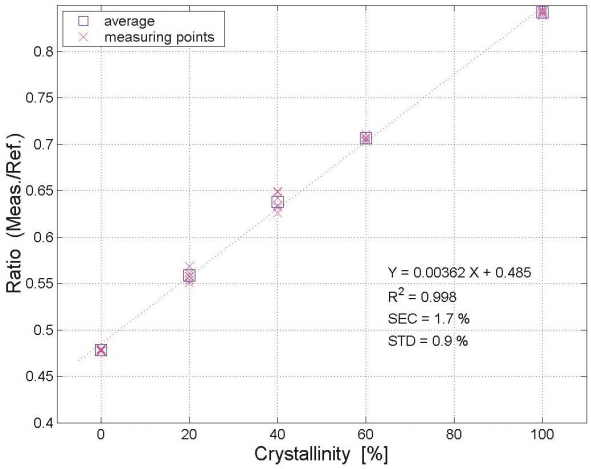

Figure 2: The areas used in quantitative analysis.

During measurement the samples were rotated stepwise. With stepwise rotation it is possible to study the degree of homogeneity in the sample. The measuring time used in this study was 10 times 10 seconds. Each measuring point was run seven times. This was an experimental study and measurements conducted with the isothermal microcalorimeter were of the same kind. Hence, the results achieved with Raman spectroscopy seem to correlate well with the microcalorimeter studies. The largest source of error appears to be in the homogeneity of mixing during the preparation of samples. In consequence,

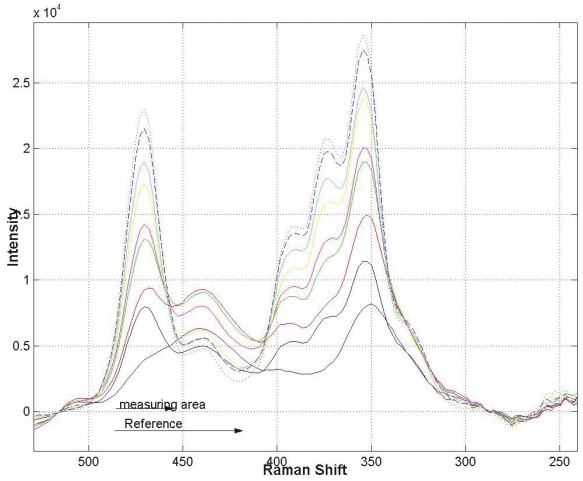

Figure 3: Correlation curve.

the preparation of homogeneously mixed standards for the construction of a calibration curve is necessary for a quantitative method.

CONCLUSIONS

A quantitative, non-destructive CCD-Raman spectroscopic method has been developed for the analysis of mixtures of crystalline and amorphous lactose. A correlation curve was constructed which was linear across the entire composition range.

One further perspective in the use of Raman spectroscopy for the analysis of polymorphism is connected with the possibility of using CCD-Raman in situ. CCD-Raman spectra can be obtained from whole, undisturbed, pharmaceutical tablets and pharmaceutical formulations can be studied directly in case of several crystal forms.

REFERENCES

1. Campbell Roberts, Williams, Grimsey, Booth, *J. Pharm. Biomed. Anal*. 28, 1135-1147, (2002).
2. Bladgen, Davey, *Chem. Brit.* 35, 44-47, (1999).
3. Khoshkhoo, Anwar, *Phys. D Appl. Phys*. 26, B90-93, (1993).

Maarit Päällysaho
Maarit.Paallysaho@vtt.fi

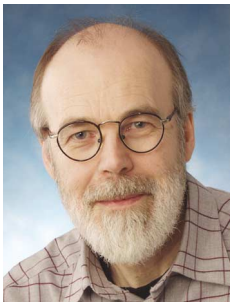

Pentti Niemelä
Pentti.Niemela@vtt.fi

Janne Suhonen
Janne.Suhonen@vtt.fi

Kristiina Järvinen, Erja Katainen
The University of Kuopio, Department of Pharmaceutics

Raman Investigation of Minor Component Reaction During Polymer Synthesis Process

ABSTRACT

Raman spectroscopy was applied to study the reactions between amine and epoxy groups, which had been expected to proceed during synthesis of hybrid polymer based on three monomers: 3-aminopropyltrimethoxysilane (APTES), 3-glycidyloxypropyl-trimethoxysilane (GPTS) and methacryloxy-propyltrimethoxysilane (MPTS). The efficiency of the investigated reaction determines the molecular structure of the organic network and consequently the mechanical and optical properties of the manufactured material. An optical system developed for the real-time Raman monitoring was connected with a typical glass reaction vessel and non-invasive measurements were made. An additional FT-Raman investigation was carried out to confirm the results obtained. The transformation of the primary amine as well as the epoxy ring opening was confirmed and the role of catalysers was discussed.

INTRODUCTION

Hybrid polymers are new materials for photonics with a large application and development potential. In these materials a wide variety of optical and mechanical properties can be obtained from the proper design of their molecular structure. Hybrids are usually prepared using sol-gel technology. The main advantage of this method is the possibility of the synthesis of sophisticated materials in a relatively simple, cost-effective and low-temperature process. Sol-gel enables the precise control of composition as well as of the optical and mechanical properties of the final product. However, to obtain a high quality product, a strict control of its molecular structure must be ensured. The most difficult task is the investigation of reactions between minor components, which requires high sensitivity and selectivity of measurement. In the case of hybrids, the problem is related to the bonds of the organic network, whose total quantity in a particular volume of the hybrid material is much lower than the total amount of Si-O bonds. If the inorganic network is condensing properly and the material becomes solid, the investigation of organic polymerisation is not a trivial problem.

EXPERIMENTAL

Sol-gel process

A gelation of a system of silanes containing amine groups and epoxy rings was presented in this paper as an example of the reaction, which needs high sensitivity measurement. The process was performed in a typical two-neck glass flask equipped with a magnetic stirrer. A system of three monomers - APTES, GPTS and MPTS - was used to synthesise the hybrid material. The primary amine – APTES - was expected to become a secondary one as a result of a reaction between the $-NH_2$ groups and epoxy rings. The subsequent reaction between the N-H bond and another epoxy group should have resulted in it becoming tertiary amine. It was the basic reaction for organic polymerisation. To explain more precisely the nature of the reaction between amine and epoxy groups additional experiments were carried out:

1. Systems of APTES/GPTS with different molar ratios (1:2, 1:4, 1:6) were stirred without any additional components. Raman spectra of these solutions were compared with a spectrum of APTES/MPTS system to find out if the reaction between amine and epoxy group may take place without the presence of water and isopropyl alcohol.
2. One set of silanes (APTES/GPTS) was stirred only with water and the other set was mixed only with isopropyl alcohol.

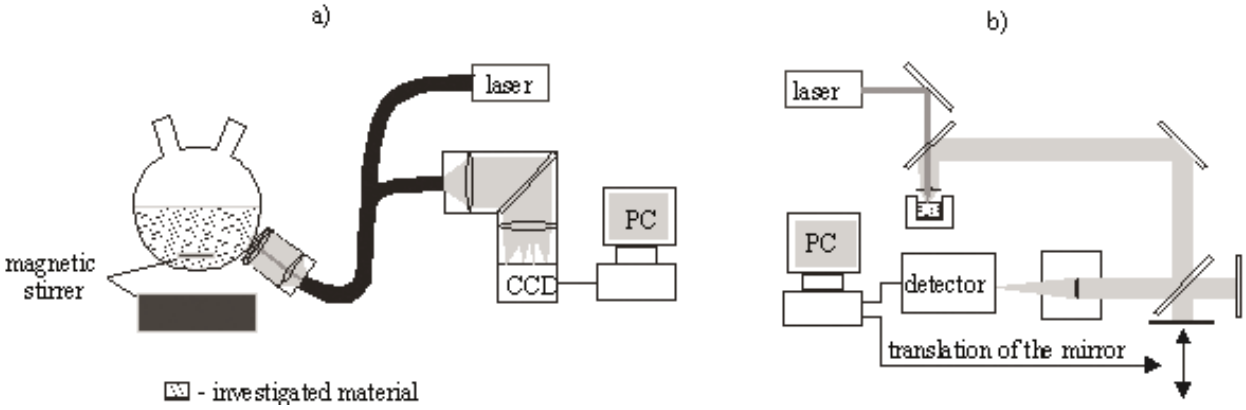

Figure1. Raman devices: a) CCD-Raman system used for real-time monitoring, b) FT-Raman spectrometers.

Measurements

Two Raman bands were used to investigate the behaviour of the amine group and epoxy rings. APTES is a primary amine type PP'[1]. A doublet at 3361-3380 cm^{-1} and 3290-3320 cm^{-1}, assigned to asymmetric and symmetric NH_2 stretching respectively, can be observed in a Raman spectrum of such a structure. After the transformation to secondary amine type SP', only a single peak at 3280-3320 cm^{-1}, assigned to N-H stretching, can be observed, while after the final transformation to tertiary amine type TP' any peak should not be recorded in this range. A peak at 1256 cm^{-1} assigned to epoxy rings breatching was used to study their behaviour [1,2].

To ensure a high reliability of investigation, measurements were carried out in real time and subsequently their results were confirmed by FT-Raman measurements. The measurement systems are presented in Figure 1.

RESULTS

The decrease of intensity in the bands assigned to NH_2 and N-H stretching during the investigated gelation process is presented in Figure 2. The system of three silanes was stirred for 30 minutes. During that time no changes were observed in the Raman spectrum, which is shown in Figure 2a. Then solvents were added (part b) and as a result peaks derived from NH_2 and N-H bonds disappeared in less than 10 minutes. A decrease in the intensity of the Raman doublet at 3310 cm^{-1} and 3370 cm^{-1}, shown in part b) is mainly the result of the change in the total concentration of APTES in the solution after the solvents were added. A disappearance of the doublet after an additional 5 minutes, presented in part c), can be explained only as the transformation of the primary amine to a tertiary one. The weak band observed in part c) originates, as we found out, from the isopropyl alcohol.

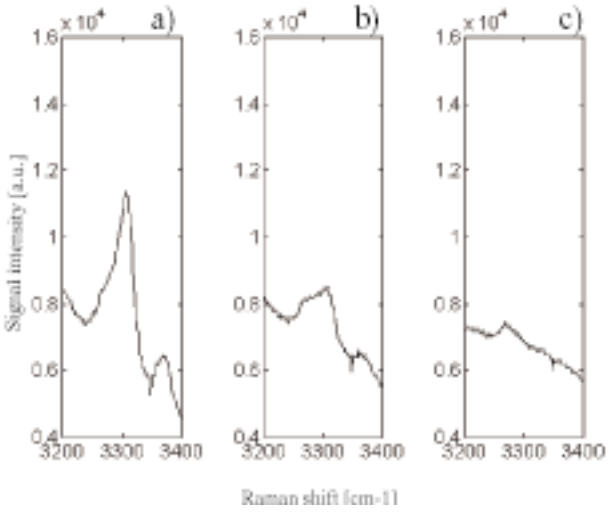

Figure 2. Raman peaks assigned to N-H vibrations: a) APTES/GPTS/MPTS system, b) solution after solvents were added, c) solution after 5 minutes of stirring.

As was mentioned before, systems of APTES and GPTS with different ratios between them as well as APTES/MPTS were mixed for 8 hours and their Raman spectra were monitored in real time. Any changes of intensity in the doublet assigned to NH_2 stretching were not observed during these reactions. Additional experiments – investigation into the influence of solvents on described reactions – showed that the addition of water caused a decrease in Raman peaks assigned to the primary and secondary amine while the addition of isopropyl alcohol did not. Also MPTS was not catalysing the amine-epoxy reaction itself. FT-Raman investigation confirmed these results. The kinetic plot of a Raman line assigned to epoxy ring breatching (1256 cm^{-1}) is presented in Figure 3. To compensate the influence of a change of relative concentration of silanes in the solution after the addition of solvents, the intensity of this line was related to the intensity of a peak at 1631 cm^{-1} assigned to the C=C double bonds of MPTS. Such operations were carried out because the ratio of GPTS/MPTS was constant during the process and subsequently crosslinking between double C=C bonds had not been expected to happen. The short-time fluctuation of intensity is a result of the constant mixing of the solution. However, a general trend can be observed and the efficiency of the reactions can be estimated. It looks as if about 40% of the epoxy rings were opened during the 8 hours of the process.

Preliminary analysis suggested that the addition of solvents simply catalysed the reaction between the amine group of APTES and the epoxy rings of GPTS. However, a comparison of reaction times shows that epoxy ring opening was quite a slow process and a constant, approximately logarithmic, decrease could have been observed during the whole process. On the other hand, Raman peaks derived from primary and secondary amine disappeared after a few minutes. It suggests that the amine-epoxy reaction is not the only one taking part during organic polymerisation.

It may be assumed that progressively, as the epoxy rings were being opened, they were removing temporary substituents and creating the required organic network originated from the amine and epoxy groups.

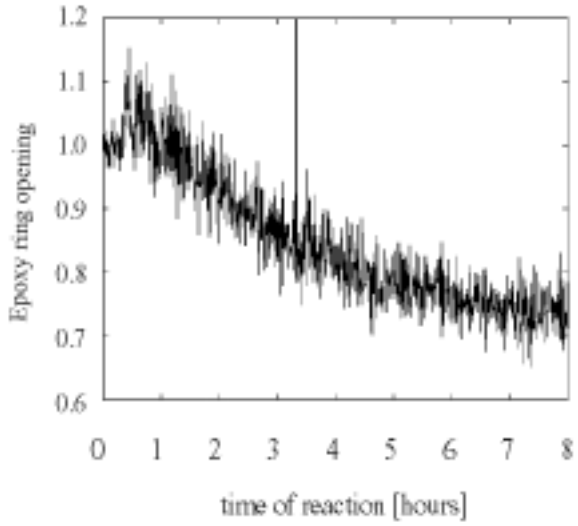

Figure 3. Kinetic plot of a peak assigned to an epoxy ring related to the peak assigned to double C=C bonds.

CONCLUSIONS

The Raman monitor enabled the investigation of the reactions in the organic part of a hybrid material during its synthesis. The process was performed in a typical glass reaction vessel. The measurement was totally non-invasive. No access inside the vessel was required. This means it is also possible to use Raman spectroscopy to control vacuum processes, as well as those which are performed in the presence of an aggressive chemical atmosphere. The measurement of time and the efficiency of primary and secondary amine transformation as well as epoxy ring opening showed that amine-epoxy reaction is a sophisticated process which needs a catalyser. It was proved that during the investigated process water worked as the catalyser. Moreover, it was found that epoxy ring opening is not as rapid a process as amine transformation and some temporary substitution can take place during the reaction. Consequently, to obtain the required optical network, the reaction should proceed until the required amount of epoxy ring (in this case about 50%) was opened. Investigations presented herein should be treated as introductory. In further investigations, the appropriate mixing time required for epoxy ring opening will be precisely measured and the structure of the final organic network will be investigated.

REFERENCES

1. Lin-Vien D., Colthup N.B., Fateley W.G., Grasselli J.G., *The Handbook of Infrared and Raman Characteristic Frequencies of Organic Molecules.* Academic Press Inc., 1991.
2. Riegel B., Blittersdorf S., Kiefer W., Hofacker S., Müller M., Schottner G., "Kinetic investigation of hydrolysis and consideration of the glycidyloxy propyltrimetoxysilane /aminopropyltriethoxy-silane system by means of FT-Raman Spectroscopy." *J. of Non-Crystalline Solids*, 76-84, 226, 1998.

Mikko Keränen
Mikko.Keranen@vtt.fi

Janne Suhonen
Janne.Suhonen@vtt.fi

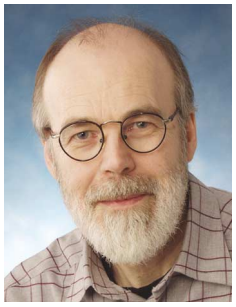

Pentti Niemelä
Pentti.Niemela@vtt.fi

Marcin Gnyba, Robert Bogdanowicz, Małgorzata J drzejewska-Szczerska
Gdan sk University of Technology, Gda sk, Poland

Minitaturization and Integration of Opto-electronic Devices

Minitaturization and integration of opto-electronic devices. Licentiate Thesis, Keränen, Kimmo. University of Oulu, Department of Electrical Engineering, (2002) 79p.

The challenging integration process for multi-technology miniaturized modules is studied in this thesis.

The origin of miniaturization concept is shortly introduced. The terms microtechnology and nanotechnology are shortly introduced. Microtechnology is already in use and utilized in the realization of MOEMS. Nanotechnology, in which structures of components are constructed at the atomic and molecule level, is seen as an ultimate miniaturization technology in the future.

The integration process model utilized in the realization of miniaturized opto-electronic modules and systems is shown and discussed. The most important parts in the integration process are generation and evaluation of concept ideas and analytic simulation of the components, modules and systems. Monte-Carlo simulations are also extremely important, because they can give valuable information about the tolerances and performance variation of the manufactured systems. In some occasions those simulations can give fundamental information already at the feasibility study phase. Monte-Carlo simulations can also save essentially resources in the development process.

The possible realization technologies for miniaturizated opto-electronic components and modules are presented. The developed system integration process model is tested and evaluated by using three various pilot cases: a fiber pigtailed laser transmitter, distance sensor and a miniature IR-spectrometer.

Positive utilization of the developed integration process model with different kind of opto-electronic modules in the development process shows that the utilized process model is a useful operations model in diverse miniature module and system integration cases.

Kimmo Keränen
Kimmo.Keranen@vtt.fi

Determination of Factors Affecting Characteristic Impedance of Printed Circuit Board

Jaakola Tuomo (2002) Determination of factors affecting characteristic impedance of printed circuit board. University of Oulu, Department of Electrical Engineering. Licenciate thesis, 65 p.

The effect of temperature, moisture and different manufacturing parameters on the characteristic impedance and effective dielectric constant of microstrip and stripline transmission lines in multilayer FR-4 PCBs have been studied. Also the applicability of the developed impedance measurement method has been studied.

Characteristic impedance and dielectric constant of the lines were measured using a vector network analyzer and a program simulating the TDR (Time Domain Reflectometry) method. The correctness of the program was evaluated by comparison measurements. The inaccuracy of the measurement method was found to be ± 0.1 Ω.

The change in impedance was measured to be -3 % for microstripline and -3.2 % for stripline when temperature changed from +20°C to 120°C. The change in impedance due to ingress of moisture was found to be between –1.5... -4 % for microstriplines depending on manufacturing parameters and materials used. The striplines had a very small moisture dependence due to the signal line location between moisture impermeable copper ground layers.

The microstriplines were found to have a wider distribution in their impedance values than the striplines. The lamination pressure affected both the impedance and the effective dielectric constant and also the standard deviation of the measured results. Higher pressure resulted in lower impedance value, higher dielectric constant and wider distribution of the impedance values. The moisture sensitivity of microstrip lines was found to be slightly affected by lamination pressure. Sensitivity to moisture increased after application of the resist over the microstrip line.

Key words: printed circuit board, stripline, microstripline, manufacturing parameters, moisture, temperature

Tuomo Jaakola
Tuomo.Jaakola@vtt.fi

A Parallel FDTD Algorithm for the Analysis of Optical Data Storage Systems

Juuso Olkkonen (2002) A Parallel FDTD Algorithm for the Analysis of Optical Data Storage Systems. University of Oulu, Department of Physical Sciences. Master of Science-thesis, 102 p.

The need for information storage is increasing at an explosive rate, fueled by global interconnection networks, miniaturized mobile devices, and multimedia requirements for text, images, video and audio. To meet these needs, new storage methods in magnetic and optical data storage are extensively studied; our attention is confined to optical data storage.

This thesis presents a brief survey of Finite Difference Time Domain (FDTD) method, which is widely used to estimate the viability of new optical data storage methods. When the light interacts with structural elements comparable in size to the wavelength of the incident light, as in optical data storage, it is not permissible to invoke assumptions of scalar diffraction theories. The solution has to be sought via numerical methods based on the Maxwell's equations. The FDTD method approximates continuous time and space derivatives of Maxwell's equations in a spatial grid by finite difference operators. This leads to an algorithm, which provides reliable solutions of field distributions and is applicable for a wide range of problems of computational electrodynamics.

The disadvantages of the FDTD method are its relatively high memory requirements and long computational times. The available memory limits the maximum size of a computational domain that can be simulated, while the long computational times restrict the use of the FDTD method for 'what-if' simulations. These limitations can be significantly reduced by using parallel computing. As a part of this thesis, a three-dimensional parallel FDTD algorithm based on the MPI (Message Passing Interface) library is introduced for Beowulf cluster systems, where many PCs are connected to each other by a network.

The applicability of the developed FDTD algorithm for purposes of optical data storage is proved by investigating the interaction of a Gaussian laser beam and a DVD-RAM disk. The electric field distribution in the vicinity of the data layer is observed to be clearly polarization dependent.

Juuso Olkkonen
Juuso Olkkonen@vtt.fi

Characterization and Use of Bragg Gratings in Optical Communications

Soukkamäki, Jussi. Characterization and use of bragg gratings in optical communications. Pro Gradu, University of Oulu, Department of Physical Sciences. Oulu (2002), 124 p.

In this thesis, characterization and use of Bragg gratings in optical communications was examined. The study was concentrated on the properties of the reflection spectrum which are important in optical communications. Also the suitability of the matrix simulation method to characterize the structural quality from reflected spectrum was studied. For this purpose the matrix method was systematically derived from Maxwell's equations.

In the first part of thesis, the concept of Bragg grating is created and introduction of fundamentals is made. Conventional types of gratings are introduced as well as general grating parameters. Both single- and multichannel structures are taken into account. Also the manufacturing techniques and principles are discussed but only the overview of the most general solutions is presented. Also the applications of Bragg gratings in the fiber systems and solutions in optical communications are examined.

In theory part, the derivation of simulation method for reflection spectrum is made. The coupled-mode theory is first derived starting with Maxwell's equations and solutions of general coupled-mode equations are applied to Bragg gratings to generate a matrix method. The derivation is systematically presented. Also the Rouard's method is introduced.

In experimental part, the results from measurements and Matlab-simulations are compared. This study showed, that by using the transfer matrix method the quality of manufactured grating structure can not be well-controlled by examining only the reflected spectrum of the grating. The similar spectrum can be gained with different combinations of the grating parameters. The transfer matrix algorithm is a good tool for the design of grating structures but for the controlling of the manufactured physical parameters other method is needed.

Jussi Soukkamäki

Performance Evaluation of Near Infrared Spectrometers Based on Array Detectors

Lindström H. (2002) . Department of Electrical Engineering, University of Oulu, Finland, Diploma Thesis, 71 p.

Array detectors are proving themselves more and more useful in applied spectroscopy. Spectrometers based on array detectors offer many advantages like speed, lack of moving parts, continuous measurement of spectrum, wavelength repeatability, process applicability and large number of channels in comparison to traditional scanning spectrometers. Array detectors operating in the near infrared region (NIR) offer considerable performance for process measurement applications e.g. in pulp and paper industry, food and beverage industry and pharmaceutical industry.

The most important part of this diploma thesis was to evaluate the performace of commercial Zeiss spectrometer which is build around MMS NIR spectrometer module. The module has an InGaAs array detector with a standard 1.7 µm cut-off wavelength. Properties of interest were linearity, signal-to-noise ratio and noise, dark current, temperature drift, stray light level and wavelength resolution. Additional measurements were done with commercial spectrometer based on PbS array detector. Performance of spectrometers was compared. The calibration of both spectrometer was carried out with a blackbody light source.

Linearity of both spectrometer was determined to be better than one per cent. The linearity results were probably limited by the measurement set-up itself. Typical signal-to-noise ratio of InGaAs spectrometer was determined to be 3000–4000 while typical values for PbS spectrometer were 2500–3000 using external illumination source. It was also evident that dark current of InGaAs spectrometer drifted as a function of temperature. Moreover, dark current characteristics of odd and even pixels were not similar. Stray light level was determined to be better than one per mille. Resolution results satisfied the Rayleigh criterion.

When spectrometers were compared against each other it became evident that both PbS and InGaAs spectrometers had very similar performance in measuring radiance levels of same order of magnitude. Calibrated noise levels were found to be very similar for both spectrometers. Comparison revealed that in principle it could be possible to replace the array of PbS spectrometer with standard InGaAs array. However, the standard InGaAs detector lacks the longer wavelengths beyond 1.7 µm which are covered by the PbS detector.

Key words: near infrared spectroscopy, NIR, measurement of continuous spectrum, InGaAs detector, PbS detector, performance, linearity, signal-to-noise ratio, dark current, temperature drift, stray light.

Hannu Lindström
Hannu.Linstrom@vtt.fi

LABRA Concept Car
Industrial Design as a Tool for Research

LABRA Concept Car Industrial Design as a Tool for Research. Laudatur thesis, Vehmas Jarno, The University of Lapland, Art and Design, (2001) 48 s + appendices 14

This thesis presents the process of concept design that was used to develop new optical and opto-electronic solutions to be used in the vehicles of the future. The beginning of the thesis focuses on industrial design on a general level, and gives a short review on concept cars. The objective of the presentation of industrial design is to describe the suitability of design to a research environment such as VTT Electronics.

After this, the thesis handles the various stages of the LABRA Concept Car design process. The innovations generated along the process are partly presented using photographs. The material relating to the innovations is intended to be the basis of an article handling the issue, as well as a small-scale exhibition.

A background study into the history of concept cars, as well as short descriptions of five concept cars that have influenced my thesis most have been attached to the end of this thesis. These five concept cars have been chosen especially for the reason that they deviate from the general line of concept cars, and because they were pioneers of their own time.

Key words: Industrial design, concept car, concept design, VTT Electronics, motoring, future

Jarno Vehmas

List of Referred Papers

Ailisto, Heikki; Heikkinen, Veli; Mitikka, Risto; Myllylä, Risto; Kostamovaara, Juha; Mäntyniemi, Antti; Koskinen, Markku. Scannerless imaging pulsed-laser range finding. Journal of Optics A: Pure and Applied Optics. Vol. 4 (2002) No: 6, S337 - S346

Alasaarela, Ikka; Karioja, Pentti; Kopola,Harri. Comparison of distributed fiber optic sensing methods for location and quantity information measurements. Optical Engineering . Vol. 41 (2002) No: 1, 181 - 189

Descour, Michael R.; Kärkkäinen, Ari H.O.; Rogers, Jeremy D.; Liang, Chen; Kilic, Bahattin; Madenci, Erdogan; Rantala, Juha T.; Richards-Kortum, Rebecca R.; Anslyn, Eric V.; and Dupuis, Russell D.; "Towards the development of miniaturized imaging systems for detection of pre-cancer", (Invited paper), IEEE Journal of Quantum Electronics 38, 2, pp. 122-130 (2002).

Gnyba, M.; Keränen, Mikko; Kozanecki, M.; Bogdanowicz, R.; Kosmowski, B.; Wroczynski, P. Raman investigation of sol-derived hybrid polymers for optoelectronics. Opto-Electronics Review. Vol. 10 (2002) No: 2, 137 - 143

Heikkinen, Veli; Aikio, Mauri; Keränen, Kimmo; Wang, Minqiang. Fiberoptic in-vessel viewing system for the international thermonuclear experimental reactor. Review of Scientific Instruments. Vol. 73 (2002) No: 7, 2616 - 2623

Karppinen, Mikko; Kataja, Kari; Mäkinen, Jukka-Tapani; Juuso, Sanna; Rajaniemi, Hannu; Paakkonen, P.; Turunen, J.; Rantala, Juha; Karioja, Pentti. Wireless infrared data links: ray-trace simulations of diffuse channels and demonstration of diffractive element for multibeam transmitters. Optical Engineering. Vol. 41 (2002) No: 4, 899 - 910

Kataja, Kari; Aikio, Janne; Howe, Dennis G.Numerical study of near-field writing on a phase-change optical disk. Applied Optics . Vol. 41 (2002) No: 20, 4181 - 4187

Kololuoma, Terho; Kataja, Kari; Juuso, Sanna; Aikio, Janne; Rantala, Juha. Fabrication and Characterization of Hybrid-Glass Based Axicons. Optical Engineering. Vol. 41 (2002), 3136 - 3140

Kololuoma, Terho; Johansson, L.-S.; Campbell, J.; Tolonen, A.; Halttunen, Marita; Haatainen, T.; Rantala, Juha. The effect of UV irradiation on antimony-doped tin dioxide thin films derived from methacrylic acid modified precursors. Chemistry of Materials . Vol. 14 (2002) No: 10, 4443 - 4447

Kololuoma, Terho; Kärkkäinen, Ari; Rantala, Juha. Novel synthesis route to conductive antimony doped tin dioxide and micro-fabrication method. Thin Solid Films . Vol. 408 (2002) No: 1-2, 128 - 131

Kärkkäinen, Ari; Rantala, Juha; Maaninen, Arto; Ghassan, Jabbour; Descour, Michael. Siloxane-based hybrid glass materials for binary and grayscale mask photoimaging. Advanced Materials. Vol. 14 (2002) No: 7 , 535 - 540

Kärkkäinen, Ari; Rantala, J.T.; Descour, M.R. Fabrication of micro-optical structures by applying negative tone hybrid glass materials and greyscale lithography. Electronics Letters . Vol. 38 (2002) No: 1, 23 - 24

Kärkkäinen, Ari; Tamkin, John M.; Rogers, Jeremy D.; Neal, Daniel R.; Hormi, Osmo;
Jabbour, Ghassan E.; Rantala, Juha; Descour, Michael R. Direct photolithographic deforming of organomodified siloxane films for micro-optics fabrication. Applied Optics . Vol. 41 (2002) No: 19, 3988 - 3998

Marbach, Ralf. On Wiener filtering and the physics behind statistical modeling. Journal of Biomedical Optics . Vol. 7 (2002) No: 1, 130 - 147

Wartak, M S; Weetman, P; Alajoki, T; Aikio, J.; Heikkinen, V; Extraction of rate-equation parameters from optical modal gain measurements for multiple-quantum-well semiconductor lasers. Microwave and Optical Technology Letters, vol. 35 (2002), nro 1, 55-56.

Wartak, M S; Weetman, P; On the design of polarization-insensitive semiconductor optical amplifiers. Microwave and Optical Technology Letters, vol. 35 (2002), nro 3, 227-230.

Weetman, P; Kucharczyk, M; Wartak, M S; Effect of well coupling on the TE optical modal gain in quantum-well-based semiconductor lasers. Journal of Physics: Condensed Matter, vol. 14 (2002), L1-L5.

International Conference Papers

Aikio, Janne; Kataja, Kari J.; Olkkonen, Juuso; Howe,Dennis; Two-dimensional FDTD modeling of direct semiconductor laser read/write systems. SPIE 4647. Functional Integration of Opto-Electro-Mechanical Devices and Systems II. San Jose, CA, 23 - 24 Jan. 2002 . SPIE (2002), 43 - 51

Garmendia, I; Niemelä, Pentti; Tornberg, Jouni; Hietala, Eero Nuevos desarrollos en maquinaria de aplicación de recubrimentos: Sistemas para medición del esposor húmedo en línea y control automático de la aplicación. Proceedings of Eurocoat, Barcelona, ES, 2002. UATCM-Union of Technical Associations of Mediterranean Culture (2002), 811 - 821

Gnyba, Marcin; Keränen, Mikko; Raman scattering measurements in monitoring of polymer synthesis process, SPIE International Conference Lightmetry'02, Warsaw, PL, 2002 (2002), 52

Holmberg, Mika; Lenkkeri, Jaakko; Lahti, Markku; Wiik, Bengt; Reliability of adhesive joints in dual interface smart cards, Proc. of Second International IEEE Conference on Polymers and Adhesives in Microelectronics and Photonics, Zalaegerszeg, HU, 23 - 26 Jun. 2002 (2002), 49 - 53

Karioja, Pentti; Kusevic, Maja; Hiltunen, Marianne; Paaso, Janne; Mäkinen, Jukka-Tapani; Hiltunen, Jussi; Kautio, Kari; Kopola; Harri Sol-gel technologies for multimode waveguide devices. 2002. SPIE, US SPIE: 4640

Kataja, Kari; Aikio, Janne; Howe, Dennis, G; Near field writing on a phase change optical disc, Technical Digest, ISOM/ODS 2002, Hawaii, US, 7 - 11 Jul. 2002. IEEE (2002), 311-313, 439

Kataja, Kari; Olkkonen, Juuso; Aikio, Janne; Howe, Dennis, G. Super resolution near field structure study. Technical Digest, ISOM/ODS 2002, Hawaii, US, 7 - 11 Jul. 2002 (2002), 135 - 137, 439.

Kautio, Kari; Properties of high definition photoimaged conductors in LTCC. Proceedings of the IMAPS Nordic Annual Conference, Stockholm, SE, 2002 (2002), 227 - 232

Kololuoma, Terho; Haatainen, Tomi. Plastic integrated optoelectronics, SPIE 4647. Photonics West. San Jose, US, 23 - 24 Jan. 2002 (2002), 52 59

Kololuoma, Terho; Kataja, Kari; Juuso, Sanna; Aikio, Janne; Rantala, Juha; Morphological and optical characterization of hybrid-glass based axicons, SPIE 4647. Functional Integration of Opto-Electro-Mechanical Devices and Systems II. San Jose, CA, 23 - 24 Jan. 2002 (2002), 60 - 67

Kololuoma, Terho; Tolonen, Ari; Johansson, Leena-Sisko; Campbell, Joseph, M; Kärkkäinen, Ari; Halttunen, Mari; Haatainen, Tomi; Rantala, Juha; Fabrication and characterization of Sb-doped SnO2 thin films derived from methacrylic acid modified tin(IV)alkoxides. 2002. SPIE, US SPIE: 4804

Kusevic, Maja; Hiltunen, Marianne. Development of polymeric materials for waveguide components. 2002. SPIE, US SPIE: 4640

Lahti, Markku; Realisation of narrow conductor lines in LTCC modules by etching technique, Proc. European IMAPS Symposium, Cracow, PL, 16 - 18 Jun.2002 (2002), 271 - 273

Lenkkeri, Jaakko; Jaakola, Tuomo; Kautio, Kari; LTCC substrate technology for MEMS applications, International Workshop on Power MEMS, Tsukuba, JP, 12 - 13 Nov. 2002 (2002)

Malinen, Jouko; Marbach, Ralf; Lindström, Hannu. Detector array based techniques for NIR instrumentation. The 11th International Diffuse Reflectance Conference, IDRC-2002, Chambersburg, US, 10 - 16 Aug. 2002 (2002)

Sillanpää, Teuvo; Pekko, Panu; Oja, Aarne; Heikkinen, Mikko; Kiihamäki, Jyrki; Halme, Jari; Seppä, Heikki; Micromechanical acoustic emission sensor. The 16th European Conference on Solid-State Transducers, Eurosensors XVI, Sept. 15-18, Prague, Czech RepublicEurosensors XVI, Book of Abstracts, Part 1. (Also available as cd-rom 4 p.). Czech Technical University. Praha (2002), 205 - 206.

Vimpari, Antti; The characterisation of the integrated RF passive components in LTCC The IMAPS Nordic Annual Conference, 29 Sep. - 2 Oct. 2002, Stockholm, SE, 2002. IMAPS Nordic (2002), 219 - 226.

Other Publications

Ailisto, Heikki; Haataja, Ville; Kyllönen, Vesa; Lindholm, Mikko Käyttölaite mukautuu moneksi: Tulevaisuuden multikka. Prosessori (2002) No: 9, 72 - 74

Heikkinen, Veli; Heikkinen, Mikko; Mitikka, Risto; Putila, Veli-Pekka Laser rangefinder based on CMOS detector and LTCC technology. Proceedings of Optics Days 2002, Kajaani, FI, 24 - 26 Apr. 2002 (2002), 35

Kondratyev, Vasily; Lahti, Markku; Jaakola, Tuomo; LTCC dual mode patch filter for millimeter-waves Proc. XXVII URSI National Convention on Radio Science, Radiotekniikan päivät, Espoo, FI, 17 - 18 Oct. 2002 (2002), 146 - 147

Känsäkoski, Markku; NIR teoria ja sovellukset, IR-koulutusseminaari. Naantali, FI, 18. - 19.4.2002. Suomen Kemian Seuran Optisen Spektroskopian jaosto (2002).

Kololuoma, Terho; Tolonen, Ari; Johansson, Leena-Sisko; Campbell, Joseph; Kärkkäinen, Ari; Halttunen, Mari; Haatainen, Tomi; Rantala, Juha; UV-photopatternable Sb-doped SnO2 thin films derived from methacrylic acid modified Tin(IV)alkoxides, University of Oulu, Report Series in Chemistry 59. 6th Spring Meeting of the Division of Synthetic Chemistry. Oulu, FI, 28 - 29 May, 2002. Abstract (2002)

Lahti, Markku; The use of etching technique in realisation of fine lines for LTCC modules, Julkaisusarja A - Porin korkeakouluyksikkö A . Porin korkeakouluyksikkö. Pori (2002), 105 - 107
LTCC substrate technology for MEMS sensor packaging. Lenkkeri, Jaakko; Jaakola, Tuomo; Heikkinen, Mikko; Kivimäki, Liisa. Elektroniikan valmistus 2002, Elektroniikan tuotanto- ja pakkaustekniikan konferenssi. Pori 23. - 24.5.2002 (2002), 52 - 57

Åberg, Markku; Jenu, Markku; Kattelus, Hannu; Lenkkeri, Jaakko; Seppä, Heikki; Sipola, Hannu; Varpula, Timo; Vähä-Heikkilä, Tauno. Micromechanical radio frequency systems. VTT Tiedotteita 2146. Communications Technologies. The VTT Roadmaps. Sipilä, Markku (ed.). VTT Information Technology. Espoo (2002), 27 - 43

Examination Theses

Jaakola Tuomo. Determination of factors affecting characteristic impedance of printed circuit board, Licentiate thesis, University of Oulu, Department of Electrical Engineering. Oulu (2002), 65 p.

Keränen, Kimmo. Miniaturization and integration of opto-electronic devices, Licentiate Thesis, University of Oulu, Department of Electrical Engineering, Oulu (2002) 79 p.

Olkkonen, Juuso. A Parallel FDTD Algorithm for the Analysis of Optical Data Storage Systems. Master of Science-thesis, University of Oulu, Department of Physical Sciences, Oulu (2002) 102 p.

Soukkamäki, Jussi. Characterization and use of bragg gratings in optical communications. Pro Gradu, University of Oulu, Department of Physical Sciences. Oulu (2002), 124 p.

Vehmas, Jarno LABRA Concept Car Industrial Design as a Tool for Research. Laudatur thesis, The University of Lapland, Art and Design, (2001) 48 s + appendices 14

Patents

A method and a measuring system for determining and monitoring exhaust gas emissions from a vechicle. Pat. WO 02/82059, application date 3 April 2002, publication date 17 October 2002. Känsäkoski, Markku; Niemelä, Pentti (2002), 42.

Parannettu menetelmä ja järjestely monikanavaisen spektrometrin toteuttamiseksi. Pat. FI 20011399, julkaisupäivä 13.11.2002 (hakemispäivä 29.06.2001), Känsäkoski, Markku; Tenhunen, Jussi (2002)

CONTACT INFORMATION

VTT Electronics
P.O.Box 1100, (Kaitoväylä 1), FIN-90571 OULU, FINLAND
Tel. +358 8 551 2111, fax +358 8 551 2320
e-mail: ele.info@vtt.fi
www.vtt.fi/ele